Probabilistic Design Optimization of Horizontal Axis Wind Turbine Rotors

Marco Caboni

School of Engineering

University of Glasgow

This thesis is submitted for the degree of

Doctor of Philosophy

May 2016

Abstract

Considerable interest in renewable energy has increased in recent years due to the concerns raised over the environmental impact of conventional energy sources and their price volatility. In particular, wind power has enjoyed a dramatic global growth in installed capacity over the past few decades. Nowadays, the advancement of wind turbine industry represents a challenge for several engineering areas, including materials science, computer science, aerodynamics, analytical design and analysis methods, testing and monitoring, and power electronics. In particular, the technological improvement of wind turbines is currently tied to the use of advanced design methodologies, allowing the designers to develop new and more efficient design concepts. Integrating mathematical optimization techniques into the multidisciplinary design of wind turbines constitutes a promising way to enhance the profitability of these devices. In the literature, wind turbine design optimization is typically performed deterministically. Deterministic optimizations do not consider any degree of randomness affecting the inputs of the system under consideration, and result, therefore, in an unique set of outputs. However, given the stochastic nature of the wind and the uncertainties associated, for instance, with wind turbine operating conditions or geometric tolerances, deterministically optimized designs may be inefficient. Therefore, one of the ways to further improve the design of modern wind turbines is to take into account the aforementioned sources of uncertainty in the optimization process, achieving robust configurations with minimal performance sensitivity to factors causing variability.

The research work presented in this thesis deals with the development of a novel integrated multidisciplinary design framework for the robust aeroservoelastic design optimization of multi-megawatt horizontal axis wind turbine (HAWT) rotors, accounting for the stochastic variability related to the input variables. The design system is based on a multidisciplinary analysis module integrating several simulations tools needed to characterize the aeroservoelastic behavior of wind turbines, and determine their economical performance by means of the levelized cost of energy (LCOE). The reported design framework is portable and modular in that any of its analysis modules can be replaced with counterparts of user-selected fidelity. The presented technology is applied to the design of a 5-MW HAWT rotor to be used at sites of wind power density class from 3 to 7, where the mean wind speed at 50 m above the

ground ranges from 6.4 to 11.9 m/s. Assuming the mean wind speed to vary stochastically in such range, the rotor design is optimized by minimizing the mean and standard deviation of the LCOE. Airfoil shapes, spanwise distributions of blade chord and twist, internal structural layup and rotor speed are optimized concurrently, subject to an extensive set of structural and aeroelastic constraints. The effectiveness of the multidisciplinary and robust design framework is demonstrated by showing that the probabilistically designed turbine achieves more favorable probabilistic performance than those of the initial baseline turbine and a turbine designed deterministically.

Keywords: horizontal axis wind turbine design, multidisciplinary design optimization, robust design optimization, wind turbine aeroservoelasticity, uncertainty propagation, environmental uncertainty.

Table of contents

List of tables

List of figures

Acknowledgements

I would like to extend my gratitude to Dr. M. Sergio Campobasso for his valuable support and supervision over the past few years. I would also like to extend my thanks to Dr. Edmondo Minisci for his kind help and encouragement.

This project has been carried out with the support of the wind turbine manufacturer Gaia-Wind and the Energy Technology Partnership, which are hereby acknowledged.

Declaration

Part of the work presented in this thesis has been published in the following articles:

M. Caboni, M. S. Campobasso and E. Minisci. "Wind Turbine Design Optimization Under Environmental Uncertainty". *Journal of Engineering for Gas Turbines and Power*. DOI: 10.1115/1.4032665.

M. S. Campobasso, E. Minisci and **M. Caboni**. "Aerodynamic Design Optimization of Wind Turbine Rotors Under Geometric Uncertainty". *Wind Energy*. DOI: 10.1002/we.1820.

M. Caboni, E. Minisci, and M. S. Campobasso, 2015. "Robust Aerodynamic Design Optimization of Horizontal Axis Wind Turbine Rotors". In *Advances in Evolutionary and Deterministic Methods for Design, Optimization and Control in Engineering and Sciences*, D. Greiner, B. Galván, J. Periaux, N. Gauger, K. Giannakoglou, and G. Winter, eds., Vol. 36 of *Computational Methods in Applied Sciences*. Springer. ISBN 978-3-319-11540-5.

M. Caboni, M. S. Campobasso and E. Minisci. "Wind Turbine Design Optimization Under Environmental Uncertainty". ASME paper GT2015-42674, presented at the *ASME Turbo Expo 2015: Turbine Technical Conference and Exposition*, 15-19 June 2015, Montréal, Canada.

M. S. Campobasso, M. Yan, J. Drofelnik, A. Piskopakis and **M. Caboni**. "Compressible Reynolds-Averaged Navier-Stokes Analysis of Wind Turbine Turbulent Flows Using a Fully Coupled Low-speed Preconditioned Multigrid Solver". ASME paper GT2014-25562, presented at the *ASME Turbo Expo 2014: Turbine Technical Conference and Exposition*, 16-20 June 2014, Düsseldorf, Germany.

I declare that this thesis is the result of my own work and has not been submitted for any other degree at the University of Glasgow or any other institution.

Marco Caboni
May 2016

Nomenclature

Greek Symbols

α	Angle of attack
α_p	Power law profile coefficient
α_w	Weighted sum method weight
δ	Out-of-plane tip deflection
δ_f	Partial safety factors for loads
δ_m	Partial safety factors for materials
δ_n	Partial safety factor for consequence of failure and component classes
δ_T	Total safety factor
κ_i	Joint PDFs of the uncertainty variables
λ	Tip-speed ratio
λ_r	Local speed ratio
μ_{LCOE}	Mean of LCOE
μ_X	Mean of random variable X
ν_i	Joint PDFs of the uncertainty parameters
ν_{12}	Poisson ration
Ω	Angular velocity of the rotor
ω	Rotor speed

ω_1 Blade first natural frequency at a rotor speed of 12.1 rpm

ω_g Generator speed

φ Angle of relative wind

ρ Density

σ_1 Turbulence standard deviation

σ_C Compressive stress

σ_{LCOE} Standard deviation of LCOE

σ_r Local solidity

σ_T Tensile stress

σ_X^2 Variance of random variable X

τ_c Generator torque

θ_p Section pitch angle

$\theta_{p,0}$ Blade pitch angle

θ_T Section twist angle

Other Symbols

a Axial induction factor

a' Circumferential induction factor

a_{skew} Axial induction factor corrected for skewed wake

$\boldsymbol{b}$ Design variables

$\boldsymbol{b_L}$ Design variable lower bound

$\boldsymbol{b_U}$ Design variable upper bound

c Airfoil chord length

C^0 Position continuity

C^1 Tangent continuity

C^2 Curvature continuity

C_D Drag coefficient

C_L Lift coefficient

C_P Local power coefficient

C_Q Local torque coefficient

C_T Local thrust coefficient

c_W Weibull distribution scale parameter

D Rotor diameter

dA Area of annular element

dF_D Local drag force

dF_L Local lift force

dP Local power

dQ Local torque

dr Radial width of annular element

$D_{(RootMxc1)}$ Lifetime damage caused by in-plane moment at the blade root

$D_{(RootMyc1)}$ Lifetime damage caused by out-of-plane moment at the blade root

dT Local thrust

E_{11} Principal Young's modulus

E_{22} Lateral Young's modulus

F Probabilistic objective function

f Objective function

f_{det} Deterministic objective function

F_{hub} Hub loss correction factor

F_{Pr} Prandtl's correction factor

f_{rob}	Robust objective function
F_{tip}	Tip loss correction factor
G_{12}	Shear modulus
G_j	Probabilistic constraints
g_j	Constraints
I	Turbulence intensity
I_{ref}	IEC standard's hub height reference turbulence intensity
K	Torque control parameter
K_{skew}	Function of the skew angle
k_W	Weibull distribution shape parameter
N_b	Number of blades
$\boldsymbol{p}$	Design parameters
P_e	Turbine electrical power
ψ	Azimuth angle
p_X	PDF of a generic variable X
R	Tip radius
r	Mean radius of annular element
Re	Reynolds number
R_{hub}	Hub radius
s	Thickness parameter
U	Freestream wind velocity
u	Wind speed
$\bar{u}$	Mean value of the wind speed distribution
$\bar{u}_L$	Lower bound of the mean value of the wind speed distribution

U_{rel} Relative wind velocity

$\bar{u}_U$ Upper bound of the mean value of the wind speed distribution

V_{e50} Extreme wind speed with a recurrence period of 50 years

V_{hub} Hub height wind speed

V_{ref} IEC standard's hub height reference wind speed

w_b Blade mass

$\boldsymbol{z}$ Generic uncertainties associated with the design variables and parameters

Z Vertical distance from the ground

$\boldsymbol{z}^b$ Uncertainties associated with the design variables

$\boldsymbol{z}^p$ Uncertainties associated with the design parameters

Acronyms / Abbreviations

$1D$ One-dimensional

$2D$ Two-dimensional

$3D$ Three-dimensional

AEP Annual energy production

AoA Angle of attack

AR Blade aspect ratio

BEM Blade element momentum

BOS Balance of station

CFD Computational fluid dynamics

CLT Classical lamination theory

DE Differential evolution

DLC Design load case

EDA Estimation of distribution algorithm

EWM Extreme wind speed model

FEM Finite element method

FIO Fully integrated optimization

FRC Fixed charge rate

GA Genetic algorithm

$HAWT$ Horizontal axis wind turbine

HSS High-speed shaft

ICC Initial capital cost

$IDEA$ Inflationary differential evolution algorithm

IEC International Electrotechnical Commission

LC Lease cost

$LCOE$ Levelized cost of energy

LEP Leading edge panel

LRC Levelized replacement/overhaul cost

MBH Monotonic basin hopping

MDO Multidisciplinary design optimization

$MOPED$ Multi-objective parzen-based estimation of distribution

NS Navier-Stokes

$NSGA-II$ Non-dominated sorting genetic algorithm II

NTM Normal turbulence model

$O\&M$ Operations and maintenance

PDF Probability density function

PPI Producer price index

QoI Quantity of interest

RDO Robust design optimization

RMSE Root-mean-square error

TCC Turbine capital cost

TEP Trailing edge panel

URQ Univariate reduced quadrature

Chapter 1

Introduction

By the late 20th century, wind power had become one of the most promising alternative sources of energy worldwide, achieving a rapid global growth in installed capacity. In the foreseeable future, as shown in Fig. 1.1, the global wind power installed capacity is expected to continue to grow at an average annual rate of about 8%, bringing the worldwide installed capacity up to 600 GW by 2018 [1]. One of the main challenges associated with the

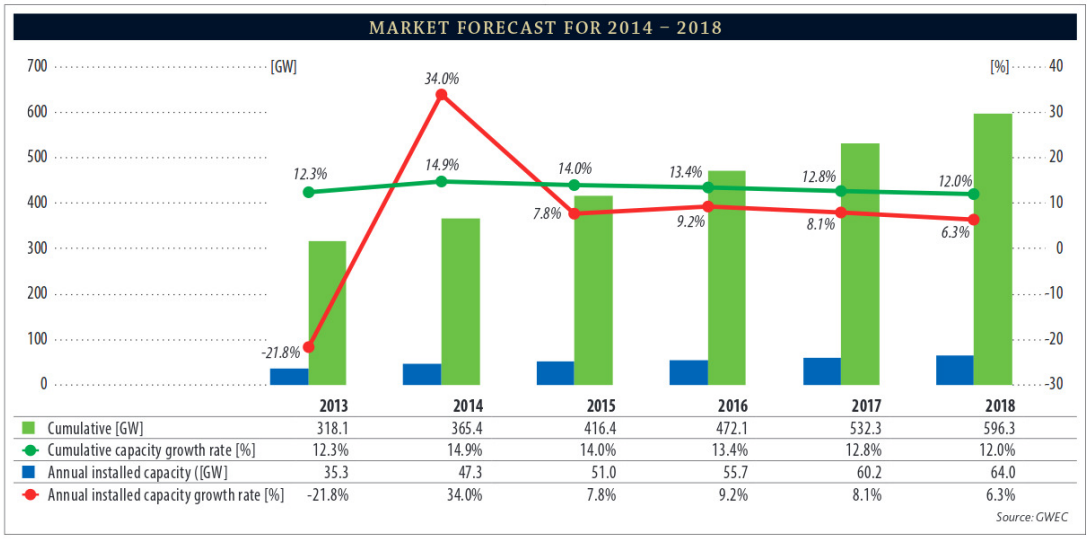

Fig. 1.1 Forecast of worldwide wind power installed capacity. Image reproduced from [1].

advancement of wind energy technology is making wind energy economically competitive with the conventional sources of energy, such as oil, gas and coal. This is normally pursued by lowering the levelized cost of energy (LCOE). This figure of merit can be roughly defined as the ratio of the capital and the operations and maintenance (O&M) costs of an energy

system to the energy capture of the energy system over its lifetime. Accordingly, the LCOE is the minimum price at which energy must be sold for an energy project to break even. The attribute "levelized" in the definition of the cost of energy refers to the fact that the LCOE characterizes the cost of energy of a system by means of a single figure of merit, indeed distributed (or levelized) over the life of the energy system. As depicted in Fig. 1.2, in order to decrease the LCOE a general trend in wind turbine industry has been to increase the rotor diameter, therefore increasing the installation height (or hub height) and turbine rated power. Indeed, larger turbines can extract more energy form the wind, and although both capital and

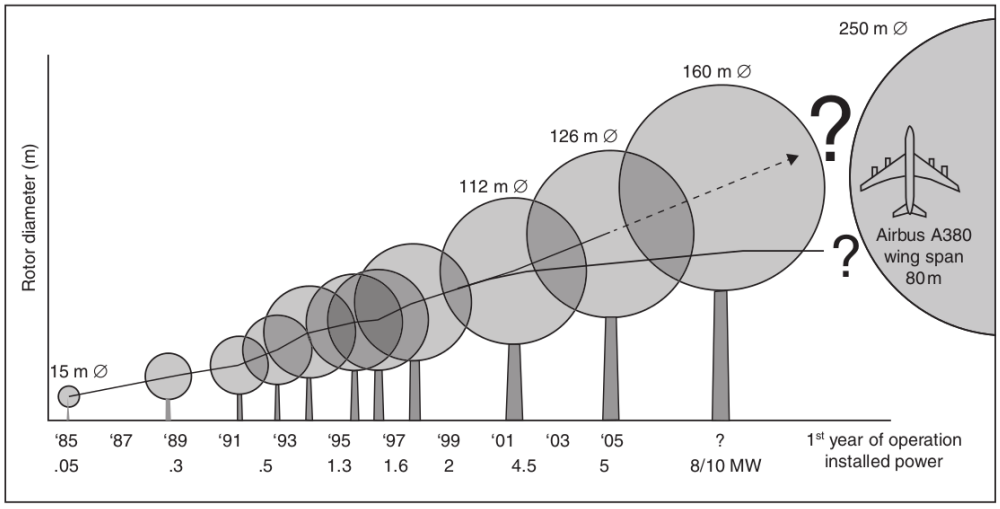

Fig. 1.2 Upscaling history of wind turbine size. The picture shows the trend over the past three decades in rotor diameter, installation height and turbine rated power. Image reproduced from [2].

O&M costs increase, the overall LCOE decreases. During the past few years, offshore wind turbines with rated power up to 8 MW have been developed and installed.

The further increase of wind turbine size represents one of the directions for the future development of wind energy technology [3]. This however will inevitably lead to new challenges, and new solutions are therefore required to tackle them. In fact, as demonstrated by Ashuri [3], the upscaling of large offshore wind turbines, using the current dominant concept (i.e., a three-blade, upwind, variable speed, pitch regulated wind turbine installed on a monopile), presents significative technical and economical challenges for machines approaching 10 MW. Indeed, for very large turbines, the extreme and fatigue loads, that the structural components experience throughout their lifespan, become more severe. This leads to a considerable weight growth associated with the blades and other components [4], posing major challenges to the technical feasibility and economical profitability of wind

turbines. In other words, we cannot keep designing profitable large wind turbines just by upscaling the current concepts without introducing significant advancements in their design. Therefore, in recent years there has been intensive research into the design of more effective wind turbines, focusing on aspects beyond the mere upscaling of current wind turbines. To this aim, advanced analysis and design methodologies have been devised, providing better understanding of the operating behavior of wind turbines, and enabling designers to develop new design strategies. In this research framework, the present thesis focuses on multidisciplinary design optimization (MDO), which will be introduced and reviewed in Sect. 1.1.

1.1 Multidisciplinary design optimization

To study the effect of changing the turbine size on the turbine's components and characteristics, two methods have been traditionally used. These methods, denoted by classical upscaling methods, are indeed based on two approaches, namely on linear scaling laws [3, 5] and existing data trends [3, 5]. The first approach is based on the assumption that all geometrical parameters of the turbine scale linearly with the rotor diameter. This method, however, fails to characterize accurately the technical characteristics and economical performances for large scales. Therefore, it is commonly used only in conceptual design phases. In the second approach, the correlations between the rotor diameter and other parameters are determined by interpolating over real data, available for existing wind turbines. However, when designing turbines larger than the existing ones, and therefore real data are not available, an extrapolation is needed, therefore introducing important uncertainties. Considering these facts, classical upscaling methods are not well suited for the design of large scale wind turbines, and therefore they cannot be used to achieve the aforementioned advancements needed to make large wind turbines effective and profitable. Therefore, the design of large scale wind turbines necessitates the use of alternative methods. These methods should be able to evaluate the relevant design constraints, investigating the results of design modifications in terms of cost of energy.

In general, the situation in which a designer need to improve the performance of a given system is referred to as design problem. In order to solve design problems, several approaches can be followed. Factors like the quality of the solution, time requirements and acceptance of the solution represent different criteria to assess the design approaches. However, good design approaches need to have in common the following characteristics:

- A design approach should incorporate a mechanism for directing the search performed by the designer (or a design solver). The search mechanism should reduce quickly the design space, eliminating non feasible solutions, and leading to the solution.
- A design approach should lead to high quality solutions in a short time. This characteristic is particularly important when dealing with problem involving a large number of design variables and different disciplines.
- A design approach should incorporate an adequate amount of practical knowledge in order to obtain sound solutions.
- A design approach should overcome the designers' psychological inertia, preventing them to came up with innovative solutions.

The design of wind turbines is a multidisciplinary process, integrating aerodynamic, structural, environmental, manufacturing, transportability and cost considerations. The traditional approach to wind turbine design is based on a manual process, relying on the knowledge of the designer, plus intuition and trial-and-error. Such approaches are more efficient for relatively simple design problems. For more complex design problems, involving a high number of design variables, trial-and-error methods present significant drawbacks. For example, a trial-and-error approach is not time effective, as the number of successful trials (that concretely lead to design improvements) per unit of time is low. Other major disadvantages of such methods are that they are not able to define a search direction in which the optimum solution might be found, and also they do not incorporate any mechanism to systematically explore the design space. The use of MDO [6] constitutes a promising way to overcome the inherent limitations of traditional design approaches and improve the design of wind turbines, therefore enhancing their profitability. MDO is a field of engineering that uses mathematical optimization techniques to solve design problems involving a certain number of disciplines. MDO techniques are able to directly and systematically search through the design space for the optimum design, automatically fulfilling specified constraints. This potentially allows designers to come up with configurations beyond their experience and intuition, enabling them to develop new design concepts.

1.1.1 Wind turbine MDO literature review

The aim of wind turbine MDO is to find the best design of a wind turbine by optimizing a set of parameters, denoted by design variables, without violating some constraints. Design variables and constraints represent physical characteristics of wind energy systems, and may be directly related with different disciplines, such as aerodynamics, solid mechanics and control theory.

A review of the design constraints used in wind turbine MDO will be presented in Sect. 1.3. Design variables commonly considered in wind turbine MDO applications include: twist and chord distributions along the blade span [7–20], blade pitch angle [7, 20–22], rotor speed [7, 8, 10, 16, 17, 19–25], rotor diameter [7, 16, 17, 21–25], rated power [17, 21–23, 25], hub height [16, 21–23, 25], blade thickness to chord ratio [7, 10, 11] and the thickness of the blade internal structural layup [7, 10, 14, 16, 17, 19, 25–27]. Lately, a few wind turbine MDO studies have also focused on the optimization of the airfoil shapes [12, 15, 18, 19]. This particular application will be discussed in Sect. 1.4. The design optimization of wind turbines is generally carried out through an iterative procedure, whereby a figure of merit, denoted by objective function, is optimized by varying the design variables. Wind turbine MDO problems have been formulated in terms of different objective functions, including: rotor power [9, 12, 24], wind turbine annual energy production (AEP) [8, 17, 20], blade mass [26], the ratio of turbine mass to AEP [14, 17, 19] and LCOE [7, 8, 10, 11, 14–18, 21–23, 25]. Ning et al. [17] investigated the influence of the objective function choice on the design optimization of a multi-megawatt horizontal axis wind turbine (HAWT). Considering the LCOE minimization as the reference metric in wind turbine design optimization, these authors concluded that maximizing AEP leads to suboptimal solutions, while minimizing the ratio of turbine mass to AEP can be effective only for fixed rotor diameter designs. The iterative design process, by which a high number of wind turbine configurations are generated, is regulated by an optimization algorithm. Optimization algorithms encompass derivative-based algorithms, as well as genetic and pattern search algorithms. A review of these methods is included in Sect. 3.5. Both gradient-based algorithms [7, 10, 11, 14, 16–18, 21, 22, 24] and evolutionary algorithms [8, 9, 12, 13, 15, 19, 20, 23, 25, 26] have been used in wind turbine MDO. At each iteration, the objective function and constraints of the optimized configurations are typically evaluated by means of a computational module, which must be able to rapidly and accurately perform the analysis of a given wind turbine. A complete wind turbine analysis involves determining the interactions between aerodynamics, structure and control. The interaction between these disciplines is commonly denoted by the term “aeroservoelasticity”. In the literature, several MDO methods (or architectures) have been developed and presented [6]. Commonly, wind turbine MDO is performed by using a simple sequential approach, in which the different disciplines are treated in cascade, following successive optimization stages. For example, a simple sequential approach for the MDO of wind turbines is to firstly optimize the aerodynamic shape of the rotor blades taking into account no or only a limited number of structural considerations. Subsequently, once the geometric shape of the blades is determined, and hence the aerodynamic loads on the rotor are known, a structural optimization is performed to determine the internal structural layup of the

blades. Clearly, this approach neglects the coupling between disciplines (i.e., aerodynamics and structure), leading to suboptimal solutions. A more complex and effective MDO method is represented by the fully integrated optimization (FIO) architecture [6]. In this approach, an optimizer is directly coupled with a multidisciplinary analysis model, allowing the different disciplines to interact with each other concurrently during the optimization process.

In recent years, several studies have been devoted to the MDO of wind turbines, encompassing a wide variety of approaches and techniques. Fuglsang and Madsen [7] presented a MDO method for the aeroelastic design of HAWT rotors. Using a gradient-based approach, these authors optimized the design of a 1.5-MW stall-regulated rotor, minimizing LCOE, while enforcing multiple constraints on the ultimate[1] and fatigue loads and the aerodynamic noise emission. Design variables included the blade geometric shape, rotor regulation and the aerodynamic characteristics of the airfoils (i.e., lift and drag coefficients as a function of the incidence). LCOE was reduced by 3.5% and 7% respectively without and with optimization of the aerodynamic characteristics of the airfoils. This paper showed the potential of the integration of airfoil optimization within the rotor optimization. Fuglsang et al. [21, 22] investigated the site-specific design optimization of wind turbines, coupling a gradient-based optimization algorithm with an aeroelastic turbine model. These authors optimized the design of a stall-regulated wind turbine for the minimum LCOE across different installation site conditions, incorporating detailed wind climate information. Design variables included the hub height, rated power and rotor speed and diameter. The optimizations perfomed by these authors showed that there are significant differences in the optimum design obtained for normal flat terrain and offshore, and that cost of energy for offshore wind turbines can be significantly reduced compared with today's wind turbines. Benini and Toffolo [8] used a global multi-objective evolution-based search method to optimize HAWT conceptual designs, investigating the choice of fundamental HAWT design parameters, such as its rotor diameter, on the economy of whole wind farms. The core results showed that the minimization of LCOE requires larger HAWTs having high AEP, but low blade loads and weights. As opposite, the maximization of AEP density requires smaller HAWTs having low AEP but high blade loads which result in expensive designs. The obtained Pareto front, however, allows us to determine the limits of improvement for the AEP density and the corresponding increase in LCOE. Kenway and Martins [10] used a gradient-based optimizer to design a 5 kW wind turbine rotor. These authors considered seven groups of design variables, including: blade chord and twist distributions, spar thickness, spar location, spar length, airfoil thickness, and rotation speed. Subject to a set of structural constraints, the objective was to minimize LCOE by keeping constant wind turbine total costs and maximizing AEP. The framework presented

[1] Ultimate limit state generally corresponds to maximum load carrying capacity [28].

by these authors showed the ability to simulate the average power expected from specific localized wind distributions, allowing one for detailed site-specific optimization. Xudong et. al. [11] developed a design tool based on an aeroelastic model coupled with a gradient-based algorithm which was used to minimize LCOE of three wind turbine rotors of different sizes. The design variables included the blade chord and twist distributions and the blade thickness to chord ratio, while the constraints encompassed the rotor torque and thrust. This work demonstrate that optimization tools in all cases represent a valuable tool for the design of wind turbines to achieve the most efficient design. Maki et. al. [25] optimized the the rotor diameter, the rotational speed, the maximum rated power, the hub height, the structural characteristics of the blade, and the geometric characteristics of the blade (distribution of thickness, twist angle, and chord) of a HAWT by using a multi-level system optimization algorithm. This approach allowed these authors to coordinate and execute a network of two single-disciplinary optimizations, namely the maximization of AEP, and the minimization of the turbine blade moment at the root of the blade. Each single-disciplinary optimization was performed by means of a genetic algorithm (GA), and LCOE was considered as the top-level objective function. Bottasso et al. [14] described a procedure for the MDO of wind turbines, where the blade twist and chord distributions and internal structure are optimized by maximizing AEP and minimizing the rotor blade weight, subject to a set of structural constraints. These authors devised a nested optimization approach solved by two consecutive optimizations. The first optimization maximizes AEP assuming frozen structural parameters, while the second one minimizes the blade weight by using the optimal aerodynamic ones obtained through the first optimization. This procedure was demonstrated on the aeroelastic optimization of two multi-megawatt HAWTs. Using a GA, Vesel and McNamara [15] optimized a multi-megawatt turbine for minimum LCOE, integrating the rotor aerodynamics and the structural bend-twist coupling behavior of the blades. Design variables included airfoil shapes, chord and twist distributions, and the degree of the blade bend-twist coupling. LCOE of the optimized turbine was decreased by over 6% than that of a baseline turbine. Ashuri et al. [16] defined the minimum number of structural constraints that should be considered to obtain a practical design. Using a gradient-based algorithm, these authors optimized the rotor and tower of a wind turbine for minimum LCOE. Blade design variables encompassed chord and twist distribution, blade length, rated rotor speed and structural thicknesses along the span. The use of this methodology contributed to 2.3% reduction in the LCOE compared to a baseline turbine. The results showed a significant improvement in the quality of the design process by means of a realistic assessment of the LCOE and constraints, while keeping the coupling of the disciplines, and by using numerical optimization. Bottasso et al. [18] optimized concurrently the airfoil shapes and the chord and twist spanwise distributions

of a 2-MW wind turbine blade subject to a set of structural constraints. A gradient-based algorithm was used to solve the optimization problem, achieving a 6% reduction in LCOE with respect to an initial reference turbine. This work highlights the improved optimization capability allowed by the simultaneous design of the blade and of its airfoils, thereby achieving a true 3D optimization, in which aerodynamic and structure can interact simultaneously in the course of the optimization.

1.2 Robust design optimization

In the literature, wind turbine design optimization is typically performed deterministically. Deterministic optimizations do not consider any degree of randomness affecting the inputs of the system under consideration, and result, therefore, in an unique set of outputs. However, given the stochastic nature of the wind and the uncertainties associated, for instance, with wind turbine operating conditions or geometric tolerances, deterministically optimized designs may be inefficient. In other words, the performance of deterministically designed wind turbines is likely to deteriorate when they operate in the presence of uncertainty, that leads them to work under off-design conditions. Therefore, one of the ways to further improve the design of modern wind turbines is to take into account the aforementioned sources of uncertainty in the optimization process, achieving robust configurations with minimal performance sensitivity to factors causing variability. Design optimization in the presence of uncertainty is denoted by robust design optimization (RDO) [29]. The main feature of RDO is that the objective function and constraints are treated probabilistically. Three basic steps are required to perform the RDO of a given system. First of all, the uncertainties affecting the physical inputs of the system need to be characterized probabilistically. This is normally accomplished by defining each uncertain variable by means of a probability density function (PDF). The second step consists of propagating the input uncertainties throughout the computational analysis system in order to characterize probabilistically the system outputs (i.e., objective function and constraints) by means of a PDF. The probabilistic definition of the objective function and constraints is often expressed by their mean and the variance[2]. Uncertainty propagation is a computationally intensive step, involving a high number of system analyses. A variety of numerical methods have been developed to carry out uncertainty propagation, from sampling based approaches (e.g. Monte Carlo) to more sophisticated stochastic spectral Galerkin approaches [31]. The third and last step consists

[2]Variance is a measurement of the spread between numbers in a data set. The variance measures how far each number in the set is from the mean. Variance is calculated by taking the differences between each number in the set and the mean, squaring the differences (to make them positive) and dividing the sum of the squares by the number of values in the set [30]. The square root of the variance is called the standard deviation.

of optimizing the probabilistic objective function subject to the probabilistic constraints. When the PDFs of the objective function and constraints are expressed as their mean and variance, the optimization is achieved by concurrently optimizing the mean of the objective function and minimizing its variance, satisfying all constraints within a certain range of variability. Despite the significant impact it may have on wind turbine performance, the RDO of wind turbines has so far received little attention. Petrone et al. [12] optimized the airfoil shapes and blade chord and twist distributions of a stall-regulated rotor for maximum mean power coefficient and minimum acoustic emissions, considering the uncertainty on laminar-to-turbulent transition caused by insect contamination. Uncertainty was propagated by means of the stochastic simplex collocation method, and the optimization was carried out using a multi-objective GA. The design obtained with this probabilistic procedure appeared to be less sensitive to the presence of uncertainty than its deterministic counterpart. Campobasso et al. [20] developed a robust optimization strategy for the aerodynamic design of HAWT rotors accounting for the uncertainty of the blade geometry caused by manufacturing and assembly errors. Their numerical studies aimed at maximizing the expectation of AEP and minimizing its standard deviation by optimizing the chord and twist distributions, and the rotor angular speed. Uncertainty was propagated with Monte Carlo sampling and the univariate reduced quadrature (URQ) approach [32], and a two-stage multi-objective evolution-based optimization strategy was used. The comparative analysis of a rotor design obtained by considering the stochastic geometry errors and a rotor design obtained by neglecting all uncertainties showed that AEP standard deviation of the former rotor was less than 40% than that of the latter. The analyses indicated that a lower sensitivity of AEP to rotor geometry errors can be achieved by lowering rotational speeds and compensating for the reduction of power due to lower rotational velocities by shifting upwards the radial profiles of CL . This increment of the aerodynamic loading is achieved by increasing the angle of attack (to a large extent through lower values of the sectional pitch) and the chord of the blade over most part of the blade length. Caboni et al. [19] generalized the probabilistic design approach of [20] by including also the airfoil geometry in the probabilistic design environment, and applied this technology to maximize the expectation and minimize the standard deviation of AEP of a multi-megawatt rotor subject to geometric uncertainty. Both robust optimization processes performed in this paper confirm that the search for the lower sensitivity to geometry errors is pursued by adopting lower rotational speeds, and therefore the robustness is actually obtained by moving to a range of higher values of the angle of attack where the slope of the angle of attack/lift coefficient curve is lower than for lower values of the angle of attack. Using a gradient-based optimizer, Ning et al. [17] designed a wind turbine rotor to be used across diverse sites characterized by a different mean of the

wind distribution. Subject to a set of structural constraints, blade chord, twist and spar cap thickness distributions, rotor speed, diameter and rated power were optimized to minimize the expected value of LCOE. The robust design achieved a 1.2% lower average LCOE than that of a deterministically designed rotor. This paper showed the importance of combining optimization with uncertainty quantification, along with a better understanding of the nature of the uncertainties.

1.3 Structural constraints

To ensure structural integrity, wind turbines must satisfy an extensive set of structural requirements, relating to material ultimate and fatigue strength, deflections and structural stability. Several national and international organizations, such as the International Electrotechnical Commission (IEC), Germanischer Lloyd and Det Norske Veritas, prepare and publish standards covering the various aspects of the wind turbine design process. More specifically, these standards prescribe a large number of combinations of environmental and operating conditions under which wind turbine components need to be verified structurally. These design combinations are normally referred to as design cases. In addition, the standards define the procedures to be followed when calculating ultimate and fatigue loads, suggesting the application of safety factors to cover uncertainties and variabilities of various natures (such as in loads and materials) in the design procedure. Specifically, the structural analysis of wind turbine components starts from predicting the loads that the wind turbine components experience during their lifespan, considering a combination of different operating conditions (e.g., normal, fault, and parked) and environment conditions (e.g., normal and extreme wind). For each design case considered, load predictions are carried out by means of aeroelastic codes, which are able to simulate the complex dynamic interaction between wind turbine aerodynamics and structure under various conditions. Subsequently, these loads are augmented by means of safety factors in order to consider, for instance, possible errors in the aeroelastic model, or the uncertainty related with the strength of constituent materials. A stress-strain analysis is then required to verify the structural integrity of each component subject to the calculated loads. Generally, this analysis step involves the calculation of ultimate stress, fatigue damage, component deflection and structural stability, such as buckling. Structural integrity is ensured when these criteria fulfill the structural strength requirements of materials and components.

In the context of wind turbine optimization, all configurations generated during the iterative design procedure should be assessed structurally, to make sure that they satisfy the design requirements prescribed by the standards. In practice, during the optimization,

the above-mentioned structural criteria, treated as design constraints, must be kept below their critical values, for the full set of design cases. Due to the large number of aeroelastic simulations required, this is a computationally expensive step, and in most cases impracticable. Fortunately, a limited number of design cases have been proven to be the most likely design driver for majority of turbine blades [16, 33, 34]. In particular, the design case in which the wind turbine rotor is parked and subject to extreme wind conditions is one of the most critical cases for ultimate stress, deflection and buckling. In the literature, only few HAWT design optimization studies attempted to consider a sufficient number of design cases to obtain a practical design [14, 16, 17], evaluating the turbine response with respect to ultimate strength, fatigue failure, stability and critical deflections. In fact, wind turbine design optimization is commonly subject only to a limited number of structural constraints, neglecting the most relevant design cases. Typically, the structural verification in wind turbine design optimization problems is carried out by using simple surrogates of more involved structural analyses. However, this approach may neglect design cases or criteria that may predict structural failure. In the majority of MDO studies reported in the literature [7–20], only operational conditions are considered when evaluating structural criteria, neglecting extreme conditions. Moreover, in these studies, a detailed stress-strain analysis is often replaced by the analysis of simpler criteria, such as root bending moment [20], simplified function of structural stresses [8] or rotor thrust [11].

1.4 Airfoil optimization

Another important limitation affecting most reported HAWT design optimization studies is that the airfoil design is not handled within the rotor optimization, although such inclusion plays a fundamental role in both aerodynamic and structural turbine performance. In fact, a commonly employed design procedure is to optimize the rotor blades by preselecting a set of existing available airfoils. This choice clearly limits the exploration of the design space, and inefficiently considers the cross-coupling interactions between the blade aerodynamics and the structural properties of the rotor. The interaction between wind turbine aerodynamics and structure is tied to the structural sizing of all wind turbine components, and therefore the design of the airfoil shapes affects not only the aerodynamic performance of the rotor, but directly determines the overall efficiency and LCOE of wind turbines. Designing the airfoils together with the rest of the blade therefore results in a wider exploration of the design space, and allows the airfoils to adapt to different local aerodynamic and structural conditions. In the course of an automated airfoil optimization process, the airfoil shapes are allowed to change, and therefore, at each iteration the aerodynamic characteristics of the airfoils need to

be determined. Therefore, the key issues that need to be addressed in design optimization of airfoils concern the definition of a suitable airfoil shape parametrization and the calculation of the airfoil aerodynamic performance. In a majority of airfoil design optimization applications, panel codes and Navier-Stokes (NS) computational fluid dynamics (CFD) solvers are used to evaluate airfoil aerodynamic performance. Airfoil parametrization is needed to relate the airfoil shape to numerical parameters, which are handled by the optimizer in order to find the optimum. To reduce the computational burden associated with the optimization process, airfoil parametrization should have a limited number of degrees of freedom, yet it should be able to describe any shape with good accuracy, exploring as many design alternatives as possible. Common parameterization techniques devised to numerically represent airfoil geometry for design optimization studies include: basis vector, domain element, partial differential equation, discrete, polynomial and spline, CAD-based, analytical, and freeform deformation. An exhaustive review of these methods can be found in [35]. The issue of optimizing the airfoil shapes with the rest of the blade was recently investigated by Petrone et. al. [12], Vesel and McNamara [15], Bottasso et al. [18] and Caboni et. al. [19]. These authors used XFOIL to determine the airfoil aerodynamic characteristics, and parametrized the airfoil shapes by means of B-splines [12] and Bézier curves [15, 18, 19].

1.5 Objectives, novelty and overview of the thesis

The main drive of the research work reported in this thesis was two-fold. On the one hand, it aimed at developing and assessing a novel integrated multidisciplinary design framework for the probabilistic aeroservoelastic design optimization of HAWT rotors. On the other hand, it aimed at demonstrating the effectiveness of the developed framework by performing the design optimization of a multi-megawatt HAWT rotor under environmental uncertainty. More specifically, the main objectives associated with the development of the design system were to:

- integrate, in a common computational framework, several simulation tools needed to assess the aeroservoelastic behavior of wind turbines, and determine their economical performance, and
- couple the multidisciplinary analysis module with an uncertainty propagation algorithm and an optimizer, and
- define the design space by developing a suitable wind turbine parametrization.

The main objective associated with the application of the design system was to optimize the aeroservoelastic design of 5-MW HAWT rotor so as to minimize mean and standard deviation

of its LCOE in the presence of uncertain wind speed. This probabilistic design scenario was described by Ning et al. [17]. The presented probabilistically optimal design was compared to a reference turbine based on the NREL 5-MW turbine [36], and a deterministic design, obtained without considering uncertainties in the optimization process.

The main novelty of this thesis is the presentation and demonstration of a fully integrated computational framework for the robust aeroservoelastic design optimization of HAWT rotors. The key feature of such a framework is that it concurrently optimizes airfoil shapes, external blade geometry and internal blade structure. As typical multidisciplinary HAWT rotor design systems optimize only blade chord and twist distributions, and internal blade structure making use of pre-selected airfoils, the design framework presented herein enables a wider exploration of the feasible design space, possibly leading to radically new and more efficient designs. In the developed framework, spanwise distributions of blade chord and twist, airfoil shapes, rotor speed and blade internal structural layup are optimized concurrently, enforcing structural constraints on ultimate, fatigue and buckling stresses, tip deflection and blade natural frequency, considering an extensive set of design cases. The design system is also probabilistic in that it can account for several uncertainty sources, and the study presented below focuses on probabilistic HAWT rotor design accounting for uncertain site-dependent mean wind speed. To the best of the writer's knowledge, there are no published reports on fully automated wind turbine multidisciplinary design optimization that simultaneously include realistic structural analysis/constraints based on three-dimensional (3D) models, the fully 3D blade shape parametrization of the blade, the airfoil geometry, and consider the stochastic variability of the wind frequency distribution.

The thesis is organized as follows. Chapter 2 presents an overview of the main topics and issues associated with the multidisciplinary analysis and design optimization of wind turbine rotors, providing details on the theoretical aspects and computational models commonly used to characterize the aeroservoelastic behavior of wind turbine rotors, as well as their economical performance. Advantages and disadvantages of the use of these methods in wind turbine design optimization are discussed. Chapter 3 presents the classical approach to the design optimization under uncertainty. The classical formulation of the RDO is explained along with the common approaches followed to solve such problems. This chapter also present an overview of the most popular methods for uncertainty propagation and optimization algorithms. A detailed description of the developed multidisciplinary and robust design optimization framework is reported in Chapter 4. This includes an integrated analysis module, based on aerodynamic, aeroelastic, structural and cost analysis models, coupled with an uncertainty propagation and optimization strategy. Chapter 5 deals with the development of the wind turbine parametrization, and it illustrates its use for the definition of the reference

5-MW HAWT rotor. In particular, this chapter aims to present the definition of the design space developed for the optimizations. Chapter 6 focuses on the HAWT design optimization under environmental uncertainty, formulating the probabilistic and deterministic optimization problems, and explaining the objective function and the constraints used. In this chapter the probabilistic and deterministic turbines are compared with the reference one. The main conclusions of the thesis and future work are summarized in Chapter 7.

Chapter 2

Multidisciplinary analysis of horizontal axis wind turbine rotors

Wind turbines are complex devices, and their overall characteristics result from the interaction of different disciplines, including aerodynamics, solid mechanics, control theory and economics. As already stated in Chapter 1, the design optimization of wind turbines is pursued by optimizing a figure of merit, or objective function, while fulfilling a number of requirements, or constraints. The objective function typically characterizes the economical performance of wind turbines, while the constraints ensure the structural integrity of their components throughout the expected turbine life. Both the objective function and constraints depend on the coupling among the aerodynamic and structural characteristics of the rotor, as well as the control strategy. This highlights the multidisciplinary nature of the design optimization of wind turbines. Therefore, the central part of a design system for the optimization of wind turbines should be constituted by an integrated multidisciplinary analysis module used to evaluate wind turbine aeroservoelastic performance. The aim of this chapter is to provide an overview of the topics which are fundamental to understanding the behavior of HAWTs. In particular, this chapter discusses the theoretical approaches and the computational tools that are commonly used to model wind turbines. For this purpose, three analysis areas have been identified and presented individually, namely: wind turbine rotor aeroservoelasticity, airfoil aerodynamics and cost.

2.1 Wind turbine rotor aeroservoelasticity

Aeroelasticity is a discipline that studies the interactions between the inertial, elastic, and aerodynamic forces that occur when an elastic body is exposed to a fluid flow. The com-

bination of aeroelasticity with control theory is known as aeroservoelasticity. In order to determine wind turbine power production and loads acting on the blades, the aeroservoelastic response of wind turbine rotors needs to be accurately assessed. The aeroservoelastic analysis of a wind turbine rotor is achieved by coupling the aerodynamic analysis with the structural one, integrating the control strategy needed to regulate the turbine operating conditions. For this purpose, several aeroelastic codes have been developed and used in the wind turbine industry, including FLEX4 [37], Bladed [38], Phatas [39], FAST [40] and HAWC2 [41]. These codes model the dynamic behavior of wind turbine rotors by coupling wind turbine aerodynamic and structural response to wind-inflow conditions, including a controller which, for a given rotor, defines the rotational speed at which the rotor operates at each wind speed. Aerodynamic analysis of the rotor, normally embedded in the aeroservoelastic analysis, is performed by means of an aerodynamic module as reported in Sect. 2.1.1. Aeroservoelastic simulations normally provide time-series data of the aerodynamic loads, as well as loads and deflections of the structural components of the wind turbine. The aeroservoelastic analysis of a wind turbine rotor, carried out with an aeroelastic code, generally requires the definition of the blade shape in terms of chord and twist distributions along the blade span, the aerodynamic characteristics of the blade airfoils, the mode shapes and the distributed structural properties of the blades, including cross-coupled stiffness properties and inertia properties. Distributed structural properties of the blades are commonly calculated be means of structural models as explained in Sect. 2.1.2. The evaluation of the aerodynamic characteristics of the airfoil blades is described later on in Sect. 2.2.

2.1.1 Wind turbine rotor aerodynamics

The aerodynamic behavior of a wind turbine determines the flow field around its rotor, and therefore it is closely related with the overall turbine performance. A correct evaluation of the rotor aerodynamics is needed to efficiently predict the interaction of the aerodynamic forces with the elastic structure of the rotor blades, and ensure their structural integrity. Aerodynamic analysis of wind turbine rotors can be performed either my means of blade element momentum (BEM) theory [42] or NS CFD [43]. BEM theory is based on simple models and can perform the aerodynamic analysis of a given rotor very quickly. Some of the most commonly used BEM codes include AeroDyn [44] and CCBlade [45], both developed by NREL. AeroDyn is a plug-in type code for interfacing with various NREL dynamics programs such as FAST, while CCBlade is a stand-alone code. CFD codes solve the NS equations numerically, incorporating several models to account for turbulence and laminar-turbulent transition. Both research [46] and commercial [47] CFD codes are currently available for the aerodynamic analysis of wind turbines. These codes are able to determine a

detailed description of the flow field around the rotor and several rotor diameters upstream and downstream of the rotor plane. Despite the rapid increase in computer power, calculation times associated with CFD are still excessive for their use in design optimizations requiring hundreds or thousands of rotor analyses. Therefore these methods are generally used for the evaluation of the rotor design, rather than being part of an iterative design optimization process. For this reason, BEM theory is the most common method used for the prediction of the aerodynamic rotor performance in wind turbine rotor design. The following two sections present respectively an overview of the BEM theory and the corrections needed to overcome its limitations.

Blade element momentum theory

The steady state aerodynamics of wind turbines is commonly analyzed by using momentum and blade element theory. Momentum theory refers to a control volume analysis of the forces acting on the blade based on the conservation of linear and angular momentum. Blade element theory refers to an analysis of forces at a blade section, as a function of blade geometry. According to the blade element theory, the forces on the blades of a wind turbine are expressed as a function of lift and drag coefficients and the angle of attack (AoA). The results of these approaches can be combined into what is known as strip theory or BEM theory. The BEM theory is based on the subdivision of the rotor disk into concentric rings of radial width dr and mean radius r. Each ring intersects the rotor blades forming blade elements or strips. The flow data and the aerodynamic forces acting on each strip are determined by solving two equations, obtained by combining linear and angular momentum conservation and classic lift and drag theory. One equation results from equating the ring axial thrust determined with the one-dimensional (1D) conservation of the linear momentum to the axial thrust computed with the lift and drag forces acting on the blade strips intersected by the ring. The other equation results from equating the ring torque determined with the 1D conservation of the angular momentum to the torque produced by the lift and drag forces acting on the intersected strips. The main geometric and aerodynamic parameters of a generic strip are depicted in Fig. 2.1, in which the section lift and drag forces are denoted by dF_L and dF_D respectively. Denoting by dT the thrust acting on a ring, the local thrust coefficient is $C_T = dT/(0.5\rho U^2 dA)$, where $dA = 2\pi r dr$ is the area of the ring, and ρ and U are the freestream density and velocity respectively. The local thrust coefficient computed using the conservation of linear momentum is:

$$C_T = 4a(1-a) \tag{2.1}$$

where a is the axial induction factor. The local thrust coefficient computed using lift and drag theory is:

$$C_T = \frac{\sigma_r(1-a)^2}{sin^2\varphi}(C_L\cos\varphi + C_D\sin\varphi) \tag{2.2}$$

where $\sigma_r = (N_b c)/(2\pi r)$ is the local solidity, N_b is the number of blades, c is the airfoil chord length, and C_L and C_D are the lift and drag coefficients respectively. The symbol φ denotes the angle of the relative wind velocity vector U_{rel} on the rotor plane. Its expression is $\varphi = \arctan[(1-a)/((1+a')\lambda_r)]$, where a' is the circumferential induction factor and $\lambda_r = \Omega r/U$ is the local speed ratio, where Ω is the angular speed of the rotor. U_{rel} is expressed as $U_{rel} = U(1-a)/\sin\varphi$. Equating Eqs. 2.1 and 2.2 yields one equation in the two unknowns a and a', since C_L and C_D are ultimately also functions of the induction factors. In fact, these force coefficients can be obtained with panel or CFD codes (see Sect. 2.2 for details) or experimental data as functions of the Reynolds number (Re), which depends on U_{rel} and the relative AoA α, the angle between the airfoil chord and U_{rel}. As shown in Fig. 2.1, $\alpha = \varphi - \theta_p$, where θ_p is the section pitch angle. This parameter depends only on geometric features, and its expression is $\theta_p = \theta_{p,0} + \theta_T$, where $\theta_{p,0}$ is the pitch angle of the blade and θ_T is the section twist angle. Denoting by dQ the torque acting on a rotor ring, the local torque coefficient is $C_Q = dQ/(0.5\rho U^2 r dA)$. The local torque coefficient computed using the conservation of angular momentum is:

$$C_Q = 4a'(1-a)\lambda_r \tag{2.3}$$

The local torque coefficient computed using lift and drag theory is:

$$C_Q = \frac{\sigma_r(1-a)^2}{sin^2\varphi}(C_L\sin\varphi - C_D\cos\varphi) \tag{2.4}$$

Equating Eqs. 2.3 and 2.4 yields another equation in the two unknowns a and a'. The nonlinear system resulting by equating the two expressions of C_T and C_Q for each strip need to be solved with an iterative routine based for instance on Newton's method or the method of successive substitution. The two-dimensional (2D) C_L and C_D data are stored in tables as functions of Re and α, and such data are computed in a pre-processing step. Once the flow state of each strip is known, the elemental power dP can be computed. The nondimensional local power coefficient $C_P = dP/(0.5\rho U^3 dA)$ can be expressed as follows:

$$C_P = \frac{\sigma_r(1-a)^2\lambda_r}{sin^2\varphi}(C_L\sin\varphi - C_D\cos\varphi) \tag{2.5}$$

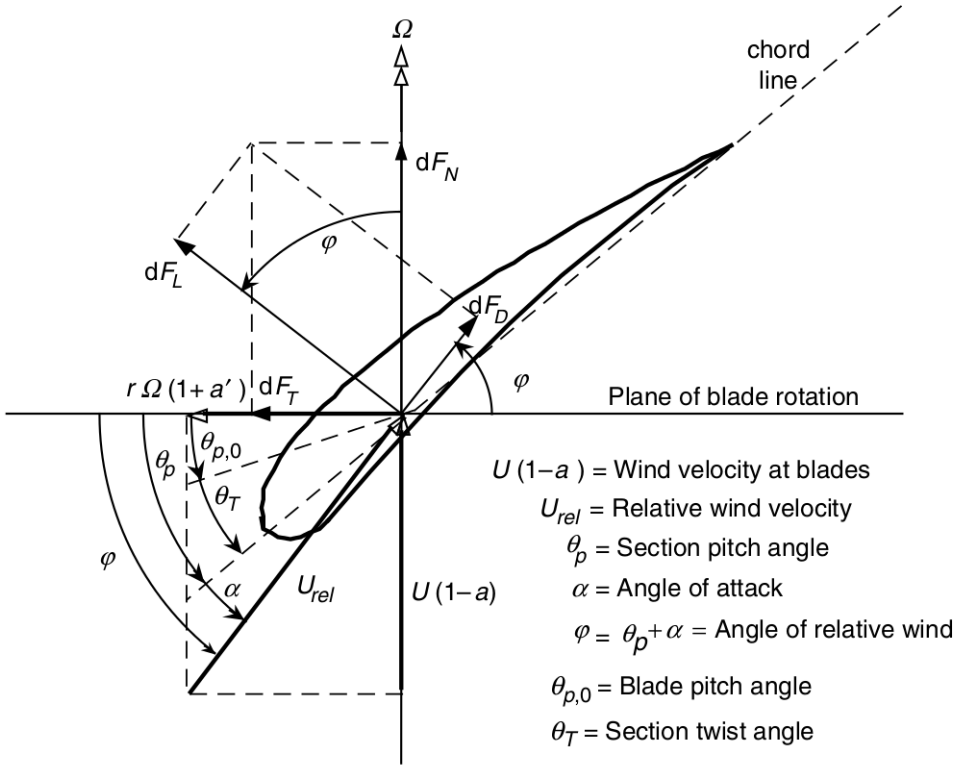

Fig. 2.1 Geometric and aerodynamic parameters of a generic blade strip. Image reproduced from [42].

The mechanical power of a given rotor corresponding to a particular value of U and Ω is determined by integrating dP from the blade root to its tip.

BEM theory corrections

Due to its simplicity, the BEM theory has several limitations. First of all, BEM calculations are static. This assumes that the flow field around the airfoils is always in equilibrium, and the flow accelerates instantaneously to adjust to new inflow or turbine operating conditions. In practice, however, the time taken by the flow-field to reach a steady-state can be relatively long, and, as explained below, the unsteady aerodynamic effects can play an important role in defining wind turbine operating conditions. Alternative methods based on the generalized dynamic wake model [48] have been used to overcome this limitation. Another limitation is tied to the fact that the BEM theory assumes that momentum is balanced in a plane parallel to the rotor. In the presence of large blade deflections this assumption will lead to inaccurate aerodynamic predictions. Moreover, BEM theory assumes the forces acting on the blade are essentially 2D, neglecting the complex 3D phenomena occurring over the rotating blades.

As discussed in Sect. 2.2, this limitation is circumvented by means of corrections directly applied on the static force coefficients of the airfoils. Other limitations, described below, come from the inability of BEM theory to model tip and hub losses, flows characterized by high induction factors, and skewed inflow.

Tip and hub loss correction. As shown in Fig. 2.2, helical vortices are shed from the blade tips into the wake. Tip vortices play an important role in defining the induced velocity field around the rotor. The most common approach to include tip loss in the BEM theory is

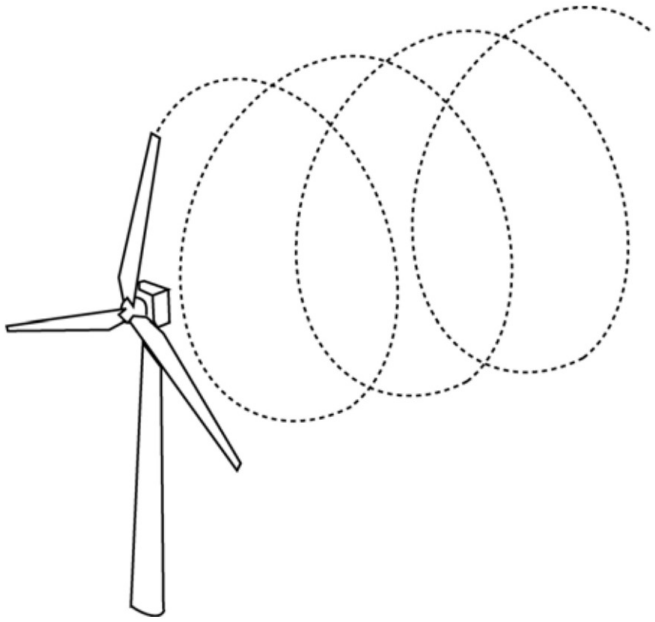

Fig. 2.2 Tip vortex pattern. Image reproduced from [44].

the one developed by Prandtl [42]. This method accounts for tip loss by means of a correction factor F_{tip} defined as follows:

$$F_{\text{tip}} = \left(\frac{2}{\pi}\right) \arccos\left(\exp\left[-\left\{\frac{N_b(R-r)}{2r\sin\varphi}\right\}\right]\right) \tag{2.6}$$

where R is the tip radius. When the tip correction is used, F_{tip} increases as the radial position approaches the blade tip, ranging from zero near the root to unity at the tip. To account for the vortices being shed at the blade hub, a correction for hub loss was developed. This correction is based on a correction factor F_{hub} expressed as:

$$F_{\text{hub}} = \left(\frac{2}{\pi}\right) \arccos\left(\exp\left[-\left\{\frac{N_b(r-R_{\text{hub}})}{2R_{\text{hub}}\sin\varphi}\right\}\right]\right) \tag{2.7}$$

where R_{hub} is the hub radius. The combined effect of tip and hub losses is taken into account by means of the Prandtl's correction factor F_{Pr} defined as:

$$F_{Pr} = F_{\text{tip}} F_{\text{hub}} \tag{2.8}$$

F_{Pr} is used to modify the momentum part of the BEM theory, replacing Eqs. 2.1 and 2.3 with the following ones:

$$C_T = 4F_{Pr}a(1-a) \tag{2.9}$$

$$C_Q = 4F_{Pr}a'(1-a)\lambda_r \tag{2.10}$$

Glauert correction. During normal operation, wind turbines typically work in the windmill state, in which the axial induction factor ranges from 0 to 0.5. When wind turbines operate at higher tip-speed ratios[1] (for example during startup or shutdown), the rotor enters in the so-called turbulent wake state [42], in which the axial induction factor is greater than 0.5. For axial induction factors greater than 0.5, BEM theory is not longer valid as, according to momentum theory, this operating state results when some of the flow in the far wake starts to propagate upstream. Flow reversal is not physically possible, and what actually happens is that the flow patterns through the wind turbine become much more complex than those predicted by momentum theory. Above an axial induction factor of 0.5, measured data indicate that thrust coefficient increases up to about 2 at an axial induction factor of 1. To compensate for this limitation Glauert [49] developed a correction to the rotor thrust coefficient based on experimental measurements. As shown in Fig. 2.3, in the windmill state, for axial induction factors up to 0.4, the mathematical relation between C_T and a is expressed by the classical momentum equation. For axial induction factors greater than 0.4, the Glauert correction takes over, intersecting tangentially the classical momentum curve. A numerical problem arises when the Prandtl's correction factor F_{Pr} is included in the classical momentum theory, as shown in Eq. 2.9. In this case, the application of the classical Glauert formulation leads to a gap between the classical momentum curve and the empirical one. In practice, the classical momentum curve and the Glauert curve do not intersect each other anymore. This gap creates a numerical discontinuity when a computer is used to iterate for the induction factor. To deal with this problem, Buhl [50] derived a modification of the

[1] Tip-speed ratio is the ratio between the tangential speed of the tip of a blade and the actual velocity of the wind.

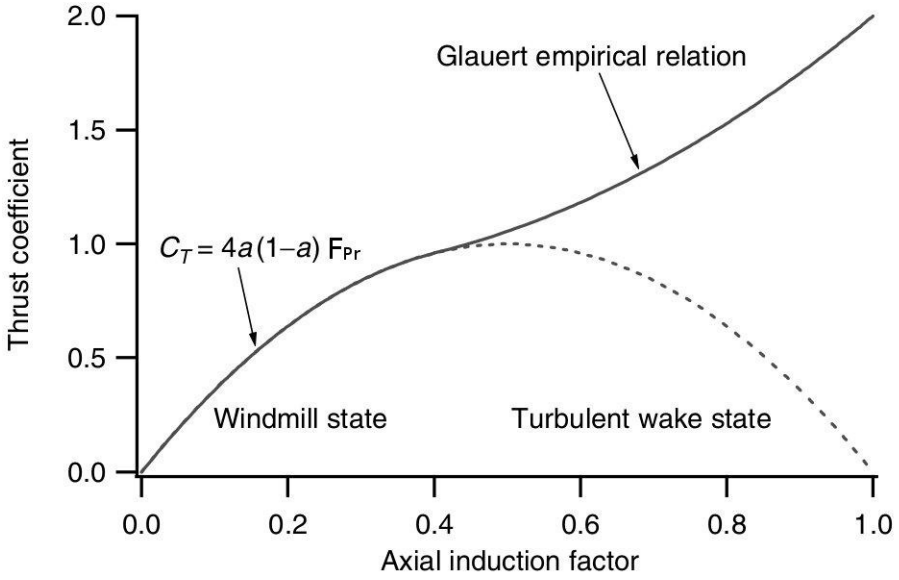

Fig. 2.3 Thrust coefficient versus axial induction factor. Image reproduced from [42].

Glauert correction including the Prandtl's correction factor as follows:

$$C_T = \frac{8}{9} + \left(4F_{Pr} - \frac{40}{9}\right) a + \left(\frac{50}{9} - 4F_{Pr}\right) a^2 \tag{2.11}$$

Taking into account the value of F_{Pr} explicitly, Eq. 2.11 always guarantees continuity between the classical momentum curve and the Glauert one.

Skewed wake correction. Wind turbines often operate with a non-zero yaw angle relative to the wind inflow. This determines a skewed wake behind the rotor. BEM theory needs to be corrected to account for such operating condition. Most of the available skewed wake corrections are based on an equation developed by Glauert [51]. This equation corrects the axial induction factor as follows:

$$a_{\text{skew}} = a\left[1 + K_{\text{skew}} \frac{r}{R} \cos(\psi)\right] \tag{2.12}$$

where K_{skew} is a function of the skew angle and ψ is the azimuth angle. In this case, since the axial induction factor depends on the value of ψ, the BEM equations outlined above need to be solved for each azimuth position. This correction has a limitation primarily due to the fact that it assumes a cylindrical wake, which is true only for lightly loaded rotors. Better predictions of the aerodynamics of wind turbines operating in yaw conditions can be achieved by using alternative methods based on the generalized dynamic wake model [48].

Unsteady aerodynamic effects. The turbulence associated with the wind and unsteady aerodynamic effects causes rapid fluctuations in the aerodynamic forces acting over the rotor blades, generating vibrations and important material fatigue. In particular, unsteady aerodynamic effects, such as those related to the tower shadow, dynamic stall and dynamic inflow (shortly described below), play a fundamental role on wind turbine operation, and their modeling can improve the accuracy of wind turbine rotor aerodynamic analysis.

Tower shadow. The wind speed experiences a deficit behind the tower. In downwind turbines, this causes a rapid drop in the power extracted by the rotor blades, and structural vibrations. A model accounting for the tower influence has been developed by Bak et al. [52]. This method models the influence of the tower on the local velocity field at all points around the tower. Fig. 2.4 shows the tower shadow model at a given point. According to this model, the tower wake decays in strength and grows in width as the distance from the tower increases.

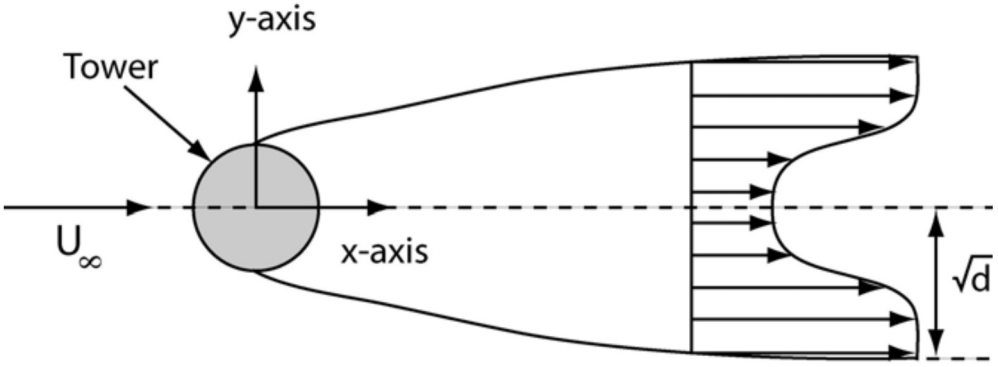

Fig. 2.4 Tower shadow model at a given point. In this picture, U_∞ is the freestream wind velocity, and d represents a characteristic length of the model. Image reproduced from [44].

Dynamic stall. When rapid changes in the AoA occur, for example when the rotor blades of a downwind turbine encounter the tower wake or due to the effects of rotor yaw, wind shear and turbulence, turbine blades can experience lift forces that are different (normally larger [53]) than those expected in static conditions. This effect is tied to the blade stall behavior, and it is normally referred to as dynamic stall. Dynamic stall is an unsteady mechanism than can occur when the AoA of an airfoil increases rapidly from below to above the static stall AoA. In this case, the flow over the airfoil can remain attached at angles of attack above the angle at which steady-state flow separation normally occurs. As shown in Fig. 2.5, under these circumstances, the airfoil can generate a higher lift coefficient than that

it would generate in the static cases. In extreme cases, dynamic stall can increase the lift

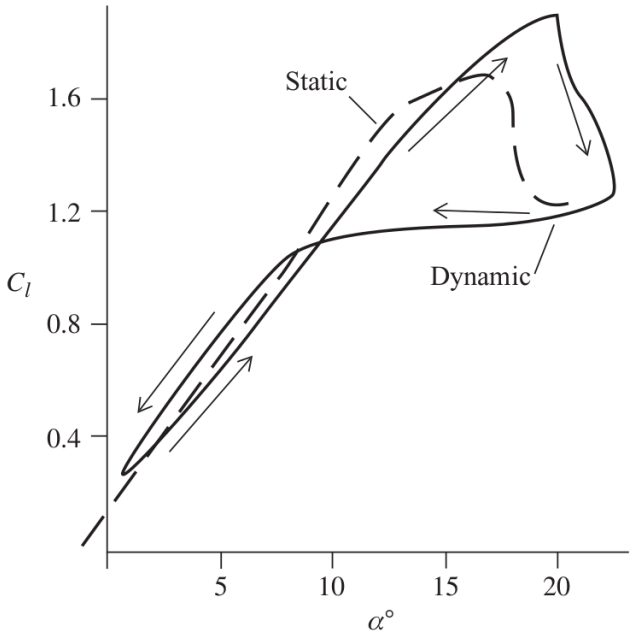

Fig. 2.5 Dynamic stall behavior. C_l and α represent the lift coefficient and the AoA, respectively. Image reproduced from [54].

coefficient by a factor of three [53]. The flow over the airfoil can then separate suddenly with the result that the lift coefficient drops and the drag coefficient increases. The loads experienced by a blade subject to dynamic stall can be large, causing significant fatigue damage. Dynamic stall also causes sudden variations of the pitching moment, resulting in important loads on the rolling bearings for the blade pitch motion. Several methods have been developed to model dynamic stall, such as those of Gormont [55] and Beddoes [56]. Details on the formulation of the Beddoes's model and its interaction within a BEM code can be found in the AeroDyn's theory manual [44]. Dynamic stall methods are not included in the design framework reported below.

Dynamic inflow. Dynamic inflow is related to the flow field response to turbulence and changes in rotor operation conditions (for example due to changes in the blade pitch angle or rotor speed). According to steady state aerodynamics, these changes should result in instantaneous changes in the flow field upstream and downstream of the rotor. However, during rapid changes the flow field cannot respond quickly enough to instantly establish steady state conditions. This results in aerodynamic conditions which may be different from the expected ones. The time scale of dynamic flow effects is on the order of D/U, the ratio

of the rotor diameter to the mean ambient flow velocity [42]. Therefore, the time scale of these effects is of the order of about 10 seconds [57]. Phenomena occurring slower than this can be treated using a steady state analysis. More details on dynamic inflow and its modeling can be found in [57–59]. Dynamic inflow methods are not included in the design framework reported below.

2.1.2 Structural analysis of the rotor blades

The design of wind turbine blades is an involved process mainly due to the complexity of their aerodynamic shape and internal structural characteristics. Indeed, wind turbine blades are made of composite laminates, constituted by anisotropic[2] layup distributed non-uniformly along the blade span. This means that the internal structural layup of composite laminates varies across the blade span from root to tip. As mentioned above, the structural analysis of rotor blades is primarily required to compute mode shape and distributed stiffness and inertial properties needed by wind turbine aeroelastic codes. Moreover, the structural analysis of the blades is needed to verify their structural integrity against ultimate and fatigue limits. Ultimate load analysis refers to the assessment of material strength (through a stress-strain analysis), blade tip deflection and structural stability (i.e., buckling), while fatigue load analysis concerns fatigue strength. The extraction of the structural properties of the blade and the stress-strain, blade tip deflection and buckling analyses are normally carried out using structural codes. Fatigue calculations involve the use of specific algorithms to process load histories in order to determine the damage accumulation. The initial part of this section deals with different methods commonly used to perform the structural analysis of wind turbine blades and fatigue calculations.

The realistic ultimate and fatigue loads, that turbine components are subjected to, need to be accurately assessed. Such loads are normally generated by running a series of aeroelastic simulations under different operating and environmental conditions, covering most of the situations that wind turbines likely experience during their lifetime. As mentioned in Chapter 1, these conditions are prescribed by standards, such as the IEC standard [28]. Wind conditions considered by these standards are normally fed into aeroelastic codes by means of wind input files. The concluding part of this section will describe the structure of such files, and explain how they can be generated.

[2] Anisotropy is the property of being directionally dependent, as opposed to isotropy, which implies identical properties in all directions.

Methods for the structural analysis of wind turbine blades

Finite element method (FEM) codes, such as ANSYS [60], Abaqus [61], SolidWorks [62] and NuMAD [63], can be used to perform the structural analysis of wind turbine blades, accurately accounting for complex geometric shapes and composite structural layup. FEMs rely on numerical approximation techniques that divide a component or structure into discrete regions (the finite elements) and the response is described by a set of functions that represent the displacements or stresses in those regions [64]. These models are able to accurately provide the span-variant properties of the blades, and describe the strain-stress fields in detail. The use of FEM techniques is however computationally expensive, requiring the generation of a computational mesh, and complex post-processing. In the preliminary design stages, where a huge number of different configurations may be evaluated, FEM approaches may become impractical. Therefore the structural analysis in the aeroelastic design optimization of wind turbine rotors generally relies on simpler and faster models. The rest of this section will review some of these simplified structural models tailored towards composite rotor blades, and featuring various solution techniques.

PreComp [65] is a popular NREL code developed to provide span-variant structural properties for composite blades. These structural properties encompass: flap, lag (edgewise), axial (with respect to the blade pitch axis), and torsion stiffnesses, as well as orientation of principal axes, density, and moments of inertia. This code is based on the classical lamination theory (CLT) with a shear-flow approach. Details on the CLT and the shear-flow theory can be found respectively in [66, 67] and [68]. It should be noted that PreComp cannot be used to perform stress-strain analysis. Therefore, in the framework of this research, alternative structural codes, not based on FEMs, yet featuring stress-strain analysis capabilities, have been reviewed.

Co-Blade [69] is a computationally efficient open source structural analysis and design code developed by Sale. This code includes all of the same capabilities of PreComp, adding analysis of load induced strain, stress, deflection, buckling, optimization capabilities, and graphical post-processing capabilities. Making use of a blend of CLT, Euler-Bernoulli theory [68, 70, 71] and shear flow theory applied to composite beams, Co-Blade predicts both the distributed structural properties of composite wind turbine blades, and their deformation and material stress fields. The Co-Blade's technical approach models the turbine blade as a cantilever beam subject to aerodynamic loads, self-weight, buoyancy[3], and centrifugal forces. As a consequence, the beam undergoes bending, axial deflection (i.e., tension and compression along the longitudinal axis of the beam), and twist (i.e. torsion about the longitudinal axis of the beam). The linear differential equations of equilibrium for a cantilever

[3]Buoyancy is an upward force exerted by a fluid that opposes the weight of an immersed object.

beam are then used to determine the shear force and bending moment distributions along the beam length. Co-Blade considers the beam cross sections are assumed to be thin-walled, closed, and single- or multi-cellular. The cross-section of the cantilever beam is discretized as a connection of flat composite laminates, as illustrated in Fig. 2.6. Although each composite

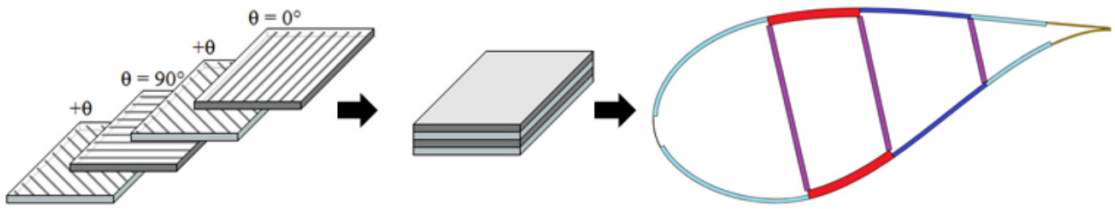

Fig. 2.6 Modeling of the turbine blade cross-section. Each section is discretized as a connection of composite laminate plates, each made up of a number of different laminas (θ represent the orientation of each lamina's principal material direction with respect to the blade axis). Image reproduced from [69].

laminate is a stack of a number of different laminas (each characterized by its own material and constitutive properties), the CLT is used to evaluate the effective mechanical properties (i.e., Young's modulus, shear modulus, Poisson's ratio, thickness, and density) of each laminate, treating it as a single structural element. Therefore, the beam cross-section is made up of a number of discrete areas, or panels, of homogeneous material (represented through different colors in Fig. 2.6). The panels, made up of consistent flat composite laminates, are characterized by the effective mechanical properties computed via CLT. Each panel then contributes to the global cross-sectional properties, which are computed by the method of Young's modulus weighted properties [70, 71]. Once that global cross-sectional properties are known, the deflections and the beam effective axial stress and effective beam shear stress are computed under the assumption of an Euler-Bernoulli beam. The calculation of the beam effective shear stress is based on a shear flow approach. The distributions of the effective beam stresses from the Euler-Bernoulli theory are eventually converted into the equivalent in-plane distributed loads on the flat composite laminates, so that the strains and stresses of each lamina can be recovered by means of CLT. Co-Blade follows the approach described in [72, 73] to perform the linear buckling analysis of the blade. In this approach the top and the bottom surfaces of the blade are modeled as curved plates subject to a combination of compression and shear loads, while the shear webs (connecting the top surface to the bottom one) are modeled as flat plates subject to combined bending and shear. Practically, panel buckling is treated by means of a buckling criteria R expressed by a dimensionless

number which is lower than 1 if the effective stresses in a panel have not exceeded the critical buckling stresses.

Another simple and fast structural code has been developed and presented by Ashuri et al. [74]. This code, based on the Euler-Bernoulli theory, enables both the extraction of structural properties of a composite wind turbine blade and the calculation of its bending stress field. In fact, unlike Precomp, this code includes the calculation of the cross-sectional area moments of inertia, allowing one to determine the bending stresses σ. For this purpose, the classic formula for determining σ, in a beam under simple bending, can be used as follows:

$$\sigma = \frac{My}{I_x} \tag{2.13}$$

where M is the moment about the neutral axis[4], y is the perpendicular distance to the neutral axis, and I_x is the cross-sectional area moments of inertia about the neutral axis.

As mentioned above, blade mode shapes are required to perform rotor aeroelastic simulations by means of aeroelastic codes. Moreover, to avoid blade resonance issues, rotor blades should be designed considering their natural frequencies. As explained in Chapter 6, the first natural frequency of the blade should be above the maximum rotor blade passing frequency. All the structural codes described in this section cannot cope with the calculation of either the blade mode shapes or the blade natural frequencies. The preprocessor BModes [75] is a NREL tool able to generate coupled modes and natural frequencies for a turbine blade or a tower. BModes uses distributed inertial and stiffness properties of the blade and tower along their longitudinal axis. For blade mode shapes calculation, BModes also requires the rotational speed of the blade to calculate the rotational stiffening and its pitch angle as input. From the solution of the associated eigenvectors, polynomial expressions of the mode shapes are calculated. The calculation of the the natural frequencies are carried out in the same way, including the stiffening effects of rotation.

Fatigue

Fatigue is defined as the progressive and localized structural damage that occurs when a material is subject to cyclic loading. Due to the spatiotemporal variability of the wind and the rotation of the rotor, wind turbine components, such as the rotor blades, tower and drive train, indeed experience cycling loads throughout their lifespan, and therefore they need to be designed against fatigue. The most common approach to design wind turbine mechanical

[4]The neutral axis is an axis in the cross section of a beam subject to bending along which there are no longitudinal stresses or strains.

parts against fatigue is to keep structural stress below threshold of fatigue limit, normally represented by a parameter indicating the fatigue damage accumulation.

Fatigue analysis for wind turbines is typically carried out by running a large number of aeroelastic (time-domain) simulations under different wind conditions, determining the fatigue loads expected over the lifetime of the turbine. Fatigue loads on each primary component of the turbine are then post-processed. MLife [76] is a NREL code, created to compute fatigue estimates resulting from time-series load data files. This code accumulates fatigue damage due to fluctuating loads. These fluctuating loads are broken down into individual hysteresis cycles each characterized by a load mean and range, using the rainflow counting method according to the ASTM standard [77]. In practice, the rainflow counting algorithm reduces a complex spectrum of varying loads into a simple set (or series) of cycles defined by a given mean and amplitude. MLife assumes that the fatigue damage accumulates linearly and independently for each of these cycles according to the Miner's rule [78]. Thus, the total damage resulting from all cycles is given by:

$$D = \sum_i \frac{n_i}{N_i(L_i^{RF})} \tag{2.14}$$

where L_i^{RF} denotes a given cycle's load range about a fixed load-mean value and $N_i(L_i^{RF})$ represents the number of cycles, characterized by L_i^{RF}, that would lead to failure. n_i represents the actual count of cycles characterized by L_i^{RF}. When n_i is equal to $N_i(L_i^{RF})$ failure occurs, and this corresponds to D equal to 1. Load ranges are related to cycles to failure by means of the S-N curve (or Wöler curve) which can be modeled as follows:

$$N_i = \left(\frac{L^{ult} - |L^{MF}|}{\left(\frac{1}{2} L_i^{RF}\right)} \right)^m \tag{2.15}$$

where L^{ult} is the ultimate design load of the component, L^{MF} is the fixed lead mean and m is the Wöler exponent, depending on the considered component.

Wind input files for structural verification

Standards, such as the IEC standard, prescribe wind conditions at which aeroelastic simulations should be carried out in order to verify structurally wind turbine components. These conditions encompass normal, extreme, steady and turbulent wind speeds. Several codes have been devised to generate wind files for HAWT structural verification suitable for aeroelastic simulations. In particular, NREL developed wind simulators primarily for use with AeroDyn-based programs, such as IECWind [79] and TurbSim [80]. In AeroDyn, wind

conditions are prescribed by two types of wind input files, namely the hub height wind files and the full field turbulence files. The former typology represents wind conditions, varying in time, by means of the values of horizontal wind speed at the hub, wind direction, vertical wind speed, horizontal wind shear, power law vertical wind shear, linear vertical wind shear and gust velocity. For the exact definition of these parameters one can refer to [44]. The latter wind file typology represents all three components of the wind vector varying in space and time. This permits a detailed simulation of a wind field with the appropriate scales and correlation of atmospheric turbulence. IECWind is a program developed to create AeroDyn hub height wind files, modeling the steady conditions outlined in the IEC standard. TurbSim is a tool able to generate numerical simulations of a full field flow, containing turbulence structures that reflect realistic spatiotemporal turbulent velocity fields. TurbSim can be used to create AeroDyn full field turbulence files, according to the turbulent conditions prescribed by the the IEC standard.

2.2 Wind turbine airfoil aerodynamics

Because of its simplicity, short execution time and robustness, BEM theory is the most widely used approach for the aerodynamic analysis and design of wind turbine rotors. Using BEM codes, the aerodynamic characteristics of the airfoils making up the rotor blades must be provided in terms of lift and drag coefficients as a function of Re and AoA. Aerodynamic characteristics used in BEM calculations are typically based on 2D airfoil lift and drag polars determined either by means of wind tunnel experiments, or computational models such as panel codes, and NS CFD. It should be noted that it is unlikely that experimental airfoil data can be used in design optimization systems which optimize concurrently the design of the blade planform and its airfoils, because many diverse and new airfoils are examined by the optimizer, and, in general, the optimal design will feature new airfoils for which experimental data do not exist. This highlights the need of using sufficiently fast computational tools for airfoil aerodynamics. Sect. 2.2.1 will review the most popular approaches for the aerodynamic analysis of wind turbine airfoils.

Using only 2D airfoil polars, however, BEM codes are not able to model the complex 3D effects that occur over the rotor blades. These effects are dominated by those associated with blade rotation, applying centrifugal and Coriolis forces to the air flow. Several empirical and semi-empirical corrections, called 3D corrections, have been devised to account for these effects. 3D corrections, described in Sect. 2.2.2, are normally applied directly to the 2D airfoil polars.

Under normal operating conditions, wind turbine blades can experience very high AoAs, causing aerodynamic stall. Therefore, to model these situations using BEM theory, 2D airfoil polars must be provided in both pre- and post-stall regions. However, wind tunnel airfoil tests are normally available until stall, and due to model limitations, airfoil analysis codes often cannot predict accurately airfoil performance beyond stall. To deal with this issue global post-stall methods have been developed. These empirical methods, often accounting for all 3D effects (including the rotational effects), are able to determine pre- and post-stall airfoil characteristics starting from the pre-stall 2D polars. Sect. 2.2.3 will illustrate the most used global post-stall methods.

2.2.1 Methods for the airfoil aerodynamic analysis

Over the last two decades, several panel codes have been developed and used to perform the aerodynamic analysis and design of new airfoils. Tangler et al. [81] used the Eppler Airfoil Design and Analysis Code to develop the NREL S8xx airfoil series. However, the most popular panel code is XFOIL [81], developed by Drela at the Massachusetts Institute of Technology (MIT). XFOIL is a panel code with a strong viscid–inviscid interaction scheme, giving realistic boundary layer properties. The code uses the e^N method to predict transition. The use of XFOIL enables a rapid and efficient calculation of the airfoil performance in the linear region of the lift curve below stall; the code, however, is known to usually overestimate the maximum lift coefficient [82], and not to provide reliable predictions of the force coefficients beyond the stall inception point, after which significant flow separations occur. The near stall predictions of XFOIL appear to be particularly inaccurate for thicker airfoils like the NREL S809 airfoil [83]. Improved near-stall force predictions could be obtained with RFOIL [82], the variant of XFOIL developed at Delft University of Technology (TU Delft), the National Aerospace Laboratory of the Netherlands (NLR) and the Energy research Centre of the Netherlands (ECN). RFOIL features a better convergence around the maximum lift due to the use of different velocity profiles for the turbulent boundary layer and due to modifications in the calculation of the turbulent boundary layer shape factor [84]. This improves the prediction of the maximum lift coefficient. An alternative to panel codes for the 2D aerodynamic analysis of airfoils is represented by the use of CFD codes. With respect to panel codes, CFD codes give better agreement with experimental measures, and provide a more detailed description of the flow field around the airfoil. The use of CFD is in fact reaching a level of maturity enabling it to accurately predict airfoil aerodynamics well beyond the AoA of maximum lift [85]. However, the computational and preparation time associated with the use of CFD codes is much more onerous than that required by panel

codes. For this reason, the use of panel codes represents the preferred approach in most of the wind turbine design optimization applications.

2.2.2 Rotational effects and 3D corrections

When used with accurate 2D airfoil lift and drag polars, BEM theory provides reasonable performance predictions when the airfoils are at AoAs below stall. However, when a significant part of the blade is subject to AoAs above stall, which lead to separated flow conditions, the direct use of 2D airfoil polars results in a poor agreement between measured and predicted power production and loads [86]. In fact, in the presence of local blade stall, the BEM theory lacks the ability to model the complex 3D effects occurring over rotating blades. These effects are primarily associated with the centrifugal and Coriolis effects, which are important mainly over the inboard part of the blade, experiencing a high degree of flow separation. In particular, rotational effects lead to the augmentation of rotating blade aerodynamic properties, including stall delay and lift enhancement. In fact, blade rotation delays turbine blade stall and significantly amplifies blade aerodynamic loads. This phenomenon depends on viscous flow effects in the presence of centrifugal and Coriolis influences, and occurs routinely during turbine operation.

At present, the physics behind rotational augmentation of HAWT blade aerodynamics remains only partially characterized and understood. Recently, the combined use of experimental measurements and CFD models have provided new insights into turbine blade flow fields and aerodynamic forces produced in the presence of rotational augmentation [87, 88]. In particular, these studies highlighted that the mechanisms underlying augmented aerodynamic force production during rotating conditions can be related to the flow field resulting over the stalled portion of the blade, involving boundary layer separation and shear layer impingement. In a stalled blade section, boundary layer separation normally occurs at some point over the suction surface. As the AoA increases, boundary layer separation moves forward towards the leading edge, starting from the trailing edge vicinity. As shown in Fig. 2.7, when the boundary layer separation reaches the leading edge, the resulting shear layer arches over the blade suction surface, and finally impinges on the aft portion of the blade chord. Between separation and impingement, the shear layer surrounds a region of intense recirculation strongly reminiscent of vortical structure, within which the flow is directed outboard and forward towards the leading edge. The degree to which rotating forces are augmented is correlated with the size of this vortical structure. Separation reaches the leading edge first at inboard locations and arrives later at the leading edge at outboard locations. For this reason, at inboard blade regions the vortical structure is bigger and stronger, and

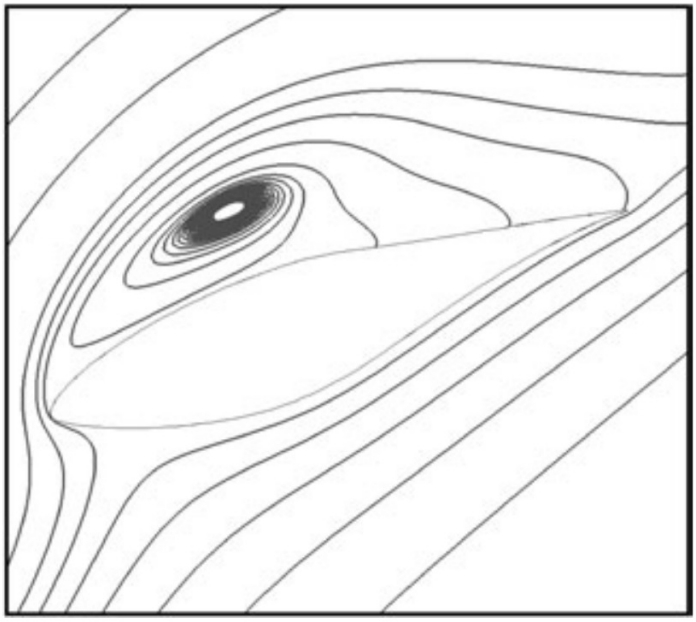

Fig. 2.7 Flow field over a stalled section of a rotating blade, showing boundary layer separation and shear layer impingement. A region of intense recirculation above the blade's suction surface is also depicted. Image reproduced from [87].

therefore these regions undergo the greatest degree of rotational augmentation. At outboard blade regions, where the flow is attached, there is little or no rotational augmentation.

Several 3D correction models have been developed to deal with centrifugal and Coriolis forces. In general, these models correct the 2D lift and drag coefficients at each radial station of the blade, accounting for different flow conditions along the blade span. The most commonly used 3D corrections include those developed by: Snel et. al. [89], Du and Selig [90], Chaviaropoulos and Hansen [91], Lindenburg [92], Bak et al. [93] and Eggers et al. [94]. The first four of these models determine the 3D lift and drag coefficients, denoted respectively by $C_{L,3D}$ and $C_{D,3D}$, by means of the following equations:

$$C_{L,3D} = C_{L,2D} + f_{C_L}\left(\frac{c}{r},...\right)\Delta C_L \tag{2.16}$$

$$C_{D,3D} = C_{D,2D} + f_{C_D}\left(\frac{c}{r},...\right)\Delta C_D \tag{2.17}$$

in which $C_{L,2D}$ and $C_{D,2D}$ are respectively the 2D lift and drag coefficients, and c/r is the local blade solidity, where c is the local chord and r is the local radius. ΔC_L and ΔC_D denote respectively the difference between the C_L and C_D that would exist if the flow did not separate (taken respectively as $C_L = 2\pi(\alpha - \alpha_{\text{lift=0}})$ and $C_D = C_{D,\alpha=0}$, where α is the AoA, $\alpha_{\text{lift=0}}$ is

the zero-lift AoA and $C_{D,\alpha=0}$ is the drag coefficient at an AoA of zero) and the C_L and C_D measured in a 2D configuration including separation (i.e., $C_{L,2D}$ and $C_{D,2D}$). Hence:

$$\Delta C_L = 2\pi(\alpha - \alpha_{\text{lift}=0}) - C_{L,2D} \tag{2.18}$$

$$\Delta C_D = C_{D,\alpha=0} - C_{D,2D} \tag{2.19}$$

Accounting for the local blade solidity, these corrections vary along the blade span. In particular, the closer the considered radial section is with respect to the blade root (i.e., the lower r is), the stronger the 3D correction on the aerodynamic polars is. In fact, as already mentioned above, blade sections near the blade root are subjected to stronger 3D effects due to rotation.

The functions f_{C_L} and f_{C_D} depend on the selected model. The model developed by Snel et. al. provides a correction only for C_L. According to this method, the function f_{C_L} is expressed as follows:

$$f_{C_L} = 3\left(\frac{c}{r}\right)^2 \tag{2.20}$$

The model of Du and Selig expresses f_{C_L} and f_{C_D} as follows:

$$f_{C_L} = \frac{1}{2\pi}\left[\frac{1.6(c/r)}{0.1267}\frac{a-(c/r)^{\frac{d}{\Lambda}\frac{R}{r}}}{b+(c/r)^{\frac{d}{\Lambda}\frac{R}{r}}} - 1\right] \tag{2.21}$$

$$f_{C_D} = \frac{1}{2\pi}\left[\frac{1.6(c/r)}{0.1267}\frac{a-(c/r)^{\frac{d}{2\Lambda}\frac{R}{r}}}{b+(c/r)^{\frac{d}{2\Lambda}\frac{R}{r}}} - 1\right] \tag{2.22}$$

$$\Lambda = \frac{\Omega R}{\sqrt{U^2+(\Omega r)^2}} \tag{2.23}$$

where Ω is the rotor speed, R is the tip radius, U is the freestream wind velocity and $a = b = d$ = 1. According to the Chaviaropoulos and Hansen model, f_{C_L} and f_{C_D} are expressed as:

$$f_{C_L} = f_{C_D} = a\left(\frac{c}{r}\right)^h \cos^n(\theta_{p,0}) \tag{2.24}$$

where $\theta_{p,0}$ is the blade pitch angle, a = 2.2, h = 1 and n = 4. The Lindenburg's model accounts for a correction just for C_L as follows:

$$f_{C_L} = 3.1\left(\frac{\Omega r}{U_{rel}}\right)^2\left(\frac{c}{r}\right)^2 \tag{2.25}$$

where U_{rel} is the relative wind velocity. An example of the application of 3D correction models to a stall-regulated wind turbine can be found in [83].

2.2.3 Global post-stall methods

The accurate prediction of airfoil aerodynamic characteristics in both pre- and post-stall regions is a key step in the BEM-based rotor analysis and design, and this holds for both stall- and pitch-regulated wind turbines. Indeed, in the former case, flow stall is induced to control the mechanical power extracted by the rotor, while in the latter case blade airfoils experience very high AoAs during the rotor start and stop transients, and in parked conditions, especially over the inboard part of the blade. For this reason, a number of global post-stall methods have been developed and presented. These codes, generally derived empirically, provide a method for calculating lift and drag polars of wind turbine airfoils, in both the pre-stall and post-stall regions, including all aerodynamic 3D effects (tip and hub losses, rotational effects, etc.). In fact, the attribute " global" of such models refers to their ability to capture the net aerodynamic effects related to the blade geometry rather than detailed flow physics characteristics (as is the case of 3D corrections seen in Sect. 2.2.2). Typically, global post-stall methods correct and extend the pre-stall airfoil lift and drag coefficient curves. Figure 2.8 shows an example of measured force coefficients at high AoAs for two typical wind turbine airfoils measured in a wind tunnel.

Viterna and Corrigan [96] proposed an empirical method to correct and extend 2D airfoil aerodynamic characteristics. This method evaluates the lift and drag coefficients at high AoA starting from the stall point of the airfoil lift curve. The equations of this method were developed by matching the experimental power curves of different rotors using a BEM code. This means that all aerodynamic effects are included, and this specifically covers the rotational effects that are dominant at the inboard part of the blade. The Viterna and Corrigan method start from correcting the 2D pre-stall polars in order to account for the blade aspect ratio effects. In fact, 2D polars do not consider the effect due to a finite blade aspect ratio, such as tip and hub losses. The size of the aspect-ratio effects on airfoil coefficients in the attached regime can be estimated using the classical equations for converting infinite-length airfoil data to finite-length data, from the work of Munk, Glauert, and Prandtl [97]. According to these equations, the finite aspect ratio pre-stall lift and drag coefficients and the AoA can be calculated as follows:

$$C_L = C_{L_0} \tag{2.26}$$

$$C_D = C_{D_0} + \frac{C_L^2}{\pi AR} \tag{2.27}$$

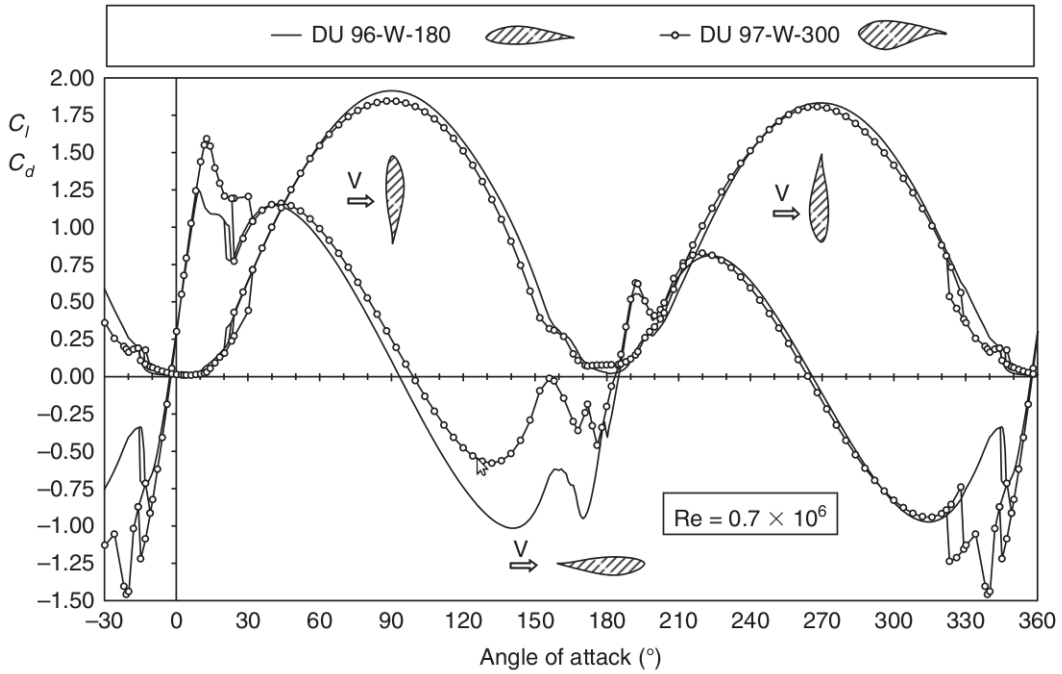

Fig. 2.8 Measured lift and drag coefficients of two airfoils at high AoAs. Image reproduced from [95].

$$\alpha = \alpha_0 + \frac{57.3 C_L}{\pi AR} \tag{2.28}$$

where 0 is a subscript denoting infinite aspect ratio (or 2D) data, and AR is the blade aspect ratio. In this model, AR is defined as the blade radius divided by the chord length at 75% of the span. The equations for the calculation of the post-stall aerodynamic coefficients constituting the Viterna and Corrigan method are partly based on the variation of the maximum flat plate drag coefficient, $C_{D,\max}$, with AR, as given in Eqs. 2.29 and 2.30:

$$C_{D,\max} = 1.111 + 0.018 AR \quad \text{for } AR < 50 \tag{2.29}$$

$$C_{D,\max} = 2.01 \quad \text{for } AR \geq 50 \tag{2.30}$$

Post-stall drag coefficient is then determined as follows:

$$C_D = C_{D,\max} \sin^2 \alpha + K_1 \cos \alpha \tag{2.31}$$

where the parameter K_1 is expressed as:

$$K_1 = \frac{C_{D,s} - C_{D,\max} \sin^2 \alpha_s}{\cos \alpha_s} \tag{2.32}$$

Post-stall lift coefficient can be calculated as:

$$C_L = \frac{1}{2} C_{D,\max} \sin 2\alpha + K_2 \frac{\cos^2 \alpha}{\sin \alpha} \tag{2.33}$$

where:

$$K_2 = (C_{L,s} - C_{D,\max} \sin \alpha_s \cos^2 \alpha_s) \frac{\sin \alpha_s}{\cos^2 \alpha} \tag{2.34}$$

The index s denotes stall conditions defining the starting point for the Viterna and Corrigan curves. In the stall point, the pre-stall characteristics match with the calculated post-stall performance of the airfoil. Recently, Tangler and Kocurek [86] used the Viterna and Corrigan method to calculate the power output of a stall regulated wind turbine, using various combinations of input parameters of the correction model.

Recently, an alternative set of empirical equations for modeling lift and drag coefficients in the pre- and post-stall regimes, called AERODAS, has been developed by Spera [98], extending the Viterna and Corrigan model. Based on empirically derived equations, AERODAS provides a method for calculating stall and post-stall lift and drag characteristics of rotating airfoils, using as input a limited amount of pre-stall 2D aerodynamic data of the blade airfoils. More precisely, the equations of the AERODAS model were determined through an empirical approach based on the trends of experimental data available for a wide variety of airfoils. These trends were then modeled by a set of algebraic equations providing the best fit of the available experimental data. An important feature of the AERODAS equations is that they correct the infinite-length airfoil (or 2D) data for the effect of blade aspect ratio, explicitly taking into account the tip and the hub losses. Figure 2.9 presents the comparison between experimental 2D lift and drag coefficients for the NREL S809 airfoil [99], and those calculated through the AERODAS equations for an infinite blade aspect ratio and a blade aspect ratio of 15.3.

An alternative method, called *StC*, has been developed and presented by Lindenburg [100]. This approach is based on empirical relations that define the pre- and post-stall lift and drag curve, including the effects associated with blade rotation and finite aspect ratio.

AirfoilPrep [101] is a NREL spreadsheet devised to generate the airfoil data needed by BEM codes. This code applies rotational augmentation corrections for 3D delayed stall to pre-stall 2D airfoil polars, by using Du's method [90] to augment the lift and Eggers'

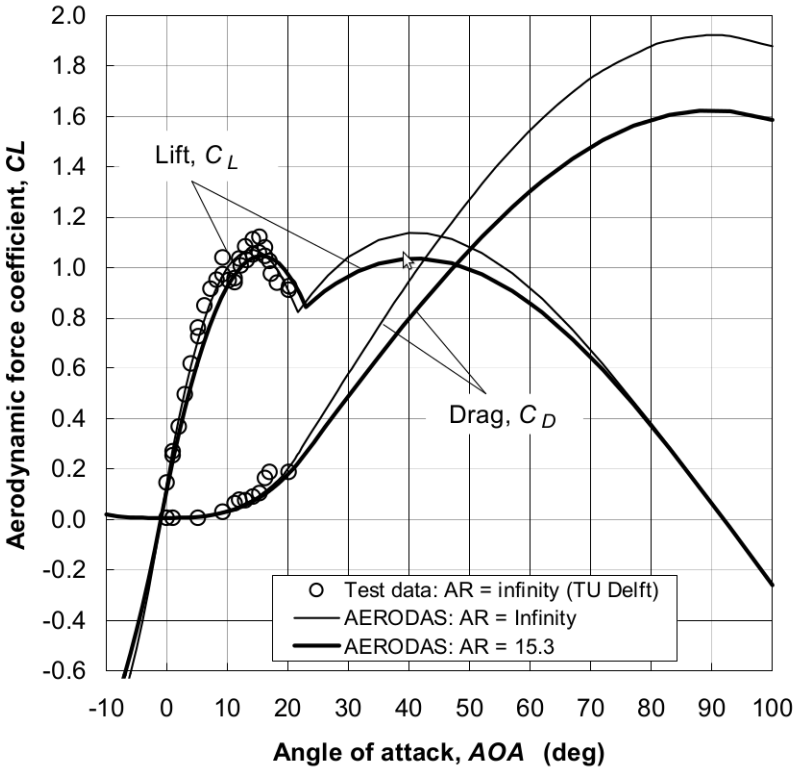

Fig. 2.9 Comparison of measured and calculated lift and drag coefficients for the NREL S809 airfoil. Infinite blade aspect ratio test data [99] are compared with the coefficients calculated by means of AERODAS, using an infinite blade aspect ratio and a blade aspect ratio of 15.3. Image reproduced from [98].

method [94] to modify the drag. The corrected polars are then extended to the full 360 deg range of AoAs by means the Viterna and Corrigan method [96].

2.3 Cost of energy

As already mentioned in Chapter 1, the reference metric in wind turbine design optimization is the LCOE, defining the economical performance of wind turbine systems distributed (or levelized) over their lifetime. Therefore, a reliable model is needed to accurately estimate the cost of electricity generated by wind turbines. For three-bladed, upwind, pitch-controlled, variable-speed wind turbines, the DOE/NREL scaling model [102] is a tool developed by NREL to accomplish this goal. The purpose of this model is to evaluate the impact of any change of the design of a wind turbine on the system cost. To do so, the model considers several elements of the system, such as the initial capital cost (ICC), the O&M cost, the levelized replacement/overhaul cost (LRC) and the AEP. To determine the cost of wind turbine

components for different sizes and configuration, the DOE/NREL scaling model uses scaling relationships. Component costs, all referred to 2002 United States dollars, in most cases are function of rotor diameter, machine rating and tower height. In the DOE/NREL scaling model, cost scaling functions have been developed for major components and subsystems. Much of the data used to develop scaling functions for machines of greater than 1 to 2 MW is based on conceptual designs. Many components are scaled using functions that are close to a cubic relationship. This is what would normally be expected for technologies that did not undergo design innovations as they grew in size [102]. According to the DOE/NREL scaling model, the LCOE, expressed in $/kWh, can be calculated by using the following equation:

$$\text{LCOE} = \frac{(\text{FCR} \cdot \text{ICC}) + \text{LC} + \text{O\&M} + \text{LRC}}{\text{AEP}} \tag{2.35}$$

where FCR is the fixed charge rate and LC is the lease cost. The ICC, expressed in $, is the sum of the wind turbine capital cost (TCC) and the balance of station (BOS) cost. The primary wind turbine components considered within the TCC include: rotor, drive train, nacelle, control, safety system, and condition monitoring and tower. BOS cost includes the costs associated with foundation/support structure, roads, civil work, assembly and installation, electrical interface/connections and engineering permits. When offshore wind turbines are assessed, additional components are included in the BOS cost, including: marinization, port and staging equipment, personal access equipment, scour protection, surety bond, and offshore warranty premium. The FCR represents the annual amount per dollar of ICC needed to cover the capital cost, a return on debt and equity, and various other fixed charges, such as depreciation, income tax, and property tax and insurance. According to the DOE/NREL scaling model, FCR is set equal to 11.85% per year. The product of FCR and ICC appearing in the LCOE formula is therefore expressed in $/year. LC represents the annual cost charged for the rental or lease of the land or ocean bottom. LC is expressed in units of $/year. O&M cost is the yearly cost associated with operations and maintenance, and it is expressed in $/year. O&M cost normally includes labour, parts, and supplies for scheduled and unscheduled turbine maintenance, parts and supplies for equipment and facilities maintenance, and labour for administration and support. LRC is the cost associated with major replacements and overhauls, distributed over the wind turbine's lifetime, and it is expressed in $/year. Measured in kWh/year, AEP is the annual energy output of the turbine based on a given annual average wind speed distribution. The AEP calculation is adjusted for mechanical and electrical conversion losses. As an example, the cost estimate from the DOE/NREL scaling model citecost for a 3 MW offshore wind turbine is reported in Fig. 2.10.

Offshore Turbine		
Cost in $	2005	
Component	Component Costs $1000	Component Mass kgs
Rotor	**477**	**50,957**
Blades	319	28,809
Hub	69	14,842
Pitch mchnsm & bearings	83	6,162
Spinner, Nose Cone	6	1,145
Drive train,nacelle	**1,425**	**88,552**
Low speed shaft	59	6,251
Bearings	32	1,650
Gearbox	408	20,973
Mech brake, HS cpling etc	6	
Generator	211	10,426
Variable spd electronics	266	
Yaw drive & bearing	46	4,312
Main frame	168	40,426
Electrical connections	150	
Hydraulic, Cooling system	41	240
Nacelle cover	38	4,273
Control, Safety System, Condition Monitoring	**60**	
Tower	**415**	**200,762**
Marinization (13.50% of Turbine and Tower System)	**321**	
TURBINE CAPITAL COST (TCC)	**2,698**	**340,271**
Monopile foundation/Support Structure	1,114	
Transportation	281	
Port and staging equipment	74	
Turbine Installation	371	
Electrical Interface/Connect	926	
Permits, Engineering, Site Assessment	119	
Personnel Access Equipment	64	
Scour Protection	204	
Surety Bond (Decomissioning - 3.0% of ICC)	176	
BALANCE OF STATION COST (BOS)	**3,331**	**0**
Offshore Warranty Premium (15.00% of Turbine and Tower System)	**357**	
Initial capital cost (ICC)	**6,386**	**340,271**
Installed Cost per kW (cost in $)	**2,129**	**113,424**
Turbine Capital per kW sans BOS & Warranty (cost in $)	**899**	**113,424**
Levelized Replacement Cost $ per year	55	
O&M $ per turbine/yr	215	
Bottom Lease Cost	12	
CAPACITY FACTOR	**38.13%**	
Net ANNUAL ENERGY PRODUCTION Energy MWh (AEP)	**10020**	
Fixed Charge Rate	11.85%	
COE $/kWh	**0.0950**	

Fig. 2.10 Cost estimate from the DOE/NREL scaling model [102] for a 3 MW offshore wind turbine (rotor diameter equal to 90 m and hub height equal to 80 m).

Chapter 3

Robust design optimization

In the last decades, advanced computer-based simulation approaches and tools have been successfully integrated in the design optimization of engineering systems, shortening the overall design cycle, providing better understanding of the operating behavior of the systems under consideration, and lowering design costs. However, it is still difficult to determine a confidence level in the information provided by numerical methods and models. This complexity is primarily related to the uncertainties associated with the inputs of any computation attempting to represent a physical system, or the errors affecting numerical algorithms and computer codes. Therefore, in order to ensure high design quality and reliability, uncertainty quantification should be considered and integrated in the optimization process. RDO is a field of optimization theory that deals with optimization problems in which a certain measure of robustness is sought against uncertainty. In other words, RDO aims at finding a design with the best possible performance expectation and minimal performance sensitivity to factors causing uncertainty. RDO problems are generally formulated and solved in terms of multiple objective functions, typically involving the mean and variance of one or more deterministic objective functions. RDO is performed by following a sequence of three main stages. The first stage consists of identifying, qualifying and quantifying the sources of uncertainty associated with the system to be optimized. In this stage, the uncertainty of the random input variables of the system is characterized probabilistically, by means of a given PDF. The second stage consists of propagating the input uncertainty through the analysis system to obtain a probabilistic description of the objective functions and constraints. Robust forms of objectives and constraints are generally expressed as a function of the mean and variance of their deterministic counterparts. Finally, the third stage consists of optimizing the robust objectives subject to the robust constraints. The robust optimal design is such that the mean of the objectives is optimized and their variance are minimized. The aim of this chapter is to describe the mathematical formulation of a RDO problem, providing an overview of the

most common approaches used for uncertainty propagation and numerical optimization. In the following sections, the methods included in the robust design optimization framework developed in this work will be highlighted.

3.1 Mathematical formulation of robust design optimization problems

An optimization problem aims at finding the best configuration of a system from all feasible configurations. This is normally accomplished by optimizing a set of parameters characterizing the system under consideration, denoted by design variables $\boldsymbol{b} \in \Re^n$, where n is the number of design variables, without violating some constraints $g_j,\ j = 1,2,...,r$, where r is the number of constraints. The optimization process is driven by an objective function f, which is typically minimized by varying the aforementioned design variables. A deterministic design optimization problem (i.e., an optimization problem that does not consider uncertainty) can be formulated as follows:

$$\begin{aligned} \text{Find: } & \boldsymbol{b} \in \Re^n \\ \text{to minimize: } & f(\boldsymbol{b}) \\ \text{subject to: } & g_j(\boldsymbol{b}) \leq 0,\ j = 1,2,...,r \\ \text{and: } & \boldsymbol{b_L} \leq \boldsymbol{b} \leq \boldsymbol{b_U} \end{aligned} \tag{3.1}$$

where $\boldsymbol{b_L}$ and $\boldsymbol{b_U}$ are respectively the lower and upper bounds of the design variables' variability ranges. The evaluation of the objective function and constraints is performed numerically, through a numerical model of the system under investigation. Considering the input uncertainty associated either with the design variables or other parameters of the system, the objective function and constraints can be modified as follows:

$$f(\boldsymbol{b}) \longrightarrow f(\boldsymbol{b} + \boldsymbol{z}^b, \boldsymbol{p} + \boldsymbol{z}^p) \tag{3.2}$$

$$g_j(\boldsymbol{b}) \longrightarrow g_j(\boldsymbol{b} + \boldsymbol{z}^b, \boldsymbol{p} + \boldsymbol{z}^p) \tag{3.3}$$

where $\boldsymbol{p} \in \Re^m$ is a constant vector defining the design parameters, and m is the number of design parameters. Like the design variables, the design parameters refer to some characteristics of the system under consideration. Design parameters, however, do not drive the optimization process (i.e., they are not optimized) as the design variables do. In a proba-

bilistic optimization framework, design parameters can be affected by uncertainty (as well as the design variables), and therefore they need to be treated explicitly in the optimization problem. $\boldsymbol{z}^b \in \Re^n$ and $\boldsymbol{z}^p \in \Re^m$ are respectively the uncertainties associated with the design variables and the design parameters. Therefore, in a probabilistic framework, f and g_j are random quantities induced by the uncertainties z_i^b and z_i^p, respectively. The RDO problem is practically treated by introducing deterministic operators applied to f and g_j, denoted respectively by F and G_j, in order to eliminate the random character of f and g_j, and thus to reduce their dependencies on z. Hence, the resulting design optimization problem under uncertainty can be expressed as:

$$\begin{aligned} \text{Find: } & \boldsymbol{b} \in \Re^n \\ \text{to minimize: } & F(\boldsymbol{b}, \boldsymbol{p}, \boldsymbol{z}) \\ \text{subject to: } & G_j(\boldsymbol{b}, \boldsymbol{p}, \boldsymbol{z}) \leq 0,\ j = 1, 2, ..., r \\ \text{and: } & \boldsymbol{b_L} \leq \boldsymbol{b} \leq \boldsymbol{b_U} \end{aligned} \tag{3.4}$$

Generally, the probabilistic objective function and constraints F and G_j are defined in terms of the statistical moments (i.e., mean, variance, skewness, kurtosis, etc.) of f and g_j, respectively. Considering the objective function f in the form given by Eq. 3.2, the mean μ_f and the variance σ_f^2 can be expressed as follows [29]:

$$\begin{aligned} \mu_f(\boldsymbol{b}, \boldsymbol{p}) = E[f(\boldsymbol{b} + \boldsymbol{z}^b, \boldsymbol{p} + \boldsymbol{z}^p)] = \int\int ... \int f(\boldsymbol{b} + \boldsymbol{z}^b, \boldsymbol{p} + \boldsymbol{z}^p) \kappa_1(z_1^b) ... \kappa_n(z_n^b) \\ \times \nu_1(z_1^p) ... \nu_0(z_0^p) \mathrm{d}z_1^b ... \mathrm{d}z_n^b \mathrm{d}z_1^p ... \mathrm{d}z_0^p \end{aligned} \tag{3.5}$$

$$\begin{aligned} \sigma_f^2(\boldsymbol{b}, \boldsymbol{p}) = E[(f(\boldsymbol{b} + \boldsymbol{z}^b, \boldsymbol{p} + \boldsymbol{z}^p) - \mu_f(\boldsymbol{b}, \boldsymbol{p}))^2] = \int\int ... \int [f(\boldsymbol{b} + \boldsymbol{z}^b, \boldsymbol{p} + \boldsymbol{z}^p) - \mu_f]^2 \\ \times \kappa_1(z_1^b) ... \kappa_n(z_n^b) \nu_1(z_1^p) ... \nu_0(z_0^p) \mathrm{d}z_1^b ... \mathrm{d}z_n^b \mathrm{d}z_1^p ... \mathrm{d}z_0^p \end{aligned} \tag{3.6}$$

where $\kappa_i(z_i^b)$ and $\nu_i(z_i^p)$ are the joint PDFs of the uncertainty factors z_i^b and z_i^p, respectively.

The RDO problem formulated in Eq. 3.4 highlights that the robustness can be sought against the variability of both the objective function and constraints. The combined probabilistic considerations of the objective function and constraints is known as reliability optimization. In practice, reliability optimization extends the concept of RDO, the main aim of which is to maximize the performance (expressed by the objective function) and simultaneously to minimize the sensitivity of the performance with respect to random parameters. Indeed, reliability optimization aims at optimizing the objective function, limiting its

variations with respect to the variations of the uncertain variables (as explained in Sect. 3.2), while satisfying all constraints within a range of tolerance (as described in Sect. 3.3).

3.2 Robust design optimization methods

For both constrained and non-constrained RDO problems, the robustness of the objective function is pursued by minimizing the probabilistic objective function F. A number of approaches have been used to solve RDO problems, formulating the minimization of F in different ways. The simplest RDO approach, known as Bayes Principle [12], is to define the probabilistic objective function F as the mean of f, denoted by μ_f. Hence:

$$F(\boldsymbol{b},\boldsymbol{p},\boldsymbol{z}) = \mu_f(\boldsymbol{b},\boldsymbol{p}) \tag{3.7}$$

Another simple approach is the weighted sum method [29], in which F is defined as the weighted averaged of the mean and variance of f, respectively denoted by μ_f and σ_f^2. Thus:

$$F(\boldsymbol{b},\boldsymbol{p},\boldsymbol{z}) = \alpha_w[\mu_f(\boldsymbol{b},\boldsymbol{p})/\mu_f^*] + (1-\alpha_w)[\sigma_f^2(\boldsymbol{b},\boldsymbol{p})/\sigma_f^{2*}] \tag{3.8}$$

where α_w and $(1-\alpha_w)$ are the weights associated with μ_f and σ_f^2, respectively. μ_f^* and σ_f^{2*} are used to normalize μ_f and σ_f^2, respectively. The approach known as constrained optimization [12], aims at minimize μ_f, keeping σ_f^2 lower or equal to a certain value σ_f^{2*}. Thus, the constrained optimization can be formulated as follows:

$$\begin{cases} \text{minimize:} & \mu_f(\boldsymbol{b},\boldsymbol{p}) \\ \text{subject to:} & \sigma_f^2(\boldsymbol{b},\boldsymbol{p}) \leq \sigma_f^{2*} \end{cases} \tag{3.9}$$

Finally, the last approach reviewed in this section is to formulate the RDO problem as a multi-objective approach [12], whereby the mean and the variance of f are minimized concurrently as follows:

$$\begin{cases} \text{minimize:} & \mu_f(\boldsymbol{b},\boldsymbol{p}) \\ \text{minimize:} & \sigma_f^2(\boldsymbol{b},\boldsymbol{p}) \end{cases} \tag{3.10}$$

3.3 Robustness of constraints

In a deterministic constrained optimization, the optimizer ensures that a given constraint does not exceed a certain limit value. In the presence of uncertainty, constraints are characterized by a certain variability, defined by a given PDF. A very simple approach to treat uncertain

constraints in the course of an optimization process is to consider their mean value. This means that the mean value of each constraint must be kept below a certain threshold. In this case, the probabilistic form of constraints G_j becomes:

$$G_j(\boldsymbol{b},\boldsymbol{p},\boldsymbol{z}) = \mu_{g_j}(\boldsymbol{b},\boldsymbol{p}) \tag{3.11}$$

where μ_{g_j} is the mean of g_j. Considering just the mean value of each constraint however does not guarantee that all values that the constraints assume are below their limit values. Therefore, if a high reliability related to the constraints is sought, each constraint needs be verified probabilistically, within a confidence interval. This means that a given constraint does not exceed a specific limit for a given number of cases (expressed by a confidence level). Confidence intervals of the constraints depend on their PDFs. Expressing confidence intervals in terms of mean and standard deviation, the probabilistic form of constraints G_j can be written as:

$$G_j(\boldsymbol{b},\boldsymbol{p},\boldsymbol{z}) = \mu_{g_j}(\boldsymbol{b},\boldsymbol{p}) + k_{g_j}\sigma_{g_j}(\boldsymbol{b},\boldsymbol{p}) \tag{3.12}$$

where σ_{g_j} is the standard deviation of g_j, and k_{g_j} is a suitably chosen coefficient, determining the length of the confidence interval.

3.4 Methods for uncertainty propagation

Within a probabilistic optimization framework, the problem of uncertainty propagation consists of characterizing probabilistically the objective function and constraints given the PDFs of all the uncertain input parameters. The output quantities of interest (QoIs), i.e., the objective function and constraints, are characterized probabilistically by defining a PDF. As already stated, the QoIs are typically defined probabilistically by their statistical moments, such as mean and variance. Let's simplify Eq. 3.5 and Eq. 3.6 by considering a generic objective function f depending on the uncertain variables $\boldsymbol{z}$. In this case, the mean value and the variance of f, denoted respectively by μ_f and σ_f^2, can be written as:

$$\mu_f = E[f(\boldsymbol{z})] = \int_{-\infty}^{+\infty} f(\boldsymbol{z}) p_{\boldsymbol{z}}(\boldsymbol{z}) d\boldsymbol{z} \tag{3.13}$$

$$\sigma_f^2 = E[(f(\boldsymbol{z}) - \mu_f)^2] = \int_{-\infty}^{+\infty} [f(\boldsymbol{z}) - \mu_f]^2 p_{\boldsymbol{z}}(\boldsymbol{z}) d\boldsymbol{z} \tag{3.14}$$

where $p_{\boldsymbol{z}}$ is the joint PDF of the random variable $\boldsymbol{z}$. For engineering problems of practical interest, the solution of Eq. 3.13 and Eq. 3.14 is normally achieved numerically, by means of

an uncertainty propagation method. Several methods have been developed to deal with this problem. The numerical approximation of the statistical moments needs a trade-off between computational time and accuracy. In this section, two approaches are described, namely sampling and deterministic methods. In the robust design optimization framework developed in this work the Latin hypercube sampling and the deterministic URQ technique (reviewed below) are included.

3.4.1 Sampling methods

Techniques based on sampling are simple uncertainty propagation approaches, relying on a number of simulations (or realizations) performed by selecting given input values. Once all realizations have been performed, the outputs are collected and analyzed in order to characterize statistically the outcome. Common approaches based on sampling are the Monte Carlo method [103] and the Latin hypercube sampling strategy [104].

Monte Carlo method

The Monte Carlo method is the oldest and the most used sampling technique. It is based on a random sampling within the variability ranges of the stochastic inputs. More precisely, it generates a random sample of m points, taken for each uncertain input variable of a model. Each of the m points corresponds to the sampling point $\boldsymbol{z_i}$. The selection of these sample points is independent of the PDFs associated with the input variables. The outcome is generally organized as a histogram and the estimations for the mean and the variance of f are determined as follows:

$$\mu_f = \frac{1}{m}\sum_{i=1}^{m} f(\boldsymbol{z_i}) \tag{3.15}$$

$$\sigma_f^2 = \frac{1}{m-1}\sum_{i=1}^{m} [f(\boldsymbol{z_i}) - \mu_f]^2 \tag{3.16}$$

The advantages of this method are that it is simple and does not require any modification of the analysis system, as the method requires a sequence of deterministic analyses. However, in order to obtain an accurate estimation of the statistical moments, a large number of realizations are required, as the method converges to the exact solution only for a number of samples going to infinity. The convergence however does not depend on the number of uncertain variables. The use of Monte Carlo methods, although they always provide the right answer, might be prohibitive in some cases due to time requirements.

Variance reduction techniques [105], such as control variates, antithetic variables, stratified, Latin hypercube (described below), and descriptive sampling [106], have been developed to achieve faster convergence for Monte Carlo methods.

Latin hypercube sampling

Latin hypercube sampling is one of the methods developed to accelerate the Monte Carlo approach, increasing its efficiency. Using the Monte Carlo method it might happen that a large number of sample points are clustered closely, maybe leaving unexplored other regions. Latin hypercube sampling aims at spreading the sample points more evenly across all possible values. In this method, the range of variability of each input stochastic variable is divided in M intervals with equal probability. M samples are then taken, one from each interval. The samples for each input are then shuffled so that there is no correlation between the inputs. The estimation of the mean and variance of f is then obtained by means of Eq. 3.15 and Eq. 3.16.

Both Monte Carlo method and Latin hypercube sampling are unbiased[1] estimation techniques. Using these methods the estimated statistical moments approach their theoretical values as the sample size increases. Given a number of samples, the Latin hypercube sampling achieves a better estimation of the statistical moments with respect to the Monte Carlo method. In other words, Latin hypercube sampling requires a lower number of samples than the Monte Carlo method to achieve the same accuracy. In particular, it has been demonstrated [107] that the same accuracy can be achieved by means of Monte Carlo method and Latin hypercube sampling by using m^2 and m samples, respectively.

3.4.2 Deterministic methods

Deterministic methods rely on the assumption that the probabilistic forms (such as means and variances) of the outputs of interests can be expressed by approximated functions. This approximation simplifies the original stochastic problem, reducing the computational requirements associated with uncertainty propagation. Therefore, this approximation requires the formulation of new mathematical problems. The most popular deterministic methods include the Taylor-based method of moments [103] and the stochastic expansion method [103]. The former method is based on the representation of the outputs by means of a lower order Taylor expansion, while the latter one uses Fourier like expansions to approximate the output. Recently, a novel fast deterministic method, named URQ [32], has been developed and

[1] The bias of an estimator, in statistics, is the difference between this estimator's expected value and the true value of the parameter being estimated.

presented. As already mentioned in Chapter 1, this method was used to perform the robust design of airfoils [32] and wind turbine blades [19, 20] under probabilistic uncertainty. The rest of this section will be devoted to the presentation of the aforementioned deterministic uncertainty propagation algorithms, namely the Taylor-based method of moments, the stochastic expansion method and the URQ technique.

Taylor-based method of moments

Taylor-based method of moments represents a generic stochastic output QoI, $f(\boldsymbol{z})$, by using a Taylor expansion with respect to the uncertain input variable set around a reference solution (e.g., the mean value). The Taylor series of $f(\boldsymbol{z})$ developed around the mean of the uncertain input variable vector $\boldsymbol{\mu}_z$ can be written as:

$$\begin{aligned} f(\boldsymbol{z}) = f(\boldsymbol{\mu}_z) + \sum_{p=1}^{n}\left(\frac{\partial f}{\partial z_p}\right)\Delta z_p + \frac{1}{2}\sum_{p=1}^{n}\sum_{q=1}^{n}\left(\frac{\partial^2 f}{\partial z_p \partial z_q}\right)\Delta z_p \Delta z_q \\ + \frac{1}{6}\sum_{p=1}^{n}\sum_{q=1}^{n}\sum_{r=1}^{n}\left(\frac{\partial^3 f}{\partial z_p \partial z_q \partial z_r}\right)\Delta z_p \Delta z_q \Delta z_r \\ + \frac{1}{24}\sum_{p=1}^{n}\sum_{q=1}^{n}\sum_{r=1}^{n}\sum_{s=1}^{n}\left(\frac{\partial^4 f}{\partial z_p \partial z_q \partial z_r \partial z_s}\right)\Delta z_p \Delta z_q \Delta z_r \Delta z_s \\ + O(\Delta \boldsymbol{z}^5) \end{aligned} \tag{3.17}$$

where $\Delta z_p = z_p - \mu_{z_p}$, and the partial derivatives of f with respect to the input variables are computed at $\boldsymbol{z} = \boldsymbol{\mu}_z$. The remainder of the series is denoted by $O(\Delta \boldsymbol{z}^5)$, including all terms of order five and higher. Considering independent input variables, μ_f and σ_f^2 can be determined by substituting Eq. 3.17 into Eq. 3.13 and Eq. 3.14, as follows:

$$\begin{aligned} \mu_f = \int_{-\infty}^{+\infty} f(\boldsymbol{z}) p_{\boldsymbol{z}}(\boldsymbol{z}) d\boldsymbol{z} = f(\boldsymbol{\mu}_z) + \frac{1}{2}\sum_{p=1}^{n}\left(\frac{\partial^2 f}{\partial z_p^2}\right)\sigma_{z_p}^2 \\ + \frac{1}{6}\sum_{p=1}^{n}\left(\frac{\partial^3 f}{\partial z_p^3}\right)\gamma_{z_p}\sigma_{z_p}^3 + \frac{1}{24}\sum_{p=1}^{n}\left(\frac{\partial^4 f}{\partial z_p^4}\right)\Gamma_{z_p}\sigma_{z_p}^4 \\ + \frac{1}{8}\sum_{p=1}^{n}\sum_{\substack{q=1 \\ q\neq p}}^{n}\left(\frac{\partial^4 f}{\partial z_p^2 \partial z_q^2}\right)\sigma_{z_p}^2\sigma_{z_q}^2 + O(\boldsymbol{\sigma}_{\boldsymbol{z}}^5) \end{aligned} \tag{3.18}$$

$$\begin{aligned}\sigma_f^2 = \int_{-\infty}^{+\infty} [f(\boldsymbol{z}) - \mu_f]^2 p_{\boldsymbol{z}}(\boldsymbol{z}) d\boldsymbol{z} = \sum_{p=1}^{n} \left(\frac{\partial f}{\partial z_p}\right) \sigma_{z_p}^2 \\ + \sum_{p=1}^{n} \left(\frac{\partial^2 f}{\partial z_p^2}\right) \left(\frac{\partial f}{\partial z_p}\right) \gamma_{z_p} \sigma_{z_p}^3 + \sum_{p=1}^{n} \sum_{\substack{q=1 \\ q \neq p}}^{n} \left(\frac{\partial^3 f}{\partial z_p^2 \partial z_q}\right) \left(\frac{\partial f}{\partial z_q}\right) \sigma_{z_p}^2 \sigma_{z_q}^2 \\ + \frac{1}{2} \sum_{p=1}^{n} \sum_{\substack{q=1 \\ q \neq p}}^{n} \left(\frac{\partial^2 f}{\partial z_p \partial z_q}\right) \sigma_{z_p}^2 \sigma_{z_q}^2 + \frac{1}{3} \sum_{p=1}^{n} \left(\frac{\partial^3 f}{\partial z_p^3}\right) \left(\frac{\partial f}{\partial z_p}\right) \Gamma_{z_p} \sigma_{z_p}^4 \\ + \frac{1}{4} \sum_{p=1}^{n} \left(\frac{\partial^2 f}{\partial z_p^2}\right)^2 (\Gamma_{z_p} - 1) \sigma_{z_p}^4 + O(\boldsymbol{\sigma}_{\boldsymbol{z}}^5)\end{aligned} \tag{3.19}$$

where the term $\boldsymbol{\sigma}_{\boldsymbol{z}}^5$ denotes all monomials of order five or higher. The partial derivatives of f with respect to the input variables are computed at $\boldsymbol{z} = \boldsymbol{\mu}_z$. The skewness and kurtosis of the variable z_p can be defined as:

$$\gamma_{z_p} = \frac{E[(z_p - \mu_{z_p})^3]}{\sigma_{z_p}^3} \tag{3.20}$$

$$\Gamma_{z_p} = \frac{E[(z_p - \mu_{z_p})^4]}{\sigma_{z_p}^4} \tag{3.21}$$

The Taylor-based method of moments relies on a model approximation, achieved by truncating the Taylor series to a lower order. The most common and simple Taylor-based method of moments used in the literature is first-order[2]. This means that only the first-order derivatives are taken into account. The approximation of the stochastic outputs is associated with a reduction in computational costs. However, even for relatively small spread of the input variables, the accuracy of the method may be severely spoiled by nonlinearities in the system response. To increase the accuracy of this method, one can retain higher-order derivatives. The computational efficiency of this method depends on the available methods for calculating derivatives. Several techniques have been devised to calculate derivatives of the simulation outputs, such as automatic differentiation and the complex variable method.

Stochastic expansion method

Stochastic expansion methods expand the QoIs in a series of random variables. Polynomial chaos expansion [108] and stochastic collocation [109] are two related techniques belonging

[2]Orders of approximation refer to formal or informal terms for how precise an approximation is.

to this category. Once the series is determined, the statistical moments can be calculated deterministically. Stochastic expansion methods have been defined in terms of intrusive and non-intrusive formulations. The latter formulation allows one to use the original code, treating it as a "black box". The former formulation instead involves defining a new problem. Focusing on the non-intrusive version of this category of methods, f, supposed square integrable, can be written as:

$$\begin{aligned} f(\boldsymbol{z}) = a_0 H_0 + \sum_{i1=1}^{\infty} a_{i1} H_1(u_{i1}) + \sum_{i1=1}^{\infty} \sum_{i2=1}^{i1} a_{i1,i2} H_2(u_{i1}, u_{i2}) \\ + \sum_{i1=1}^{\infty} \sum_{i2=1}^{i1} \sum_{i3=1}^{i2} a_{i1,i2,i3} H_3(u_{i1}, u_{i2}, u_{i3}) + \ldots \end{aligned} \tag{3.22}$$

where $\boldsymbol{u}$ is a vector of standard normal variables (which can be derived from $\boldsymbol{z}$ by resorting to the Rosenblatt transformation [48]), H_q is a qth-order multidimensional Hermite polynomial, and the a_i are suitable coefficients. For further details on stochastic expansion methods, the reader can refer to [31, 103, 108, 109]

URQ technique

URQ method is a simplified technique belonging to the quadrature method family [32]. According to this method, μ_f and σ_f^2 can be determined by the following equations:

$$\mu_f = W_0 f(\boldsymbol{\mu}_z) + \sum_{p=1}^{n} W_p \left[\frac{f(\boldsymbol{z}_p^+)}{h_p^+} - \frac{f(\boldsymbol{z}_p^-)}{h_p^-} \right] \tag{3.23}$$

$$\begin{aligned} \sigma_f^2 = \sum_{p=1}^{n} \Bigg\{ W_p^+ \left[\frac{f(\boldsymbol{z}_p^+) - f(\boldsymbol{\mu}_z)}{h_p^+} \right]^2 + W_p^- \left[\frac{f(\boldsymbol{z}_p^-) - f(\boldsymbol{\mu}_z)}{h_p^-} \right]^2 \\ + W_p^{\pm} \frac{[f(\boldsymbol{z}_p^+) - f(\boldsymbol{\mu}_z)][f(\boldsymbol{z}_p^-) - f(\boldsymbol{\mu}_z)]}{h_p^+ h_p^-} \Bigg\} \end{aligned} \tag{3.24}$$

where n is the number of the uncertain variables or parameters. The sampling points $\boldsymbol{z}_p^+$ and $\boldsymbol{z}_p^-$ are found using the following equation:

$$\boldsymbol{z}_p^{\pm} = \boldsymbol{\mu}_z + h_p^{\pm} \sigma_{z_p} \boldsymbol{e}_p \tag{3.25}$$

where $\boldsymbol{e}_p$ is the pth vector of the identity matrix of size n, and $h_p^{\pm}$ are given by:

$$h_p^{\pm} = \frac{\gamma_{z_p}}{2} \pm \sqrt{\Gamma_{z_p} - \frac{3\gamma_{z_p}^2}{4}} \tag{3.26}$$

The weights appearing in Eqs. 3.23 and 3.24 are determined as follows:

$$\begin{aligned} W_0 = 1 + \sum_{p=1}^{n} \frac{1}{h_p^+ h_p^-}; \quad W_p = \frac{1}{h_p^+ - h_p^-} \\ W_p^+ = \frac{(h_p^+)^2 - h_p^+ h_p^- - 1}{(h_p^+ - h_p^-)^2}; \quad W_p^- = \frac{(h_p^-)^2 - h_p^+ h_p^- - 1}{(h_p^+ - h_p^-)^2} \\ W_p^{\pm} = \frac{2}{(h_p^+ - h_p^-)^2} \end{aligned} \tag{3.27}$$

This method requires $2n+1$ function evaluations. Hence, the computational cost is comparable to the first-order Taylor-based method of moments, however, as demonstrated in [32], the accuracy of URQ is higher.

3.5 Optimization algorithms

The choice of the optimizer depends mainly on the problem characteristics and the type of solution sought. For problems involving smooth objectives and constraints (i.e., twice continuously differentiable with respect to the design variables), a gradient-based solver [110] might be the best suited solution, as they converge to local minima quickly. If a global solution is desired, multi-start gradient-based solvers [111] should be instead used because they are able to provide multiple local solutions. Gradient-based solvers, however, may be ineffective when the problem is not smooth, as they use derivatives to determine the search direction. In this circumstance, derivative-free methods, such as evolution-based algorithms [112] or pattern search solvers [113], may be a better choice. This section will introduce derivative-based algorithms, as well as genetic and pattern search algorithms. In the robust design optimization framework developed in this work evolution-based and pattern search solvers (reviewed below) are included.

3.5.1 Derivative-based algorithms

In mathematical optimization, derivative-based or gradient methods are algorithms used to solve optimization problems by means of gradients. More specifically, these methods define

the search direction by means of derivatives of the objective function with respect to the design variables. For these reason the smoothness of the objective function is a mandatory prerogative when using these methods. One of the simplest gradient methods is the gradient descent method. This method is a first-order optimization algorithm, used to find a local minimum of a function using gradient descent. This method starts with an initial guess of the solution, and then the gradient of the function at that point is taken. The solution is iteratively approached using the negative direction of the gradients. The descent method converges eventually where the gradient is zero, which corresponds to the local minimum. This method is first-order because it considers only the first derivative of the function. Let's assume we want to find the minimum of a given objective function $f(x)$. Using the gradient descent method we give some initial value x_0 for x. We then take the gradient (or derivative) of f with respect to x, denoted by ∇f. The derivative, calculated at x_0, gives the slope of the curve at that point, and its direction points to an increase in the function. Therefore, in order to approach the minimum value of f, we calculate the value of x for the next step moving towards the opposite direction of the gradient. Hence:

$$x_{k+1} = x_k - \lambda \nabla f(x_k) \tag{3.28}$$

where x_k and x_{k+1} represent the value of x at the iteration steps k and $k+1$, respectively. $\nabla f(x_k)$ is the derivative of f with respect to x, calculated at point x_k. λ is a number, greater than zero and normally lower than one, that forces the algorithm to make small jumps, keeping the algorithm numerically stable. For more details about the numerical stability of the gradient descent method, one is referred to [114].

In order to better understand the gradient descent method, an example is hereby provided. Assuming to have the following equation:

$$f(x) = x^2 \tag{3.29}$$

and to provide an initial guess of the solution $x_0 = 1$. The derivative of f with respect to x, ∇f, is:

$$\nabla f = \frac{f(x)}{dx} = \frac{dx^2}{dx} = 2x \tag{3.30}$$

The value of ∇f calculated at the point $x = x_0$ is then:

$$\nabla f(x_0) = 2 \cdot x_0 = 2 \cdot 1 = 2 \tag{3.31}$$

Assuming $\lambda = 0.1$, the point for the next iteration step is then computed as follows:

$$x_1 = x_0 - \lambda \nabla f(x_0) = 1 - 0.1 \cdot 2 = 0.8 \tag{3.32}$$

In order to calculate the following points x_2, x_3, ..., Eq. 3.31 and Eq. 3.32 are used recursively. The iterative process continues until the local minimum is achieved (i.e., when the gradient calculated at the current iteration point becomes zero).

3.5.2 Genetic algorithms

GAs are used for solving both constrained and unconstrained, single- or multi-objective optimization problems. They are primarily based on natural selection, which is the process on which the biological evolution is based. A GA, in fact, continuously modifies a population made up of individual solutions. At each iteration step, the algorithm selects individuals making up the current population to be parents, and combine them in order to produce the children for the next generations. The population therefore evolves towards an optimal solution over successive generations. GAs can be used to solve a wide range of problems, including those in which the objective function is discontinuous, non-differentiable, stochastic, or highly nonlinear. In order to find next generations, the main mechanisms on which the GA is based include:

- The selection mechanism. This mechanism selects the best individuals form the current population to be parents, contributing to the definition of the population of the next generation.
- The crossover mechanism. This mechanism combines two parents to form the children for the next generation.
- The mutation mechanism. This mechanism applies random changes to individual parent to form children.

As explained in [115], the GA starts by creating a random initial population. A population is made up of a number of individuals. Practically, an individual represents a given combination of the design variables, also called genome. For each of these individuals the fitness (or objective) function is calculated. The GA then performs a series of modifications of the individuals' genomes in order to produce a new population. Each successive population is called a new generation. In order to create a new generation, the GA performs the following steps:

- Calculate the objective function of each individual of the current generation;

- Score these individuals according to their objective function values.
- Select some members of the current generation, called parents. This selection is based on the individuals' objective function values.
- Some of the best members, called elite, that have the lowest value of the objective function, are selected. Elite members are passed without modification to the next generation.
- Produce children from the parents. Children are produced either by making random changes to a single parent (i.e., mutation), or by combining the genomes of a pair of parents (i.e., crossover).
- Replaces the current population with the children to form the next generation.

The iterative process normally proceeds until the GA is not able to improve the objection function for a given user-defined number of consecutive generations.

GAs have been extensively used to solve optimization problems with inequality constraints, such as that given by Eq. 3.1. The penalty function approach has been often used in conjunction with GAs due to its simplicity. Penalty functions consist of penalty parameters added to the objective function, giving a measure of violation of the constraints. The measure of violation is nonzero when the constraints are violated and is zero in the region where constraints are not violated. In particular, the larger the constraint violation, the higher the penalty parameter. In this way, the optimizer is able to determine the search direction that could lead the solution to regions where the constraints are not violated. The use of penalty functions, however, has several functional and operational drawbacks. For example, penalty functions do not take into account the mathematical form of the constraints. Moreover, the addition of penalty terms to the objective functions can create distortions (such as discontinuities) in the objective functions. Therefore, more sophisticated methods have been devised to treat inequality constraints in the context of GAs. One of these methods is the augmented Lagrangian genetic algorithm [116], belonging to the family of augmented Lagrangian algorithms [117]. These algorithms attempt to solve optimization problems with inequality constraints by formulating minimization subproblems. In such subproblems, a function depending on the objective function, the constraint functions and penalty parameters is minimized, using the genetic algorithm, such that all the constraints are verified. Practically, a minimization subproblem is carried out for each individual that does not satisfy one or more inequality constraints. This subproblem aims to satisfy all constraints by varying the values of the design variables of the solution under consideration. The subproblems stop when all constraints are verified. When using the augmented Lagrangian genetic algorithm,

the number of function evaluations per generation is therefore much higher (and normally unknown) than that required when treating inequality constraints through penalty functions.

3.5.3 Pattern search algorithms

Pattern search algorithms belongs to the family of direct search algorithms. Like GAs, these methods do not require information regarding the gradient of the objective function and constraints, and therefore they can be used to optimize problems the objective function and constraints of which are not differentiable or non-continuous. Pattern search algorithms approach an optimal solution computing a sequence of points. At each iteration step, the algorithm generates a set of points, called the mesh, around the current point, which is the result of the previous iteration step. The mesh is determined by adding the current point to a scalar multiple of a set of vectors called a pattern. If a point in the mesh improves the objective function of the current point, then that point becomes the current point at the next iteration step. The mechanism of generating the mesh is named polling. After a polling, the algorithm changes the value of the mesh size. In case of a successful polling the mesh size contracts, while if the polling has not found a better point the mesh size expands. Like GAs, pattern search algorithm can handle inequality constraints by means of augmented Lagrangian algorithms, such as the augmented Lagrangian pattern search [118]. This algorithm solves optimization problems with inequality constraints by formulating minimization subproblems such that all the constraints are verified.

In order to show how this algorithm works, a simple example (adapted from that in [115]) is given. Let's assume we want to optimize a given system by minimizing an objective function, f, depending on the design variables $\boldsymbol{x} = \{x_a, x_b\}$. Considering an unconstrained problem, this optimization can be formulated as follows:

$$\begin{aligned} \text{Find: } & \boldsymbol{x} = \{x_a, x_b\} \\ \text{to minimize: } & f(\boldsymbol{x}) \end{aligned} \tag{3.33}$$

Pattern search finds a sequence of points $\boldsymbol{x_0}$, $\boldsymbol{x_1}$, $\boldsymbol{x_2}$, ..., that approach an optimal solution. The value of the objective function either decreases (i.e., improves) or remains the same from each point in the sequence to the next. The pattern search begins at the initial point $\boldsymbol{x_0}$ provided. In this example, x_a is equal to 2.1 and x_b is equal to 1.7. Therefore the initial point can be expressed as $\boldsymbol{x_0} = \{2.1, 1.7\}$. At this point, the value of the objective function is equal to 4.6381. At the first iteration, the mesh size is 1 and the algorithm adds the pattern vectors

to the initial point $\boldsymbol{x_0}$ to compute the following four mesh points:

$$\begin{aligned} [1 \quad 0] + \boldsymbol{x_0} &= [3.1 \quad 1.7] \\ [0 \quad 1] + \boldsymbol{x_0} &= [2.1 \quad 2.7] \\ [-1 \quad 0] + \boldsymbol{x_0} &= [1.1 \quad 1.7] \\ [0 \quad -1] + \boldsymbol{x_0} &= [2.1 \quad 0.7] \end{aligned} \tag{3.34}$$

The algorithm then computes the objective function at these mesh points, as show in Fig. 3.1. After the first polling, point $[1.1 \quad 1.7]$ (depicted in Fig. 3.1) improves the value of the

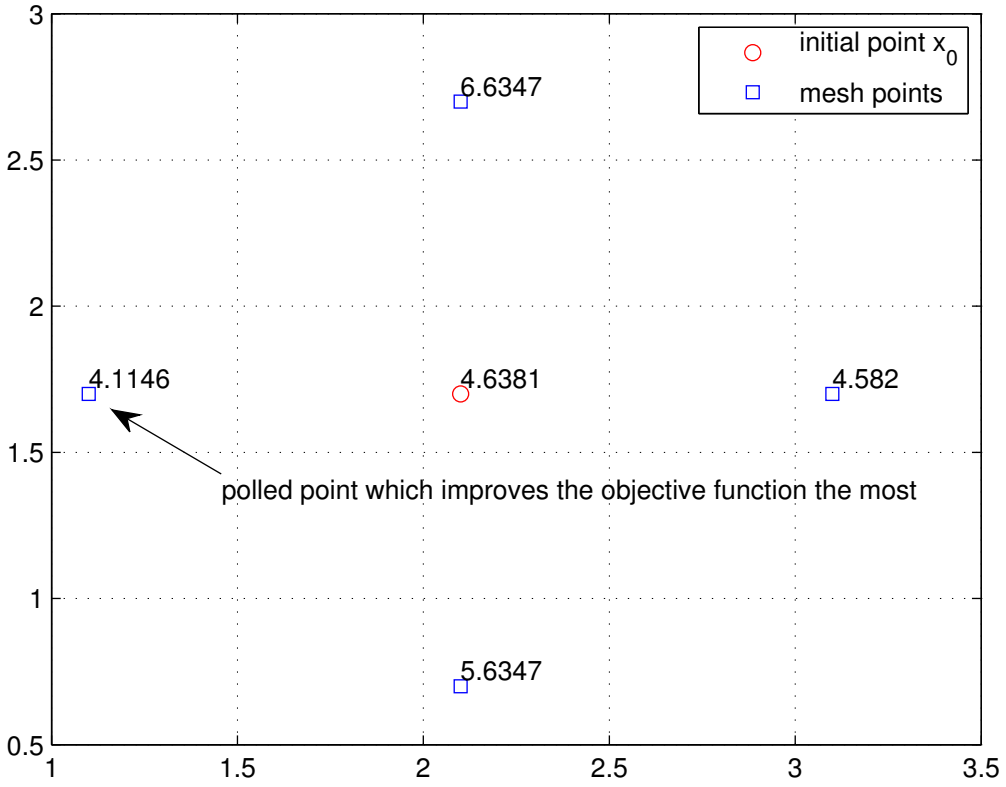

Fig. 3.1 Objective function values at initial point and mesh points after the first polling.

objective function the most (with respect to that of $\boldsymbol{x_0}$), achieving a value of 4.1146. In this case, the first polling is successful. The pattern search algorithm then sets the current point for the following iteration equal to $\boldsymbol{x_1} = \{1.1, 1.7\}$. After a successful poll, the current mesh size is multiplied by a factor of 2 (i.e., the mesh size is doubled). Therefore, because the initial mesh size was 1, at the second iteration the mesh size is 2. Thus, the mesh for the

second pooling will be:

$$\begin{aligned} 2\cdot[1 \quad 0]+\boldsymbol{x_1} &= [3.1 \quad 1.7] \\ 2\cdot[0 \quad 1]+\boldsymbol{x_1} &= [1.1 \quad 3.7] \\ 2\cdot[-1 \quad 0]+\boldsymbol{x_1} &= [-0.9 \quad 1.7] \\ 2\cdot[0 \quad -1]+\boldsymbol{x_1} &= [1.1 \quad -0.3] \end{aligned} \tag{3.35}$$

As seen before, the algorithm then calculates the values of the objective function at each of the points making up the current mesh. The mesh point that improves the objective function the most will become the current point, and the mesh size will be doubled. In case that none of the mesh points can improve the objective function, the poll is unsuccessful. In this case, the algorithm does not change the current point at the next iteration, and the algorithm multiplies the current mesh size by 0.5 (i.e., the mesh size is halved). The iterative process continues until the mesh size becomes smaller than a given user-defined tolerance.

Chapter 4

Multidisciplinary and robust design optimization framework

The research reported in this thesis focuses on the development of a computational framework which combines the multidisciplinary and the robust design optimization of HAWT rotors. The adopted design optimization approach uses a FIO architecture, based on an integrated aeroservoelastic analysis model that analyzes the aerodynamic and structural characteristics of the rotor, directly incorporating the control strategy, and assesses the economical performance of the rotor by means of a cost model. The analysis model is coupled with the optimizer through the uncertainty propagation algorithm, needed to propagate the input uncertainties throughout the design system, characterizing the objective function and constraints probabilistically. The rest of this chapter deals with the description of the developed design framework, highlighting the main features of its various parts. The presented design system has been used to perform the optimization of a multi-megawatt HAWT subject to geometric and environmental uncertainties. The environmental uncertainties considered in this work refer exclusively to the mean value of the wind speed frequency distribution. The results of the environmental uncertainty application will be reported in Chapter 6, while the results of the geometric uncertainty application have been published in [19].

4.1 Fully integrated multidisciplinary and robust design optimization framework

An overview of the developed fully integrated multidisciplinary and robust design optimization framework is schematically shown in Fig. 4.1. As depicted in this figure, the design variables, $\boldsymbol{b}$, generated by the optimizer, are directly passed on to the uncertainty propagation

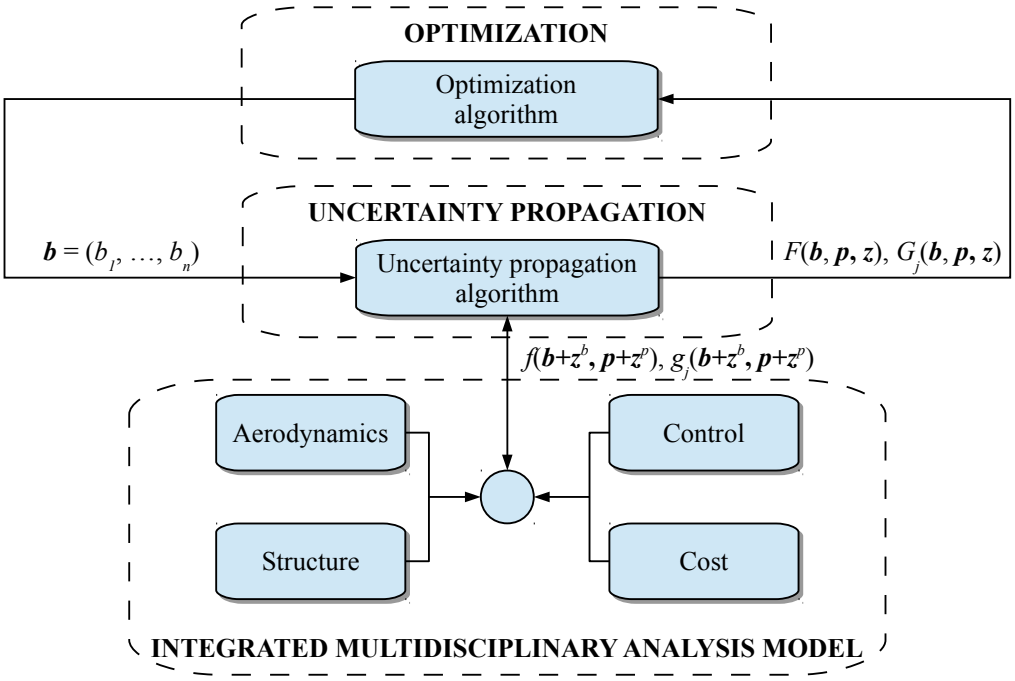

Fig. 4.1 Overview of the fully integrated multidisciplinary and robust design optimization framework. $\boldsymbol{b}$ represents the vector of the design variables, $b_i,\ i = 1,n$, $\boldsymbol{p}$ is the vector of the design parameters, $p_i,\ i = 1,m$, while $\boldsymbol{z}^b$ and $\boldsymbol{z}^p$ are the vector of the uncertainties associated with the design variables and parameters, respectively. $F(\boldsymbol{b},\boldsymbol{p},\boldsymbol{z})$ and $G_j(\boldsymbol{b},\boldsymbol{p},\boldsymbol{z})$ are the probabilistic definition of the objective function and constraints, respectively. $f(\boldsymbol{b}+\boldsymbol{z}^b,\boldsymbol{p}+\boldsymbol{z}^p)$ and $g_j(\boldsymbol{b}+\boldsymbol{z}^b,\boldsymbol{p}+\boldsymbol{z}^p)$ represent the stochastic objective function and constraints, respectively.

module. This module then evaluates the probabilistic form of the objective function, F, and constraints, G_j. F and G_j depend on the design variables, the design parameters, $\boldsymbol{p}$, and the uncertainties associated with the design variables and parameters, denoted by $\boldsymbol{z}^b$ and $\boldsymbol{z}^p$, respectively. As discussed in Chapter 3, F and G_j are generally defined in terms of the statistical moments of the stochastic objective function and constraints, respectively denoted by f and g_j. Practically, the probabilistic definition of the objective function and constraints is determined by the uncertainty propagation algorithm by means of a given number of deterministic analyses of the system. In each of these analyses, f and g_j are determined by means of the integrated multidisciplinary analysis model described in Sect. **??**. Once the probabilistic objective function and constraints are determined, they are sent back and assessed by the optimizer. The iterative process continues until convergence is reached.

4.2 Integrated multidisciplinary analysis model

The optimization problems reported in Chapter 6 were formulated considering the LCOE as performance metric. Such optimizations included constraints on blade deformations, normal and buckling stresses, fatigue damage and blade natural frequencies. A detailed description of the adopted objective function and constraints will be given in Chapter 6.

The assessment of the aeroservoelastic behavior of HAWT rotors, and thus the evaluation of the design objective function and constraints required the integration of several simulation tools, shown schematically in Fig. 4.2. These computational tools were linked together

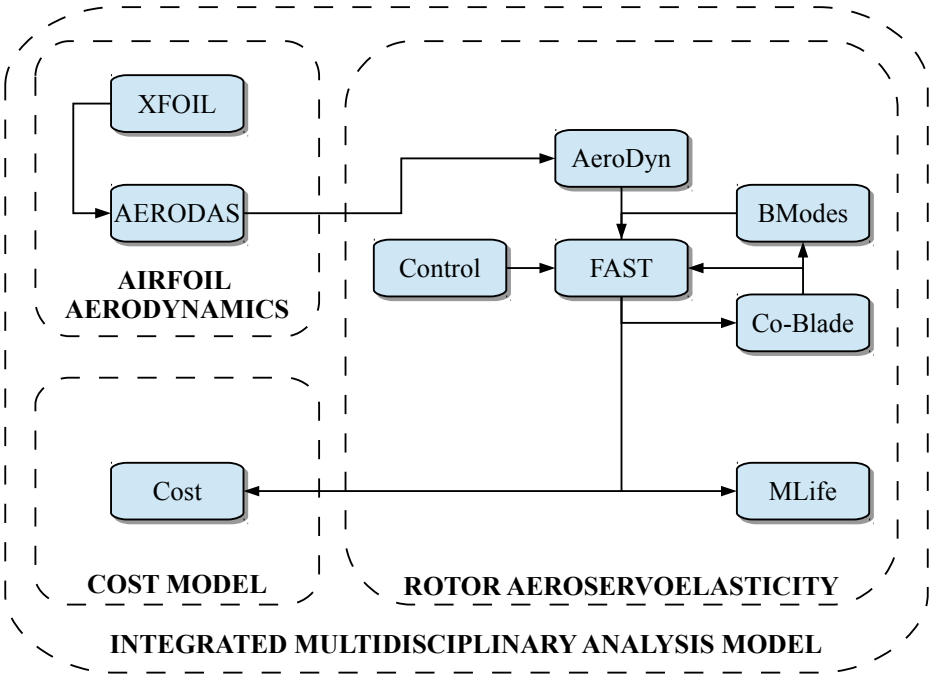

Fig. 4.2 Overview of the integrated multidisciplinary analysis model, showing the computational tools used and their mutual interactions.

in a MATLAB environment, which managed the data flow between all the codes. The multidisciplinary analysis framework for the integrated rotor design combines three main modules, encompassing: a) a module for the aerodynamic analysis of the blade airfoils, b) a module for the aeroservoelastic analysis of the rotor, and c) a cost model for the assessment of the economical performance of the rotor. All modules of the multidisciplinary analysis system are presented below, describing in details the inputs and outputs of the integrated computational tools.

4.2.1 Airfoil aerodynamics

In this study, the aeroelastic analysis of the rotor was based on the BEM theory, which requires the airfoil aerodynamic coefficients. As seen in Chapter 2, 2D aerodynamic characteristics of airfoils can be determined using panel codes, such as XFOIL and RFOIL, or by means of CFD. Run-times of CFD, even in 2D simulations, are still excessive for their use in design optimizations, and RFOIL is not an open-source tool and could thus not be used in this study. Therefore, in this research work, 2D airfoil lift and drag coefficients were calculated using the airfoil analysis code XFOIL. In this code, transition from laminar to turbulent flow along the airfoil is simulated by the e^N method, through the parameter NCRIT. A suitable value of this parameter depends on the environmental disturbance[1] level in which the airfoil operates, and mimics the effect of such disturbances on laminar-to-turbulent transition. For all optimizations carried out in this research work, NCRIT was fixed to the standard value of 9, corresponding to average wind tunnel conditions. The 2D aerodynamic data thus calculated were then corrected to account for the complex 3D physics occurring over rotating blades, in both pre- and post-stall regions, by means of AERODAS.

As shown in Fig. 4.3, XFOIL was used to compute 2D airfoil lift and drag coefficients for a Re ranging from $2 \cdot 10^6$ to $14 \cdot 10^6$, over values of the AoA ranging from -6 to 26 deg. 2D lift and drag coefficients were then fed into AERODAS, evaluating the extended 3D lift and drag coefficients. AERODAS polars for AoA ranging from -180 to 180 deg were derived from a small number of parameters of the XFOIL polars. These parameters were the zero-lift AoA, the maximum lift and drag coefficients, the AoA at maximum lift and drag, the slope of the linear part of the lift curve, and the minimum drag coefficient.

In order to provide a practical example, Fig. 4.4 shows the comparison between the experimental polars of the 21-percent-thick S809 airfoil [119], and those determined by means of XFOIL and AERODAS for the same airfoil, for a Reynolds number of $1 \cdot 10^6$. It is noted that the XFOIL polars match the experimental ones up to 9 deg. At AoAs above 9 deg, XFOIL over-predicts the lift coefficient, while it under-predicts the drag coefficient. Figure 4.4 also shows that the AERODAS correction takes into account an indicative blade aspect ratio of 15.3 by lowering the lift curve with respect to that obtained for an infinite blade aspect ratio.

[1] In this context, environmental disturbance is referred to both acoustic (sound) and vortical (turbulence) disturbances.

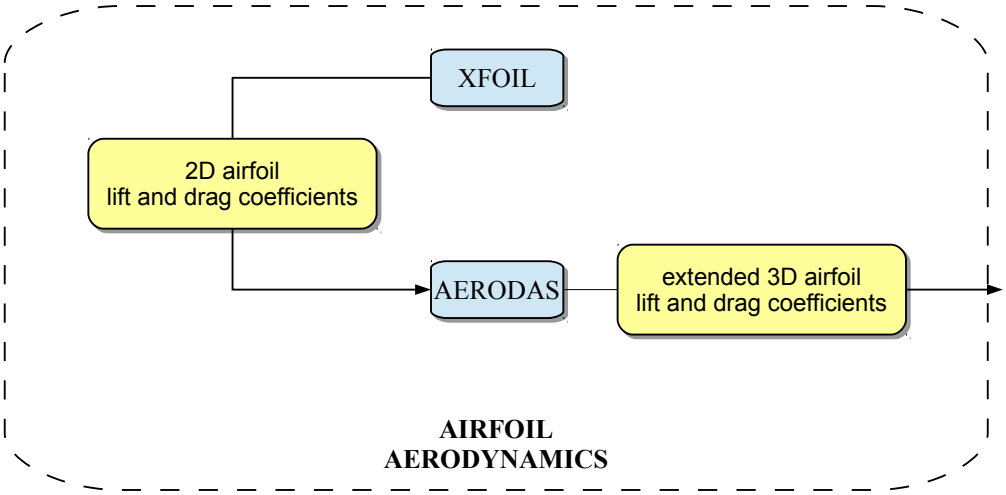

Fig. 4.3 Details of the module for the aerodynamic analysis of the blade airfoils. Blue boxes indicate the computational codes integrated in this module, while yellow boxes represent their inputs/outputs.

4.2.2 Rotor aeroservoelasticity

The aeroservoelastic simulations of the turbine rotor were performed by means of FAST, which was linked to an external library defining the control system. A detailed description of the control strategy implemented in the aeroservoelastic model for this work is reported in Chapter 5. For a given rotor geometry and wind conditions, FAST was used to predict the rotor speed and power, as well as blade mass and ultimate and fatigue loads. FAST inputs include distributed blade properties, such as the blade section mass per unit length and blade section stiffness [40]. The blade mass per unit length is then integrated along the blade length in order to determine the total blade mass. As shown in Fig. 4.5, using the aerodynamic characteristics of the airfoils determined by XFOIL and AERODAS, the rotor aerodynamics was analyzed with AeroDyn, a library implementing the BEM theory and several corrections, including the Prandtl's correction to account for tip and hub losses, and the correction accounting for axial induction factors exceeding the maximum theoretical limit of 0.5. In the analyses reported in this thesis, however, Prandtl's correction was disabled because the 2D airfoil data were already corrected to account for finite aspect ratio effects in AERODAS. FAST employs a linear modal representation to characterize blade flexibility. Blade modes depend on the rotor speed, blade geometry and span-variant structural properties, such as mass, moments of inertia, and stiffnesses. Such blade span-variant structural properties

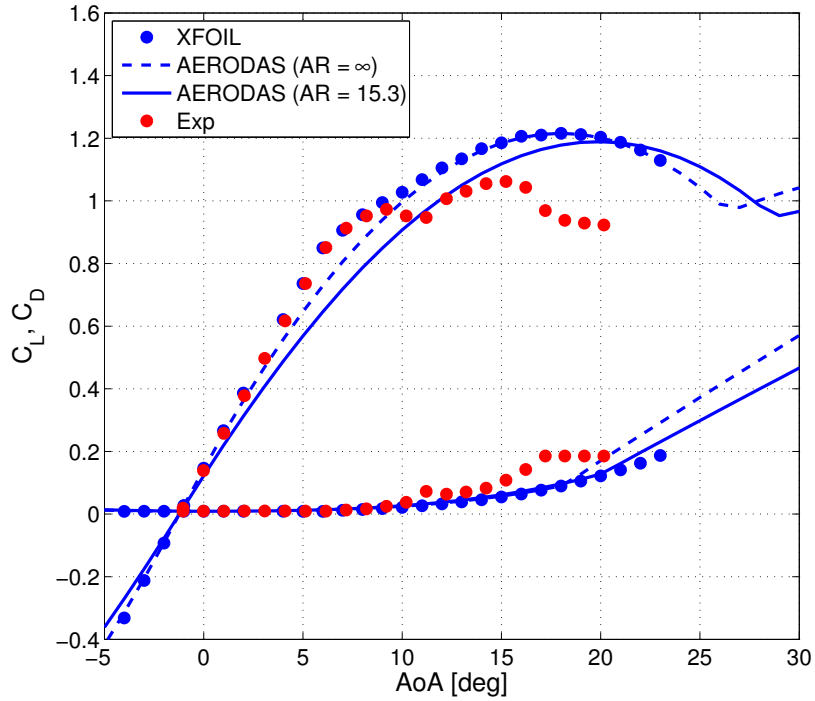

Fig. 4.4 Comparison between the S809 aifoil experimental polars and those determined by means of XFOIL and AERODAS, for a Reynolds number of $1 \cdot 10^6$. The AERODAS correction was implemented by using an infinite blade aspect ratio and an indicative aspect ratio equal to 15.3.

were computed by means of the structural analysis code Co-Blade, and subsequently fed into the preprocessor BModes in order to determine the blade modes. BModes was also used to determine the blade natural frequencies. The structural properties and blade modes determined by means of Co-Blade and BModes were then used by FAST to perform the aeroservoelastic calculations, determining the blade ultimate and fatigue loading, as well as the rotor power curve and blade mass. During such aeroelastic calculations, FAST was coupled with a control routine, defining the rotor control strategy. The obtained ultimate blade loads were then assessed by means of Co-Blade, which was used to compute blade deformations and material normal and buckling stresses. The fatigue loads were instead post-processed by MLife, providing the resulting total fatigue damage.

4.2.3 Cost model

LCOE is the figure of merit used to assess the economical performance of each design, and the LCOE model adopted herein is based on the DOE/NREL scaling model. According to

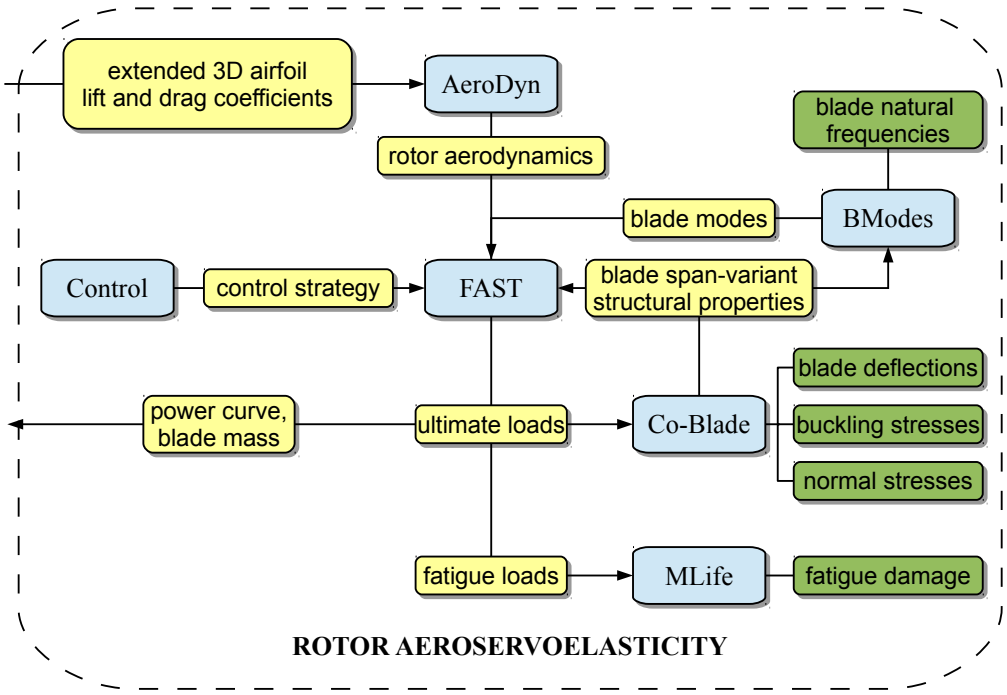

Fig. 4.5 Details of the module for the aeroservoelastic analysis of the rotor. Blue boxes indicate the computational codes integrated in this module, while yellow boxes represent their inputs/outputs. Green boxes instead represent the constraints.

this model, the LCOE of an offshore HAWT is given by Eq. 2.35. Although only the rotor design is considered in the optimization study of this thesis, the LCOE of each design refers to the cost of the whole turbine, including drive train, nacelle, tower and foundations. This is accomplished by including in ICC the cost of all turbine components, which results in this variable being the sum of a term proportional to the blade mass varying with the particular rotor configuration, and other terms referring to the costs of all other components [102]. In the LCOE equation, also AEP varies for each rotor being analyzed. AEP is defined as the amount of electricity that a wind turbine can generate in a year at a given site. Therefore, the AEP of a wind turbine depends on its power curve, as well as on the annual wind characteristics of the site in which it has been installed. At a specific site, wind speed variations during one year are described in terms of a PDF, that define the so-called wind speed distribution. Figure 4.6 shows the power curve of a typical multi-megawatt HAWT, and the indicative wind speed distribution of a generic site. The power curve defines the electrical power P_e that a turbine can generate at a given wind speed u, while the wind speed PDF, p_u, describes the probability for the wind speed to take on a given value during one year.

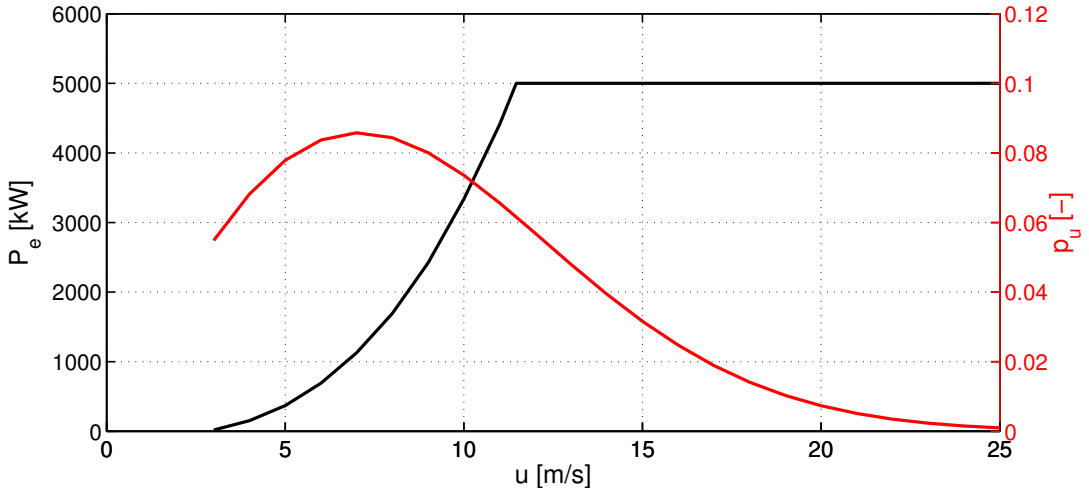

Fig. 4.6 Typical multi-megawatt HAWT power curve (in black) and indicative wind speed distribution of a generic site (in red).

The power curves of all the HAWT configurations analyzed in this work were evaluated by means of FAST. More specifically, the power curve, $P_e(u)$, of a given HAWT was reconstructed by running FAST under increasing discrete hub height wind speeds, from cut-in to cut-out. These wind conditions were represented by AeroDyn hub height wind files, defining steady wind speeds, perpendicular to the rotor plane, and characterized by a 1/7 power law profile. The power law shear profile is used to determine the wind speed, u_Z, at any height, Z, based on a reference height, Z_r, and the wind speed at the reference height, u_r, using the following equation:

$$u_Z = u_r \left(\frac{Z}{Z_r} \right)^{\alpha_p} \tag{4.1}$$

where the exponent α_p is an empirical coefficient that dependents on a large number of variables including atmospheric stability, temperature, terrain surface roughness, changes in the terrain surface conditions and terrain shape. A review of methods for determining representative power law exponents can be found in [42]. In this work, neutral stability conditions were considered, corresponding to a value of α_p equal to 1/7 (representing indeed a 1/7 power law profile).

The wind speed distribution of a given site can be well characterized by the Weibull distribution. The Weibull distribution is characterized by two parameters: the shape parameter k_W (dimensionless) and the scale parameter c_W (expressed in m/s). The PDF of the Weibull

distribution is given by:

$$p_u = \frac{k_W}{c_W}\left(\frac{u}{c_W}\right)^{k_W-1}\exp\left[-\left(\frac{u}{c_W}\right)^{k_W}\right] \tag{4.2}$$

The average wind speed of the Weibull distribution can be expressed as:

$$\bar{u} = c_W\Gamma\left(1+\frac{1}{k_W}\right) \tag{4.3}$$

where Γ is the gamma function given by:

$$\Gamma(n) = \int_0^\infty e^{-x}x^{n-1}dx \tag{4.4}$$

In this research, k_W was always set equal to 2, corresponding to the Rayleigh distribution.

As given by Eq. 4.5, from cut-in wind speed $u_{\text{cut-in}}$ to cut-out wind speed $u_{\text{cut-out}}$, AEP can be calculated by integrating the turbine power curve, $P_e(u)$, against the wind speed distribution PDF, p_u. The value of AEP is one of the inputs required by the cost model represented by Eq. 2.35.

$$\text{AEP} = 8670\cdot\int_{u_{\text{cut-in}}}^{u_{\text{cut-out}}} P_e(u)p_u du \tag{4.5}$$

where 8670 is the number of hours in one year.

As depicted in Fig. 4.7, in the presented design framework, the power curve and the blade mass, evaluated by means of FAST, were used as input values for the cost model, eventually evaluating the LCOE.

The costs of the turbine components indicated in the DOE/NREL scaling model are based on 2002 dollars. Therefore, these costs need to be updated to account for the year-over year change in products, material and labor costs. Cost escalation was based on the producer price index (PPI). The PPI, maintained and updated on a monthly basis by the U.S. Department of Labor, Bureau of Labor Statistics, tracks the price change of a wide range of product (or commodity) categories. Commodity escalation factors were determined by using the PPI categories provided by the DOE/NREL scaling model for each turbine component.

4.3 Uncertainty propagation

In the probabilistic design framework presented herein, the uncertainty propagation algorithm was implemented in a MATLAB computational interface, connecting the optimizer to the

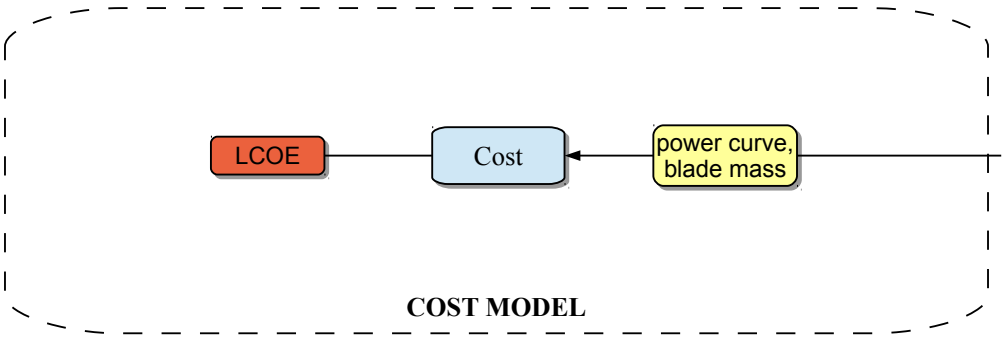

Fig. 4.7 Details of the cost model.

analysis model described in Sect. 4.2. The optimization strategies integrated in the presented design system will be described in Sect. 4.4. This section focuses on the techniques used to perform uncertainty propagation. During the optimization process, at each iteration, the optimizer generates a vector of design variables, defining a given HAWT configuration to be assessed probabilistically. Subsequently, the uncertainty propagation algorithm, using the design variables and the input uncertainties, determines the probabilistic form of the objective function and constraints. In this work, the objective function and constraints are defined probabilistically by calculating their mean and standard deviation. Within a robust design optimization framework, uncertainty propagation is a computationally onerous step, usually involving a high number of analyses of HAWT configurations. Therefore, the choice of the uncertainty propagation algorithm is a critical task, involving a trade-off between accuracy and computation time.

In the robust design optimization reported in [19], the uncertainty affecting 10 geometric parameters of HAWT blades were considered, encompassing blade thickness, chord and twist distributions. In this work, uncertainty propagation was efficiently achieved by using the URQ approach. According to this method, for each HAWT configuration, 21 rotor analyses were necessary to determine the mean and the standard deviation of the objective function and constraints. In this particular application, nonlinearities in the system response were not

too important, and therefore, under these circumstances, the accuracy of the URQ approach was not affected.

In the design optimization under environmental uncertainty reported in Chapter 6, a single uncertain variable was taken into account in the robust optimization process of a multi-megawatt HAWT, namely the mean value of the wind speed distribution, denoted by the symbol $\bar{u}$. In this optimization problem, the mean and the standard deviation of LCOE, denoted respectively by μ_{LCOE} and σ_{LCOE}, were minimized concurrently. The stochastic variable $\bar{u}$ was considered uniformly distributed within a given range of variability from $\bar{u}_L$ to $\bar{u}_U$. Figure 4.8 shows the uniform distribution of $\bar{u}$, denoted by $p_{\bar{u}}$, spanning the range of $\bar{u}$ from $\bar{u}_L$ to $\bar{u}_U$. The probability of the random variable falling within a particular range of

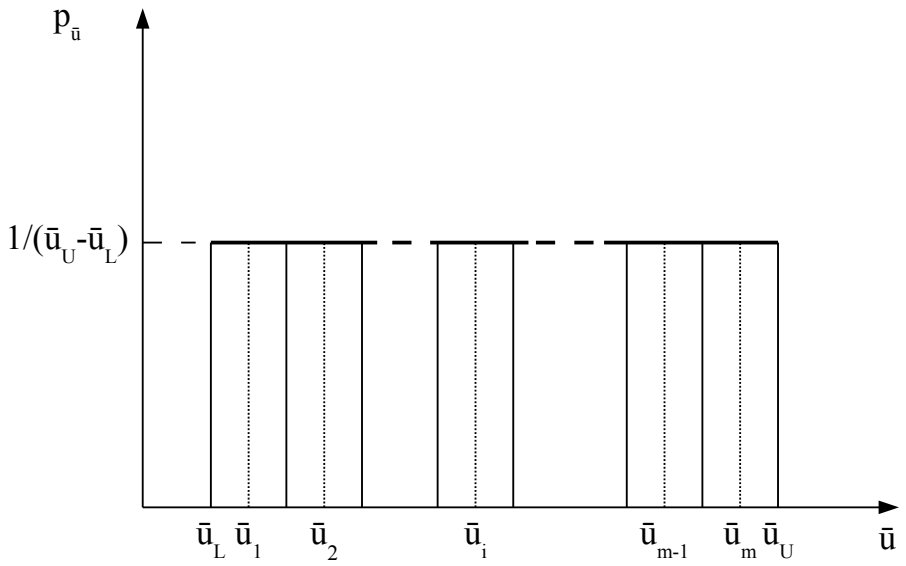

Fig. 4.8 Uniform PDF of the uncertain variable, $\bar{u}$, denoted by $p_{\bar{u}}$, defined within the lower bound, $\bar{u}_L$, and the upper bound, $\bar{u}_U$. The range of variability of $\bar{u}$ was divided in m intervals with equal probability for subsequent Latin hypercube sampling.

values is given by the integral of this variable's PDF over that range, that is, it is given by the area under the PDF but above the x-axis and between the lowest and greatest values of the range. The area under the PDF of $\bar{u}$ between $\bar{u}_L$ to $\bar{u}_U$ is equal to 1 (all values of $\bar{u}$ falls within $\bar{u}_L$ to $\bar{u}_U$). In this robust optimization problem, the uncertainty propagation was accomplished by using the Latin hypercube sampling. As shown in Fig. 4.8, the range of variability of the input stochastic variable was divided in m intervals with equal probability. Therefore, each

of these intervals is characterized by the same height and thickness. Subsequently, the metric LCOE was sampled for $\bar{u}_i,\ i = 1,m$, where $\bar{u}_i$ is the center value of the i-th interval. Once LCOE was calculated for all m sampling points, its mean and the standard deviation were computed as follows:

$$\mu_{\mathrm{LCOE}} = \frac{1}{m}\sum_{i=1}^{m} \mathrm{LCOE}(\bar{u}_i) \tag{4.6}$$

$$\sigma_{\mathrm{LCOE}} = \sqrt{\sigma^2_{\mathrm{LCOE}}} = \sqrt{\frac{1}{m-1}\sum_{i=1}^{m} [\mathrm{LCOE}(\bar{u}_i) - \mu_{\mathrm{LCOE}}]^2} \tag{4.7}$$

4.4 Optimization

The optimizations carried out in this work aimed to find a global minimum over a large design space. As explained in Chapter 6, some of the solutions included in this space are considered geometrically infeasible or prevent some of the analysis codes from converging (e.g., XFOIL fails to converge for some airfoil shapes at given flow conditions). In this work, these solutions are treated with penalty functions. The aerostructural constraints of the optimization problems, also described in Chapter 6, are treated in the same way. As seen in Chapter 3, the use of penalty functions introduces discontinuities in the objective function, and thus affect its smoothness. For this reason, as explained in Chapter 3, gradient-based algorithms could not be used in this study, as they use derivatives to determine the search direction. Therefore, in the framework of this research, gradient-free codes have been used, namely the multi-objective parzen-based estimation of distribution (MOPED) [120] and the inflationary differential evolution algorithm (IDEA) [121], two GAs, and the MATLAB patternsearch function [115], based on a pattern search algorithm. MOPED and IDEA codes were used to perform the probabilistic optimization under geometric uncertainty reported in [19], while the MATLAB patternsearch function was used to carry out the probabilistic optimization under environmental uncertainty described later on in this thesis, in Chapter 6.

4.4.1 MOPED and IDEA

As mentioned in Chapter 3, evolutionary algorithms solve optimization problems by making a generation of individuals evolve subject to selection and search operators. In this study, an individual denotes a given HAWT configuration. This iterative process eventually leads to a population containing the fittest possible individuals (best HAWT configuration designs), or individuals who are significantly fitter than those of the starting population. The role of the selection operators is to identify the fittest or most promising individuals of the current

population, whereas search operators such as crossover and mutation attempt to generate better offspring starting from suitably selected individuals of the current generation. Each individual is defined by genes, which correspond to design variables in design optimization. The solution of the optimization problems reported in [19] is based on a two-stage approach using MOPED and IDEA.

MOPED belongs to a subset of evolutionary algorithms and was developed to circumvent certain algorithmic problems of conventional evolutionary algorithms, which can be ineffective when the problem at hand features a high level of interaction among the design variables. This is mainly due to the fact that the recombination operators are likely to disrupt promising sub-structures that may lead to optimal solutions. Additionally, the use of the crossover and mutation operators may result in slow convergence to the solution of the optimization; that is, it may require a large number of generations to obtain very fit individuals. MOPED was developed to circumvent shortfalls of this kind. Its use of statistical tools enables it to preserve promising sub-structures associated with variable interaction from one generation to another (automatic linkage learning). Such statistical tools also replace the crossover and mutation operators of conventional evolutionary algorithms, and they allow a faster convergence of MOPED with respect to the latter class of optimizers. Starting from the individuals of the current population, MOPED builds an approximate probabilistic model of the search space. The role of the crossover and mutation operators is replaced by sampling of this probabilistic model. There exist other similar evolutionary methods that use the aforementioned strategy, and they are called estimation of distribution algorithms (EDAs) [122]. MOPED is a multi-objective optimization EDA for continuous problems that uses the Parzen method [123] to build a probabilistic representation of Pareto solutions, and can handle multivariate dependencies of the variables [120, 124]. MOPED implements the general layout and the selection techniques of the non-dominated sorting genetic algorithm II (NSGA-II) [125], but traditional crossover and mutation search approaches of NSGA-II are replaced by sampling of the Parzen model. NSGA-II was chosen as the base for MOPED mainly due to its simplicity, and also for the excellent results obtained for many diverse optimization problems [126, 127].

The Parzen method utilizes a non-parametric approach to kernel density estimation, and results in an estimator that converges asymptotically to the true PDF over the whole design space. Additionally, when the true PDF is uniformly continuous, the Parzen estimator can also be made uniformly consistent. The Parzen method allocates N_{ind} identical kernels (where N_{ind} is the number of individuals of the current population), each centered on a different element of the sample. A probabilistic model of the promising search space portion is built on the basis of the statistical data provided by the N_{ind} individuals through their kernels, and

$\tau_E \, N_{ind}$ new individuals ($\tau_E \leq 1$) are sampled. The variance of each kernel depends on (*i*) the location of the individuals in the search space and (*ii*) the fitness value of these individuals, and its construction leads to values that favour sampling in the neighborhood of the most promising solutions.

The features of MOPED often prevent the true Pareto front from being achieved, particularly when the front is broad and the individuals of the population are spread over different areas, which are far apart from each other in the feasible space. This circumstance has prompted coupling MOPED with another evolutionary algorithm, which has better convergence properties. To this aim, IDEA was selected. IDEA was first developed for the design optimization of interplanetary trajectories, and it is an improved variant of the differential evolution (DE) algorithms [121]. The IDEA algorithm is based on a synergistic hybridization of a standard DE algorithm and the strategy behind the monotonic basin hopping (MBH) [128]. The resulting algorithm was shown to outperform both standard DE optimizers and the MBH algorithm in the solution of challenging space trajectory design problems, featuring a multiple funnel-like structure. In this paper, a modified version of IDEA was used to move the individuals of the approximate Pareto front obtained with MOPED closer to the true front.

The main features of the original IDEA algorithm are reported in [121]. The IDEA algorithm works as follows: a DE process is performed several times and each process is stopped when the population contracts below a predefined threshold. At the end of each DE step, a local search is performed in order to get closer to the local optimum. In the case of non-trivial functions, where there is a high likelihood of converging to local optima, the combined DE/local search is usually iterated several times, performing either a local or a global restart on the basis of a predefined scheduling.

In the current implementation, MOPED and IDEA are used sequentially. When MOPED has reached a given number of generations, its final population represents a first and good approximation to the sought Pareto front. Then, clustered sub-populations of such a population are used as initial solutions of the single-objective constraint IDEA optimizer. this algorithm "pushes" the individuals of a sub-population of the MOPED front towards a better local approximation of the sought Pareto front. The resulting two-stage optimizer blends the exploratory capabilities of MOPED (global exploration) and the favorable convergence characteristics of IDEA (exploitation of local information).

4.4.2 MATLAB patternsearch function

The MATLAB pattern search algorithm was used to carry out the optimizations reported in Chapter 6. This function was parallelized over 32 processors through the MATLAB

distributed computing server tool [115]. As seen in Chapter 3, a pattern search algorithm searches the global minimum of a function by using a set of points, called pattern, which expands or shrinks depending on whether any point within the pattern has a lower objective function value than the current point. As a starting point for the optimizations carried out in this study, a suitable reference turbine, described in Chapter 6, was used. For more details about the patternsearch function and the distributed computing server tool used, one can refer to the MATLAB documentation [115].

Chapter 5

Design space and reference turbine definition

The aim of an optimization process is normally to improve the performance of a given system by optimizing a specified set of parameters without violating some constraints. Therefore, a preliminary step in design optimization is to characterize the system under consideration in terms of numerical parameters, defining selected properties that drive the optimization. The set of these parameters, denoted by design variables, and the numerical bounds in which they can vary during the course of the optimization define the design space. In this work, the blade external geometry, the rotor speed and the blade internal structural layup of a multi-megawatt HAWT were optimized concurrently, and therefore these wind turbine elements needed to be parametrized. The aim of this chapter is twofold. Firstly, it presents the parametrization of the turbine's blade external geometry, rotor speed and internal structural layup needed for the subsequent optimization. Secondly, it defines a reference turbine by means of the developed parametrization. The reference turbine is based on the NREL offshore 5-MW baseline wind turbine [36]. The design specifications of this turbine are reported in [36]. As explained below, the definition of a reference turbine was required to determine an opportune starting point for the optimizer, and to provide a metric against which the effectiveness of the optimizations could be assessed.

5.1 Turbine parametrization

This section deals with the parametrization of the turbine's blade external geometry, rotor speed and internal structural layup.

5.1.1 External geometry parametrization

The 3D external geometry of each rotor blade considered in the optimization process was determined by the airfoil schedule, and the chord and twist distributions along its span. The airfoil schedule was defined by 2 circular sections, respectively at 0% and 6.67% blade length, and the geometry of 3 airfoils, namely that at 16.67% blade length (root airfoil), 50% blade length (midspan airfoil) and 100% blade length (tip airfoil). The geometry of the sections between the root and tip radii was obtained with linear interpolations. As reported below, the geometry of the interpolated sections was needed to determine the structural properties of the blade by means of Co-Blade. Root, midspan and tip airfoils were treated as part of the optimization, as well as blade chord and twist distributions. In order to reduce the computational burden associated with the optimization process, the rotor geometry ideally should be parametrized by means of a small number of parameters, yet allowing for an extensive flexibility needed to describe any shape with good accuracy. The rest of this section deals with the description of the adopted parametrizations for the airfoil shapes and chord and twist distributions.

Airfoil parametrization

The geometry of the three base airfoils is parametrized by means of a composite Bézier curve based on 15 points, and made up of two 3rd-order Bézier curves and two 4th-order Bézier curves. A parametrization based on Bézier curves was chosen because, as shown in published applications such as those reported in [15, 18], it allows one to use a relatively small number of parameters, yet allowing for a high flexibility needed to describe any airfoil shape with good accuracy. As mentioned in Chapter 1, many other airfoil parametrizations with attractive properties are available. However, in this work, only Bézier curves were taken into account, as they were able to fulfill the aforementioned requirements. The airfoil parametrization is illustrated in Fig. 5.1. The rear part of the airfoil upper side is based on points 1, 2, 3, 4, and is defined by a 3rd order Bézier curve; the front part of the upper side is based on points 4, 5, 6, 7, 8, and is defined by a 4th order Bézier curve; the front part of the lower side is based on points 8, 9, 10, 11, 12, and is defined by a 4th order Bézier curve; the rear part of the lower side is based on points 12, 13, 14, 15, and defined by a 3rd order Bézier curve. Position (C^0), tangent (C^1) and curvature (C^2) continuity was enforced at the junction points 4, 8 and 12. In the optimization process, points 4, 5, 6, 7, 11 and 12 were actively controlled in both x- and y-directions, while points 1 and 15 were controlled only along the y-direction. This corresponds to 14 degrees of freedom. The leading edge position (point 8) is fixed at $(x = 0, y = 0)$. Once the position of points 4, 5, 6, 7, 11 and 12 is assigned,

the coordinates of points 2, 3, 9, 10, 13 and 14 are determined by enforcing C^0, C^1 and C^2 continuity at the junctions 4, 8 and 12. Thus, each of the 3 base airfoils is described by 14 independent variables, and therefore 42 design variables, labeled $b_i,\ i = 1, 2, ..., 42$, are used to define the blade airfoils from root to tip. For more details about composite Bézier curves and their continuity, one is referred to [129, 130].

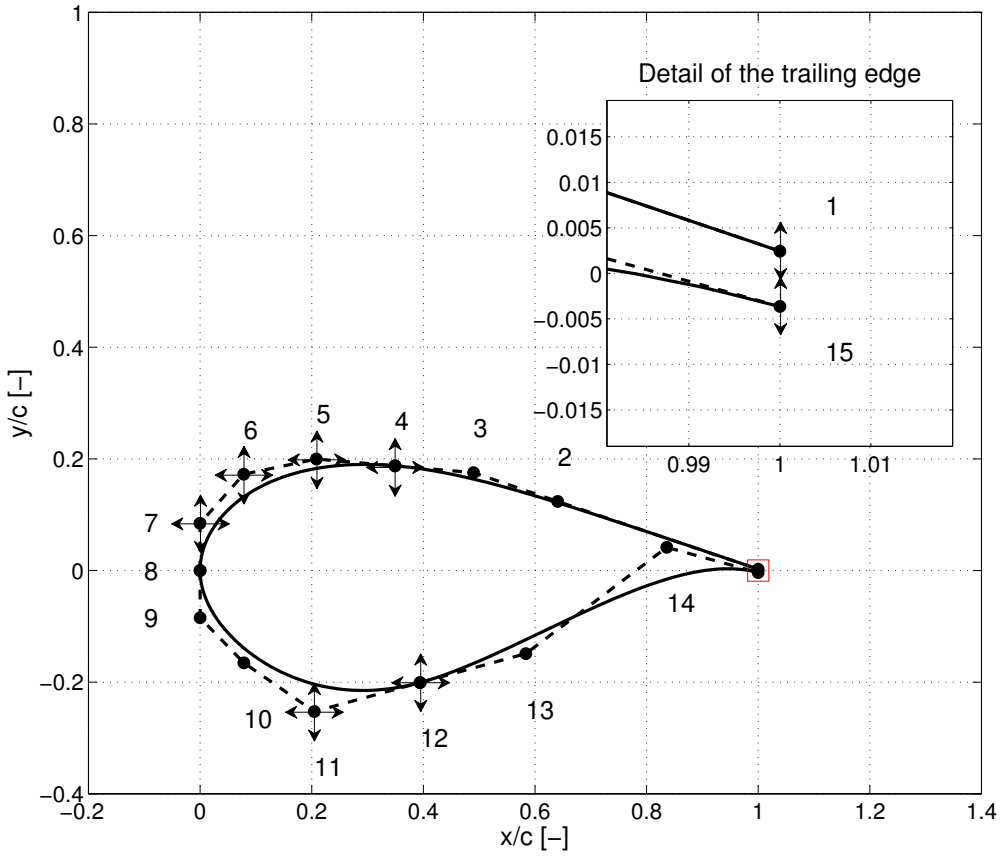

Fig. 5.1 Airfoil parametrization. The airfoil shape is defined by a composite Bézier curve controlled by 15 points. Horizontal and vertical arrows denote the actual degrees of freedom.

Parametrization of chord and twist distributions

The radial profiles of blade chord and twist angle were parametrized by means of a shape preserving piecewise cubic interpolation technique implemented in the `pchip` MATLAB function, using 5 control points for the chord distribution and 4 control points for the twist distribution. The only requirement associated to the parametrization of the chord and twist

angle parametrization was the continuity of the first derivative of the curve connecting the control points. The `pchip` MATLAB function was chosen because it is able to fulfill the first derivative continuity requirement, and available in the MATLAB package used to carry out the work reported in this thesis. The control points of the chord profile 1, 3, 4, 5 are fixed at 0%, 50%, 83.33% and 100% blade span, respectively, whereas point 2 is actively controlled also in the radial direction. Hence, 6 independent design variables, labeled $b_i,\ i = 43,44,...,48$, are used to define the chord profile. The active degrees of freedom for the parametrization of the chord profile are reported in the left subplot of Fig. 5.2. The control points of the twist profile 1, 2, 3, 4 are fixed at 16.67%, 50%, 83.33% and 100% blade span, respectively. Hence, 4 independent design variables, labeled $b_i,\ i = 49,50,...,52$, are used to define the twist profile. The active degrees of freedom for the parametrization of the twist profile are reported in the right subplot of Fig. 5.2.

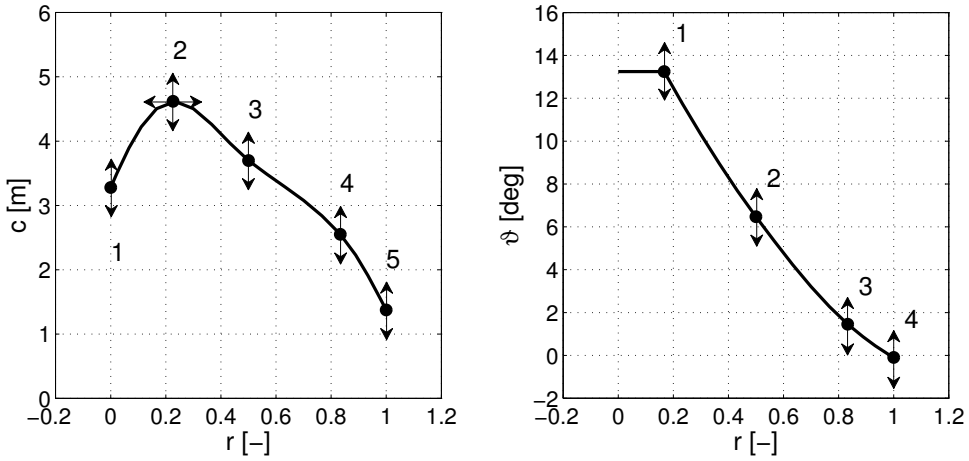

Fig. 5.2 Parametrization of chord distribution (left subplot) and twist distribution (right subplot). The chord distribution is defined by a cubic spline based on 5 points, and the twist distribution is defined by a cubic spline based on 4 points. Horizontal and vertical arrows denote the actual degrees of freedom.

5.1.2 Parametrization of the rotor speed

Turbine power control is accomplished by means of variable-speed and variable-pitch.

This control strategy is based on two independent control systems: a generator-torque controller and a full-span rotor-collective blade-pitch controller [36]. The former controller

aims at maximizing the rotor power capture below the rated wind speed, while the latter one is used to regulate the rotor speed above the rated wind speed. As is typical in utility-scale multi-megawatt wind turbines, both the generator-torque and blade-pitch controllers use the generator speed measurement as the sole feedback input [36]. In this work, the design specifications include that the cut-in and cut-out wind speeds are 3.0 and 25.0 m/s respectively, and the rated electrical power is 5 MW. A typical rotor speed ω curve is reported in the left subplot of Fig. 5.3. The right subplot of Fig. 5.3 shows the corresponding tip-speed ratio λ curve. λ is defined as follows:

$$\lambda = \frac{\omega R}{u} \tag{5.1}$$

where R is the rotor radius and u is the wind speed. The ω and λ curves consist of 5 regions

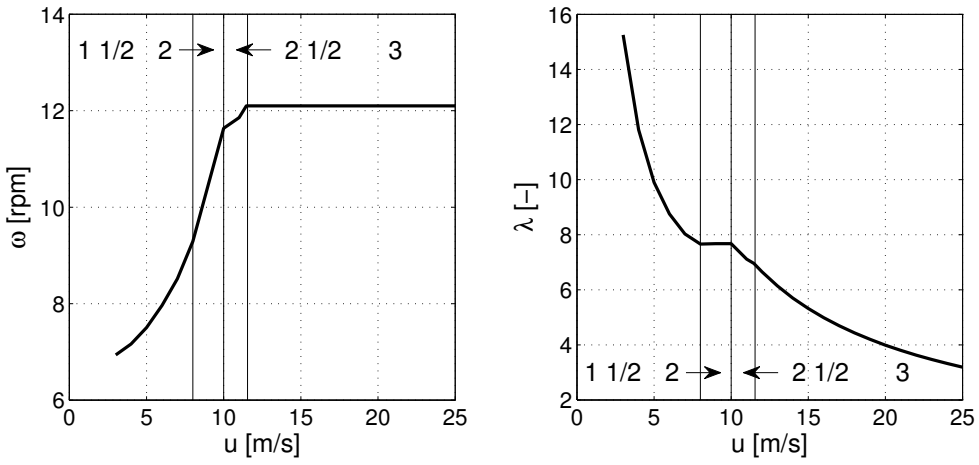

Fig. 5.3 Rotor speed (left subplot) and tip-speed ratio (right subplot) against wind speed. Left and right subplots report different control regions.

denoted respectively by 1 (not shown), 1½, 2, 2½ and 3. Region 1 is a region below the cut-in wind speed in which no power is generated, instead the wind is used to accelerate the rotor. In region 2, below the rated wind speed, the power capture is optimized by making the rotor work at a constant optimal tip-speed ratio, allowing it to operate at the peak power coefficient. In region 3, above the rated wind speed, the generator speed, and hence the generator power, are maintained constant by varying the blade pitch. Region 1½ is a transition region between regions 1 and 2, while region 2½ is a transition region between regions 2 and 3. Region 1½ is used to place a lower limit on the generator speed, limiting the wind turbine's operational

speed range. Region 2½ is needed to limit the tip speed (and therefore noise emissions) at rated power and above the rated wind speed. Control in regions 1½, 2, 2½ is accomplished by the generator-torque controller, while in region 3, the blade-pitch control system takes over. The generator torque versus generator speed response of the variable-speed controller is depicted in Fig. 5.4. Region 1½ is defined to span the range of generator speeds between 670 rpm and 871 rpm, while the transitional generator speed between regions 2½ and 3 is the 99% of the rated generator speed, or 1162 rpm. The generator-slip percentage in Region 2½ is taken to be 10%. Throughout region 2, the control torque (i.e., generator torque) τ_c is

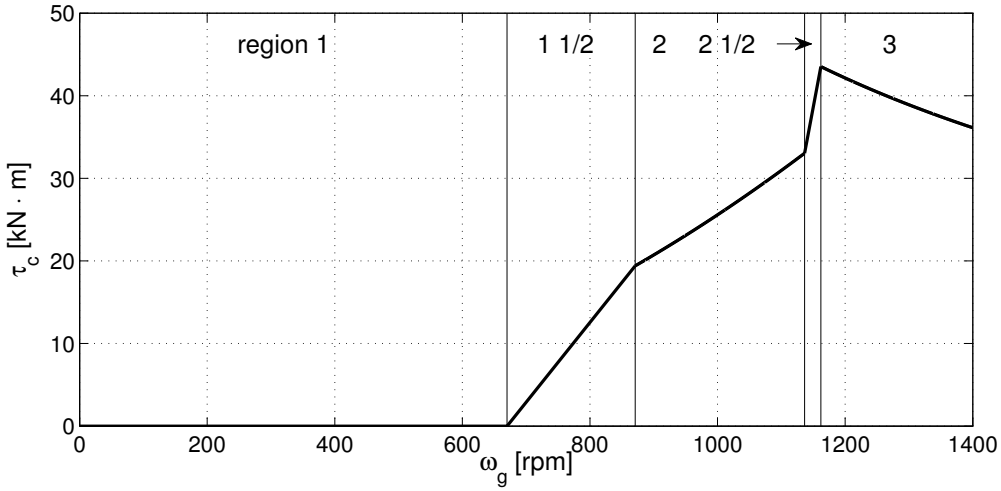

Fig. 5.4 Generator torque versus generator speed response of the variable-speed controller. Different control regions are shown.

used to maintain a constant λ. In this region, the control of the rotor speed is accomplished by varying τ_c proportionally to the square of the generator speed ω_g, that is by imposing:

$$\tau_c = K\omega_g^2 \tag{5.2}$$

where K is a constant of proportionality.

A typical power curve corresponding to the control strategy described above is reported in Fig. 5.5. In the design optimization reported below, the tip-speed ratio in region 2 is controlled by means of the torque control parameter K in Eq. 5.2, which is therefore treated as a design variable, and is labeled b_{53}.

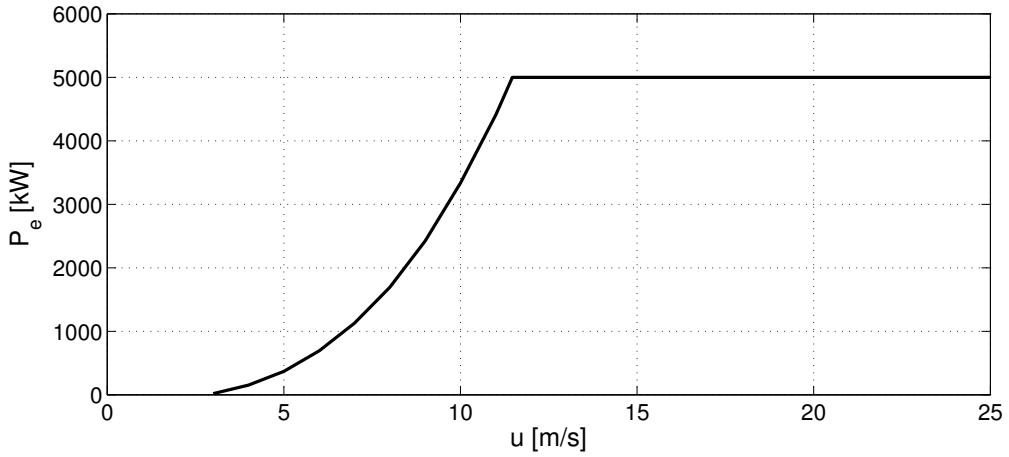

Fig. 5.5 Turbine electrical power against wind speed.

5.1.3 Internal structural layup parametrization

The blades were assumed to be fabricated from fiber-reinforced polymer, a composite material made of a polymer matrix reinforced with fibers. These types of composite blades are made up of stacks of laminas, the number and the thickness of which are piecewise constant along the cross-section periphery. A stack of laminas is commonly denoted by the term laminate. Figure 5.6 shows an example of a spar-cap type layup in which the primary bending loads are supported by the thick mid-sections, called spar caps, connected by shear webs, and the aerodynamic shape is maintained by sandwich panels around the blade periphery. The number of laminates along the section periphery, the number of laminas in each laminate, and the thickness of the laminas vary along the blade length. The webs may begin at any section and end at any other section on the blade. Each web is assumed straight and normal to the chord at each cross-section, and its cross-sectional dimensions and composites layup vary along the blade. Along the blade span, at each radial section, the internal structural layup of the blade was specified in terms of the number of laminates, lamina schedule of each laminate, orientation of fibers in each lamina, and the lamina constituent properties.

In this work, the internal structural layup of the blades is based on the Sandia 100-m all-glass baseline wind turbine blade [33]. Figure 5.7 illustrates graphically the laminate placement and the lamina schedule of each laminate. Each blade consists of nine laminates, that constitute the root build-up, leading edge panel (LEP), spar cap, trailing edge panel (TEP), shear webs, and blade tip. The principal two shear webs extend from 2.2 to 95.5% of the blade span. The third shear web begins at 14.3% of the blade span and ends at 58% of the blade span. Each of these laminates shown in Fig. 5.7 is characterized by a particular laminate schedule. The constituent material of each laminate is depicted in Table 5.1. The

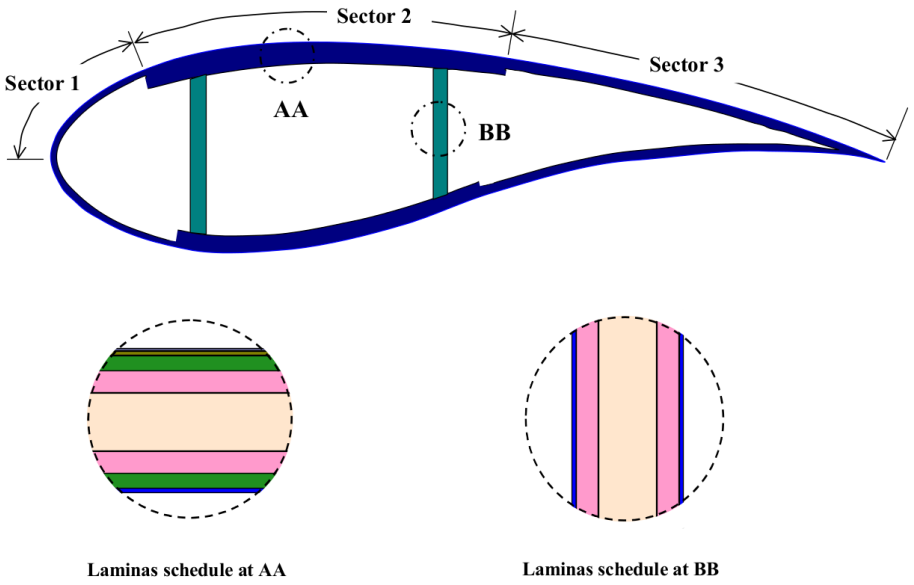

Fig. 5.6 Representative composite blade cross-section using two shear webs to define a spar-cap type layup. The upper and lower surfaces are each defined by three laminates organized in three peripheral sectors. Each shear web is instead defined by a single laminate. Lamina schedules of the top spar cap and the right shear web are shown. Image reproduced from [65].

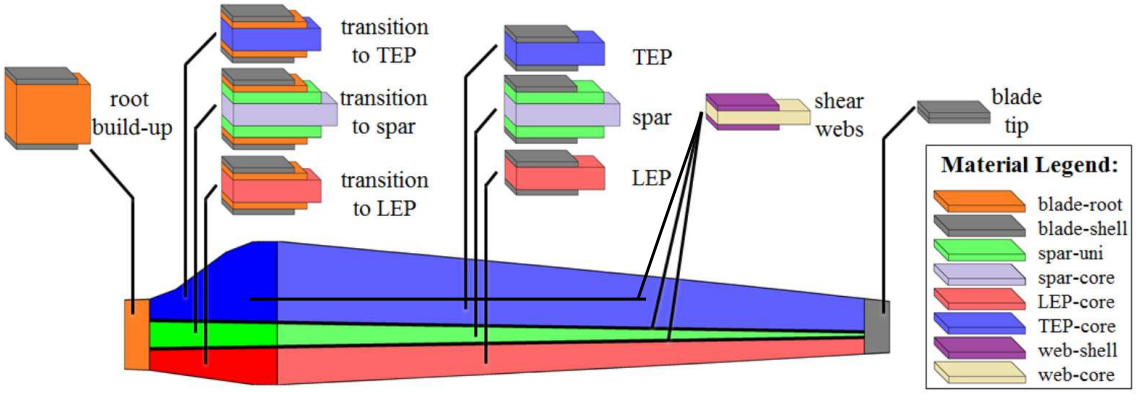

Fig. 5.7 Planform view of the turbine blade configuration used in the optimization study, showing the laminate schedules in the root build-up, LEP, spar cap, TEP, shear webs, and blade tip. For each laminate the constituent material are shown. Image reproduced from [69].

structural configuration uses a combination of composite materials and a structural foam. NCT307-D1-E300 and NCT307-D1-34-600-G300 are composite materials incorporating fiberglass in an epoxy resin matrix. NCT307-D1-34-600-G300 is a composite material made up of carbon fibers in a epoxy resin matrix. The Gurit Corecell M-foam M200 is a structural foam developed for marine applications. Mechanical properties of these materials

	material
blade-root	NCT307-D1-E300
blade-shell	NB307-D1-7781-497A
spar-uni	NCT307-D1-34-600-G300
spar-core	Gurit Corecell M-foam M200
LEP-core	Gurit Corecell M-foam M200
TEP-core	Gurit Corecell M-foam M200
web-shell	NB307-D1-7781-497A
web-core	Gurit Corecell M-foam M200

Table 5.1 Blade laminate constituent materials.

are depicted in Table 5.2 [131]. The Sandia layup is characterized by a given laminate

	E_{11} [GPa]	E_{22} [GPa]	G_{12} [GPa]	ν_{12} [-]	ρ [kg/m^3]
NCT307-D1-E300	35.5	8.33	4.12	0.33	1780
NB307-D1-7781-497A	19.2	19.2	3.95	0.13	1670
NCT307-D1-34-600-G300	123	8.2	4.71	0.31	1470
Gurit Corecell M-foam M200	0.21	0.21	0.098	0.33	200

Table 5.2 Mechanical properties of the materials used to define the composite laminates of the blades. E_{11} and E_{22} represent the principal and the lateral Young's moduli, respectively. G_{12} is the shear modulus. ν_{12} is the Poisson ratio. ρ is the density.

thickness distribution along the blade span. During the optimizations performed in this thesis, all characteristics of the Sandia layup were kept constant, except the thickness of the laminates making up the blade. During the optimization, the thickness of each laminate is controlled with a constant of proportionality s multiplying the laminate thickness of the Sandia turbine blade. Therefore, the parameter s is the design variable controlling the blade internal structure and is labeled b_{54}.

5.2 Design space

The design space $\boldsymbol{b}$ in which the optimum is sought is defined by the set of design variables presented above, and could be expressed as follows:

$$\boldsymbol{b} = \{b_1, ..., b_{54}\} \tag{5.3}$$

The ranges of variability, or bounds, within which the design variables are allowed to vary are shown in Tables 5.3, 5.4, 5.5 and 5.6.

design variable	range of variability	variable name
b_1	$\in [-0.4975, 0.5025]$ [-]	$y/c(p_1)$
b_2	$\in [-0.1508, 0.8492]$ [-]	$x/c(p_2)$
b_3	$\in [-0.3123, 0.6877]$ [-]	$y/c(p_2)$
b_4	$\in [-0.2914, 0.7086]$ [-]	$x/c(p_3)$
b_5	$\in [-0.3001, 0.6999]$ [-]	$y/c(p_3)$
b_6	$\in [-0.4218, 0.5782]$ [-]	$x/c(p_4)$
b_7	$\in [-0.3274, 0.6726]$ [-]	$y/c(p_4)$
b_8	$\in [-0.5000, 0.5000]$ [-]	$x/c(p_5)$
b_9	$\in [-0.4155, 0.5845]$ [-]	$y/c(p_5)$
b_{10}	$\in [-0.2953, 0.7047]$ [-]	$x/c(p_6)$
b_{11}	$\in [-0.7524, 0.2476]$ [-]	$y/c(p_6)$
b_{12}	$\in [-0.1058, 0.8942]$ [-]	$x/c(p_7)$
b_{13}	$\in [-0.7006, 0.2994]$ [-]	$y/c(p_7)$
b_{14}	$\in [-0.5036, 0.4964]$ [-]	$y/c(p_8)$

Table 5.3 Design variable bounds of the root airfoil (see Fig. 5.8).

design variable	range of variability	variable name
b_{15}	$\in [-0.4979, 0.5021]$ [-]	$y/c(p_9)$
b_{16}	$\in [-0.1974, 0.8026]$ [-]	$x/c(p_{10})$
b_{17}	$\in [-0.3729, 0.6271]$ [-]	$y/c(p_{10})$
b_{18}	$\in [-0.2570, 0.7430]$ [-]	$x/c(p_{11})$
b_{19}	$\in [-0.3766, 0.6234]$ [-]	$y/c(p_{11})$
b_{20}	$\in [-0.2500, 0.7500]$ [-]	$x/c(p_{12})$
b_{21}	$\in [-0.3735, 0.6265]$ [-]	$y/c(p_{12})$
b_{22}	$\in [-0.4981, 0.5019]$ [-]	$x/c(p_{13})$
b_{23}	$\in [-0.4231, 0.5769]$ [-]	$y/c(p_{13})$
b_{24}	$\in [-0.0481, 0.9519]$ [-]	$x/c(p_{14})$
b_{25}	$\in [-0.6147, 0.3853]$ [-]	$y/c(p_{14})$
b_{26}	$\in [0.1030, 1.1030]$ [-]	$x/c(p_{15})$
b_{27}	$\in [-0.5617, 0.4383]$ [-]	$y/c(p_{15})$
b_{28}	$\in [-0.5023, 0.4977]$ [-]	$y/c(p_{16})$

Table 5.4 Design variable bounds of the midspan airfoil (see Fig. 5.9).

design variable	range of variability	variable name
b_{29}	$\in [-0.4994, 0.5006]$ [-]	$y/c(p_{17})$
b_{30}	$\in [-0.1259, 0.8741]$ [-]	$x/c(p_{18})$
b_{31}	$\in [-0.3819, 0.6181]$ [-]	$y/c(p_{18})$
b_{32}	$\in [-0.3005, 0.6995]$ [-]	$x/c(p_{19})$
b_{33}	$\in [-0.3842, 0.6158]$ [-]	$y/c(p_{19})$
b_{34}	$\in [-0.4609, 0.5391]$ [-]	$x/c(p_{20})$
b_{35}	$\in [-0.4393, 0.5607]$ [-]	$y/c(p_{20})$
b_{36}	$\in [-0.4992, 0.5008]$ [-]	$x/c(p_{21})$
b_{37}	$\in [-0.4736, 0.5264]$ [-]	$y/c(p_{21})$
b_{38}	$\in [-0.2712, 0.7288]$ [-]	$x/c(p_{22})$
b_{39}	$\in [-0.5745, 0.4255]$ [-]	$y/c(p_{22})$
b_{40}	$\in [-0.0681, 0.9319]$ [-]	$x/c(p_{23})$
b_{41}	$\in [-0.5581, 0.4419]$ [-]	$y/c(p_{23})$
b_{42}	$\in [-0.4994, 0.5006]$ [-]	$y/c(p_{24})$

Table 5.5 Design variable bounds of the tip airfoil (see Fig. 5.10).

design variable	range of variability	variable name
b_{43}	$\in [0.1000, 5.5000]$ [m]	$c(c_1)$
b_{44}	$\in [0.1000, 5.5000]$ [m]	$c(c_2)$
b_{45}	$\in [1.0000, 50.0000]$ [m]	$r(c_2)$
b_{46}	$\in [0.1000, 5.5000]$ [m]	$c(c_3)$
b_{47}	$\in [0.1000, 5.5000]$ [m]	$c(c_4)$
b_{48}	$\in [0.1000, 5.5000]$ [m]	$c(c_5)$
b_{49}	$\in [-1.7507, 28.2493]$ [deg]	$\vartheta(\vartheta_1)$
b_{50}	$\in [-8.5235, 21.4765]$ [deg]	$\vartheta(\vartheta_2)$
b_{51}	$\in [-13.5416, 16.4584]$ [deg]	$\vartheta(\vartheta_3)$
b_{52}	$\in [-15.0968, 14.9032]$ [deg]	$\vartheta(\vartheta_4)$
b_{53}	$\in [1.0000, 2.8526]$ [N $\cdot$ m/s^2]	K
b_{54}	$\in [0.1000, 2.5000]$ [-]	s

Table 5.6 Design variable bounds of chord and twist distributions (see Fig. 5.11), torque control parameter and thickness parameter.

5.3 Reference turbine definition

The reference turbine to which the optimal designs determined in Chapter 6 are compared is based on the NREL offshore 5-MW baseline wind turbine [36]. This turbine is a conventional three-blade variable-speed variable blade-pitch-to-feather-controlled HAWT with upwind rotor. The blade tip and root diameters are 126 and 3 m, respectively, the rotor hub is at 90

m above the sea level, and the cut-in and cut-out speeds are 3.0 and 25.0 m/s, respectively. From root to tip, each blade is modeled with seventeen sections, including two circular sections near the blade root, one section transitioning from the outermost circular section to the innermost airfoil section, and fourteen airfoil sections over the remainder of the blade. For each of these seventeen sections, airfoil polars are given for a single Re and an AoA range from -180 to 180 deg (more details on how these polars were determined can be found in [36]). This turbine belongs to a IEC standard class I[1] [17]. A turbine belonging to a IEC standard class I is designed to withstand climates for which the extreme 10 min average wind speed with a recurrence period of 50 years at turbine hub height is lower than or equal to 50.0 m/s. In several published papers and reports, like in [17], it is stated that the NREL offshore 5-MW baseline wind turbine is a class I turbine, defining the IEC reference wind speed. However, none of these references defines the IEC turbulence characteristics to be considered when dealing with this turbine. For this reason, in this thesis a medium turbulence intensity, denoted by the subscript "B", was assumed.

The NREL test case provides also the structural properties (e.g., stiffness and inertia properties) of various turbine components, such as nacelle, hub and tower. These properties are in fact fundamental to characterize the dynamic response of the whole turbine, and therefore they must be included in the aeroelastic modeling. The design of these structural components depends generally on the loading acting on the rotor. In particular, the rotor loads and therefore the sizing of the nacelle, hub and tower are related to the rotor swept area, hub height and machine rating [102]. In this work such properties are not varied in the course of the optimization, and therefore, the structural properties of the nacelle, hub and tower are considered constant in the aeroelastic simulations.

Before starting the design optimization, the geometry of the blade of the NREL 5-MW turbine given in [36] as well as its internal structural layup and the rotor speed have been redefined using the parametrization defined above. The resulting parametrized turbine was taken as the reference configuration. The NREL offshore 5-MW baseline test case does not provide detailed information regarding its internal structural layup. Structural characteristics of the blades are indeed described only in terms of span-variant properties, such as mass, moments of inertia, and stiffnesses. For such reason, in this work, an internal structural layup

[1] According to the IEC standard [28], the external conditions to be considered for the design of wind turbines depend on the characteristics of the intended installation site. Wind turbine IEC standard classes define these characteristics in terms of wind speed and turbulence parameters. For example, a turbine belonging to a IEC standard class II_C is designed to withstand climates for which the extreme 10 min average wind speed with a recurrence period of 50 years at turbine hub height is lower than or equal to 42.5 m/s. The subscript "C" indicates that a hub height turbulence intensity, at a 10 min average wind speed of 15 m/s, equal to 0.12 is considered. In this context, turbulence intensity is defined as the ratio of the wind speed standard deviation to the mean wind speed.

based on the Sandia 100-m all-glass baseline wind turbine blade was adopted. As shown below, the use of this layup resulted in different blade span-variant structural properties with respect to those of the original NREL test case. However, in this study, the purpose of defining a reference turbine was not to replicate the same performance and characteristics of the NREL offshore 5-MW baseline wind turbine. Instead, the definition of a reference turbine was needed both to build a convenient initial solution for the optimizations, and to determine the performance of a turbine configuration using the same modeling set-up of the multidisciplinary analysis used to redesign the turbine, and determine the performance of new designs. Therefore, the differences in performance and characteristics between the reference and the NREL turbines do not have any practical implications in the optimizations reported later in this thesis. Additional information on the design specifications and turbine definition of the original NREL 5-MW turbine are available in [36].

5.3.1 Definition of the reference turbine's airfoils

Parametrizing the external geometry of the reference turbine involved finding the best geometric fit for the NREL offshore 5-MW baseline wind turbine's root, midspan and tip airfoils, which are the DU 99-W-405, DU 91-W2-250 NACA 64-618 airfoils, respectively. These fittings were performed using the MATLAB pattern search algorithm, minimizing the root-mean-square error (RMSE) between the parametric airfoils and the NREL offshore 5-MW baseline wind turbine's ones. In practice, for each airfoil, the fitting problem was formulated and solved as follows:

$$\begin{gathered}\text{Find: } \boldsymbol{p} \\ \text{to minimize: RMSE}(\boldsymbol{p})\end{gathered} \tag{5.4}$$

where the symbol $\boldsymbol{p}$ represents the vector of the airfoil parametrization's independent variables, as depicted in Fig. 5.1. The RMSE was computed as follows:

$$\text{RMSE}(\boldsymbol{p}) = \sqrt{\frac{\sum_{t=1}^{n}(\hat{y}_t(\boldsymbol{p}) - y_t)^2}{n}} \tag{5.5}$$

where $(\hat{y}_t(\boldsymbol{p}) - y_t)$ represents the distance, measured along the y/c direction (see Fig. 5.1), between the parametric airfoil and the reference one. This distance was evaluated at $n = 200$ different locations, along the x/c direction, on both the suction and pressure sides of the airfoils. Figures 5.8, 5.9 and 5.10 show the comparison between the parametric reference turbine's airfoils and those of the NREL offshore 5-MW baseline wind turbine. These figures highlight the high flexibility of the adopted airfoil parametrization, describing with good

accuracy three different airfoil shapes. The RMSEs of the reference turbine's root, midspan and tip airfoils are equal to $4.337 \cdot 10^{-4}$, $3.915 \cdot 10^{-4}$ and $2.964 \cdot 10^{-4}$, respectively.

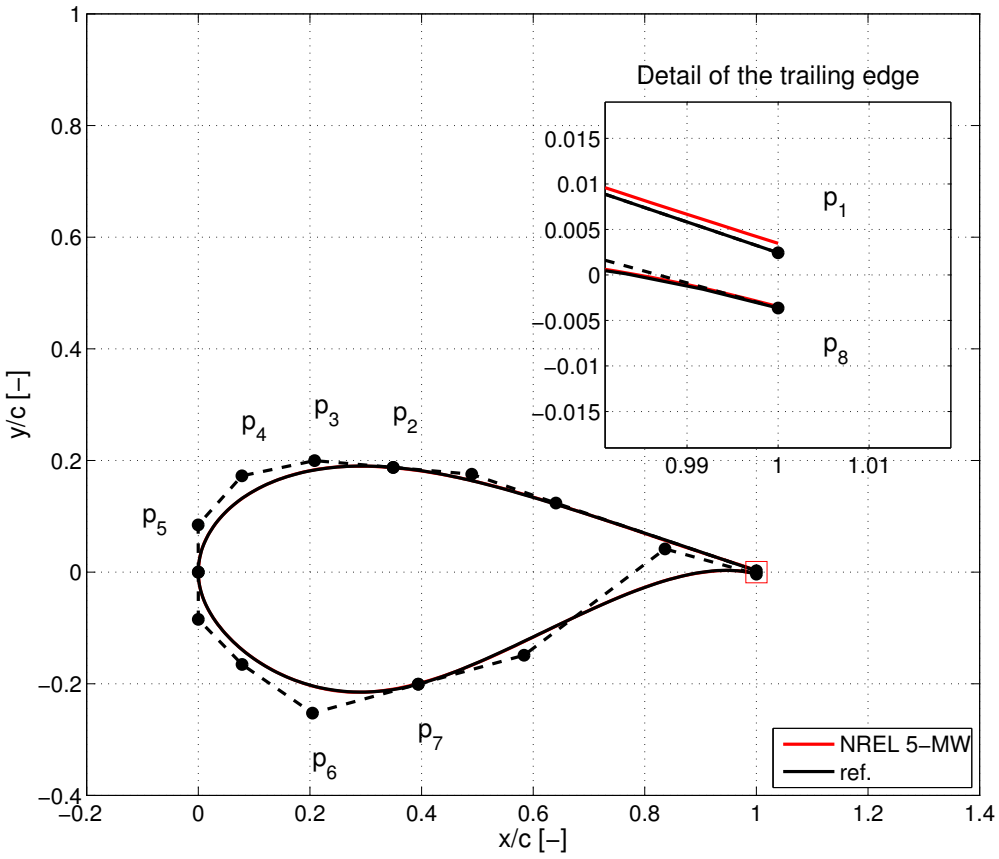

Fig. 5.8 Comparison between the NREL 5-MW baseline turbine's root airfoil and the parameterized reference one, determined as a best fit to the NREL 5-MW baseline turbine's root airfoil.

5.3.2 Definition of the reference turbine's chord and twist distributions

Control points of the reference turbine's chord and twist distributions were determined as the best fit to the NREL offshore 5-MW baseline wind turbine's ones. These fittings were carried out using the MATLAB pattern search algorithm, minimizing the RMSE between the parametric turbine's and the NREL offshore 5-MW baseline wind turbine's chord and twist

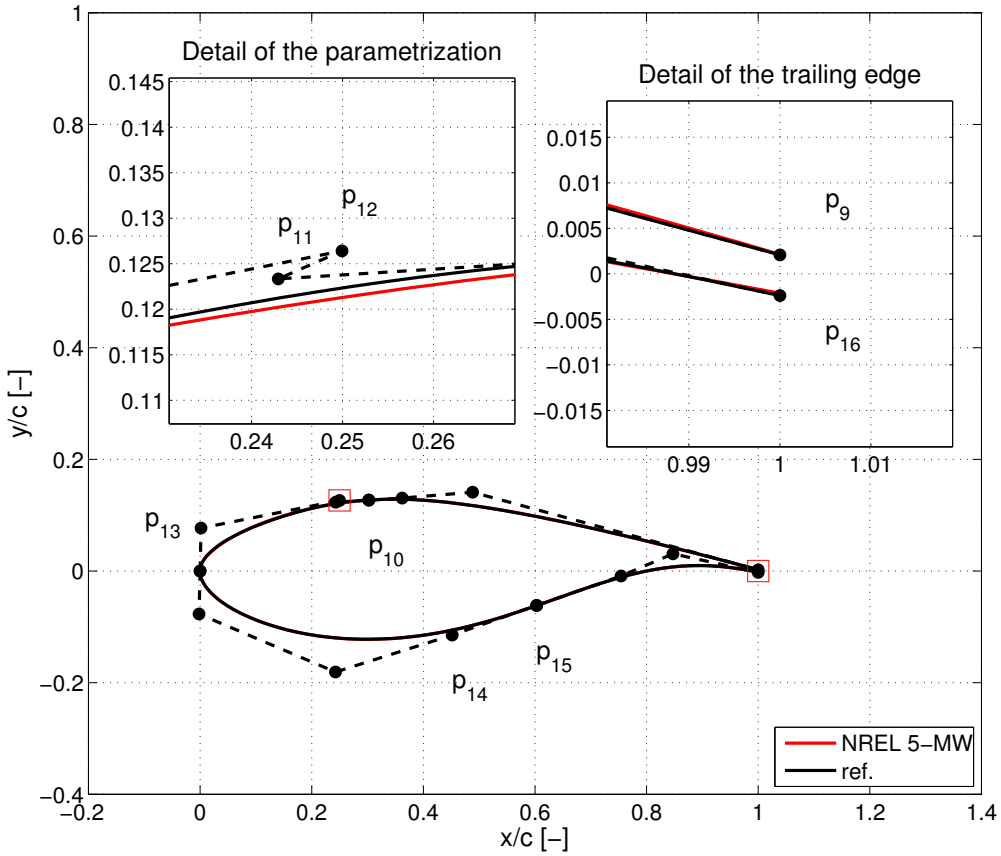

Fig. 5.9 Comparison between the NREL 5-MW baseline turbine's midspan airfoil and the parameterized reference one, determined as a best fit to the NREL 5-MW baseline turbine's midspan airfoil.

distributions. For the chord distribution, the fitting problem was formulated as follows:

$$\begin{aligned} &\text{Find: } \boldsymbol{c} \\ &\text{to minimize: } \mathrm{RMSE}(\boldsymbol{c}) \end{aligned} \tag{5.6}$$

where the symbol $\boldsymbol{c}$ represents the vector of the chord parametrization's design variables, as depicted in the left subplot of Fig. 5.2. The RMSE was computed as follows:

$$\mathrm{RMSE}(\boldsymbol{c}) = \sqrt{\frac{\sum_{t=1}^{n}(\hat{c}_t(\boldsymbol{c}) - c_t)^2}{n}} \tag{5.7}$$

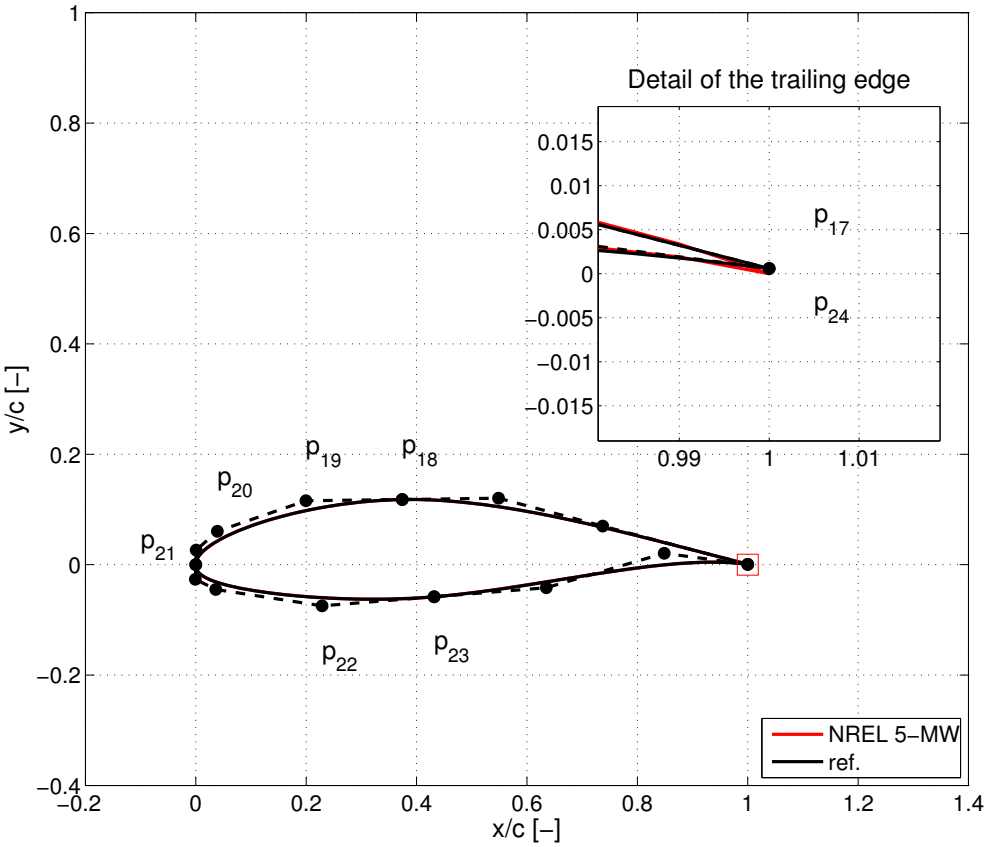

Fig. 5.10 Comparison between the NREL 5-MW baseline turbine's tip airfoil and the parameterized reference one, determined as a best fit to the NREL 5-MW baseline turbine's tip airfoil.

where $(\hat{c}_t(\boldsymbol{c}) - c_t)$ represents the difference between the parametric chord and the reference one, evaluated at $n = 100$ different radial locations. For the twist distribution, the fitting problem was formulated as follows:

$$\begin{aligned} &\text{Find: } \boldsymbol{\vartheta} \\ &\text{to minimize: } \mathrm{RMSE}(\boldsymbol{\vartheta}) \end{aligned} \tag{5.8}$$

where the symbol $\boldsymbol{\vartheta}$ represents the vector of the twist parametrization's design variables, as depicted in the right subplot of Fig. 5.2. The RMSE was computed as follows:

$$\mathrm{RMSE}(\boldsymbol{\vartheta}) = \sqrt{\frac{\sum_{t=1}^{n}(\hat{\vartheta}_t(\boldsymbol{\vartheta}) - \vartheta_t)^2}{n}} \tag{5.9}$$

where $(\hat{\vartheta}_t(\boldsymbol{\vartheta}) - \vartheta_t)$ represents the difference between the parametric twist and the reference one, evaluated at $n = 100$ different radial locations. Figure 5.11 shows the comparison between the parametric reference turbine's chord and twist distributions and those of the NREL offshore 5-MW baseline wind turbine. This figure shows that the developed parametrizations for chord and twist distributions are able to describe with accuracy the original shapes. The RMSEs of the reference turbine's chord and twist distributions are equal to $7.129 \cdot 10^{-2}$ m and $9.622 \cdot 10^{-2}$ deg, respectively.

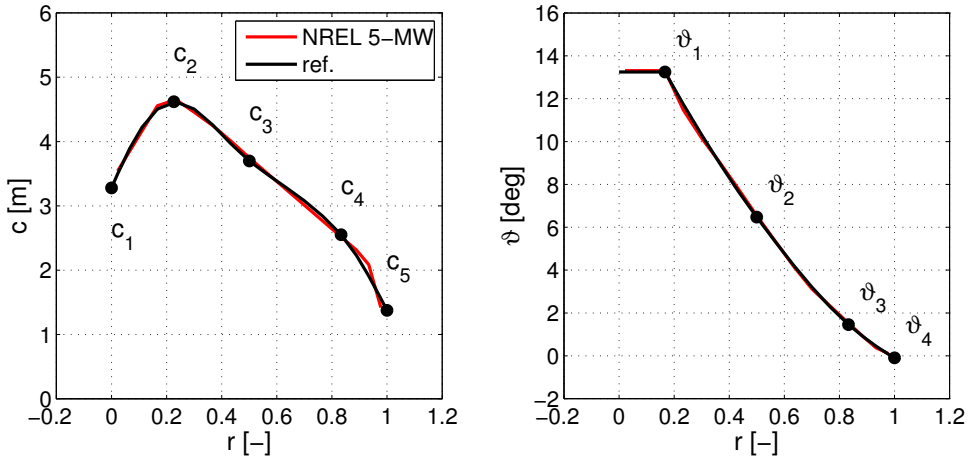

Fig. 5.11 Comparison between the reference turbine's chord and twist distributions and the NREL offshore 5-MW baseline wind turbine's ones.

5.3.3 Definition of the reference turbine's rotor speed and internal structural layup

In order to make a fair comparison between the optimized turbines and the reference one, both the torque control parameter, K, and the thickness parameter, s, of the reference turbine were optimized for minimum LCOE subject to the structural constraints described in Chapter 6 for

	NREL 5-MW	ref.
K [N · m/s^2]	2.33 (λ = 7.55)	2.13 (λ = 7.67)
s	-	0.964

Table 5.7 Torque control parameter with resulting tip-speed ratio in region 2 in parentheses, and thickness parameter of the reference turbine and the NREL offshore 5-MW baseline one.

a mean wind speed of 10.0 m/s. During this optimization, the aerodynamic forces required to determine the turbine power and the aerodynamic loads were determined as follows. Lift and drag coefficients of the two circular sections near the hub were assumed to be 0 and 0.5, respectively. Lift and drag coefficients of the sections between the outermost circular section and the root airfoil section were obtained by linear interpolation of the force coefficients of abovesaid limiting sections. 3D extended force coefficient of the root, midspan and tip airfoils were calculated by means of XFOIL/AERODAS. Lift and drag coefficients of all airfoils between the root airfoil and the tip airfoil were determined by linearly interpolating the force coefficients of the root, midspan and tip airfoils. The force coefficients thus determined were used as input variables by AeroDyn, the BEM libraries used by FAST to determine the radial distribution of the aerodynamic forces and the aerodynamic power. Co-Blade was used to determine the blade span-variant structural properties required by FAST. Co-Blade along with the definition of the internal structure of the blade, also requires a detailed geometric definition of the outer shape of the blade to determine its structural properties. The outer shape is defined by the chord and twist profiles, and the airfoil geometry at 34 radial positions, determined by linearly interpolating the blade sections defined by the hub circles, and the root, midspan and tip airfoils. The aerodynamic loads determined by FAST were then used to evaluate the objective function and constraints as explained in Chapter 4. The optimized value of K and s for the reference turbine are depicted in Table 5.7. In this table, K of the reference turbine and that of the NREL offshore 5-MW baseline turbine are compared. Table 5.7 reports also the resulting tip-speed ratio in region 2 in parentheses, showing that, in region 2, the reference turbine rotates at a speed 1.56% higher than the NREL one. As explain above, the parameter s cannot be associated with the NREL turbine, as its internal layup is not known. Instead, the parameter s refers to the internal structural layup based on the Sandia 100-m all-glass baseline wind turbine blade. At the beginning of the optimization, this parameter was set equal to 1 (i.e., the laminate thickness was equal to that of the Sandia turbine blade). As mentioned above, the use of an internal structural layup based on the Sandia turbine blade led to different structural properties with respect to the NREL turbine. This is particularly evident when comparing the blade weight of these two

	NREL 5-MW	ref.
w_b [kg]	$17.740 \cdot 10^3$	$44.216 \cdot 10^3$

Table 5.8 Blade mass of the reference turbine and the NREL offshore 5-MW baseline one.

turbines (Table 5.8). The reference blade is about 150% heavier that the NREL one. Such a difference could be reduced by adopting other structural layups, such as that reported in [34], or by optimizing the current layup by minimizing such differences.

The rotor speed and tip-speed ratio curves depicted respectively in the left and right subplots of Fig. 5.12 refer to the NREL 5-MW turbine and the modified reference turbine. These pictures shows that, from cut-in to rated wind speed, the rotor speed of the reference turbine is higher than that of the NREL 5-MW turbine. Fig. 5.13 shows a comparison

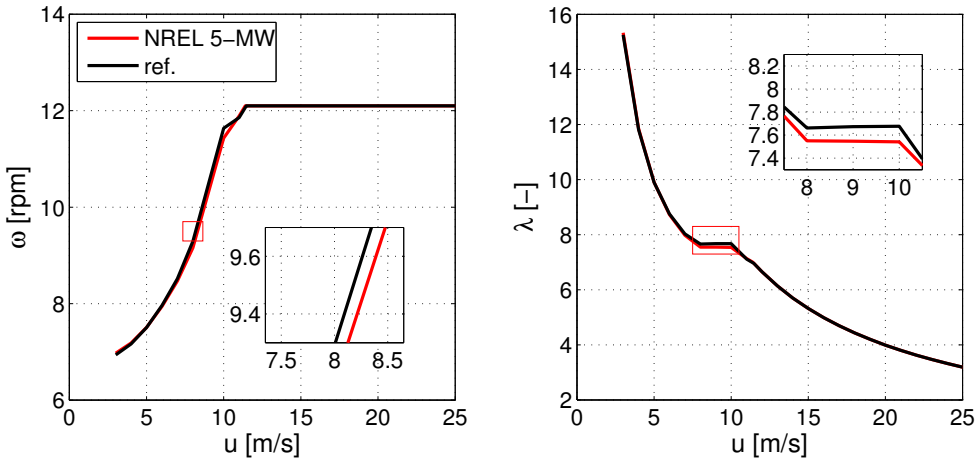

Fig. 5.12 Rotor speed (left subplot) and tip-speed ratio (right subplot) as a function of wind speed of the reference turbine and the NREL offshore 5-MW baseline wind turbine. Different control regions are shown in both subplots.

between the power curves determined for the NREL 5-MW and reference turbines from cut-in wind speed to cut-out wind speed. From cut-in to rated wind speed the NREL turbine is able to extract more energy than the reference one. This difference is primarily due to the fact that the reference turbine's power curve was calculated by considering a 1/7 wind profile power law, while the NREL turbine's power curve was evaluated considering a zero vertical wind shear.

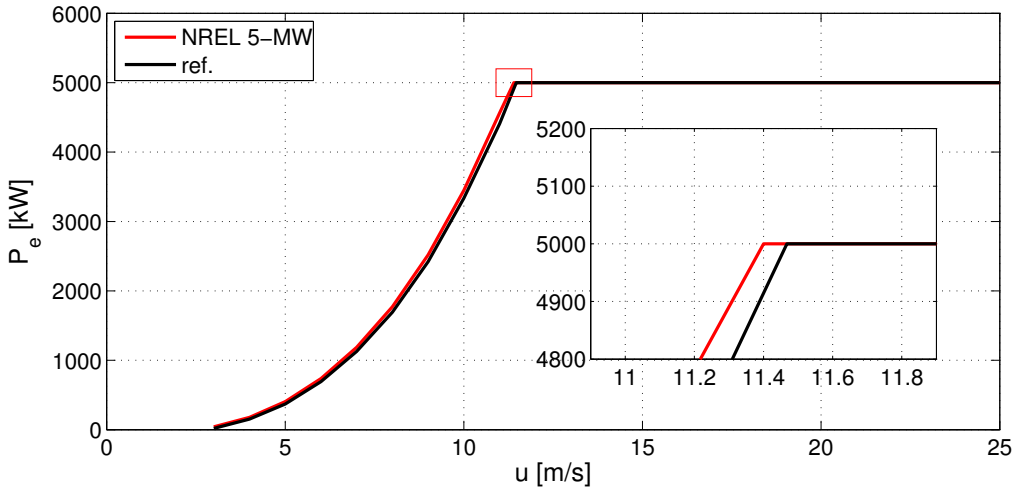

Fig. 5.13 Electrical power as a function of wind speed of the reference turbine and the NREL offshore 5-MW baseline wind turbine.

Chapter 6

HAWT design optimization under environmental uncertainty

In this chapter, the multidisciplinary and robust design optimization framework presented in Chapter 4 is demonstrated by performing the design optimization of a multi-megawatt HAWT rotor under environmental uncertainty. More specifically, the considered problem consisted of optimizing the design of the reference turbine defined in Chapter 5 so as to minimize the mean and the standard deviation of its LCOE when used at sites characterized by wind power density class from 3 to 7[1], in which the mean wind speed, based on a Rayleigh distribution, at 50 m above the ground ranges from 6.4 to 11.9 m/s[2]. At the actual reference turbine's hub height of 90 m, the mean wind speed, $\bar{u}$, determined using a vertical extrapolation based on the 1/7 power law, varies between 7.0 and 13.0 m/s. The design specifications are that the optimal turbine has the same rotor diameter, rated power, cut-in and cut-out speeds as the reference turbine.

The 54 blade geometry and control variables defined in Chapter 5 are optimized assuming the mean wind speed to be uniformly distributed in the abovesaid speed range. For comparison purposes, a deterministic optimization was performed as well. This optimization was carried out considering a fixed mean wind speed of 10 m/s. The aim of this chapter

[1] According to [132], the wind power density class defines the wind power density, expressed in W/m^2, and the mean wind speed, based on a Rayleigh speed distribution, of a given site. For example, in a site characterized by a wind power density class of 2, the wind power density varies between 200 and 300 W/m^2, with a mean wind speed, based on a Rayleigh speed distribution, ranging from 5.6 to 6.4 m/s at 50 m above the ground.

[2] As mentioned in Chapter 1, the probabilistic design scenario considered in this thesis was described by Ning et al. [17]. This scenario, as stated by Ning et al., may be simplistic. However, in the framework of this research work, it provided a plausible and feasible scenario to demonstrate the effectiveness of the developed optimization framework.

is to describe the deterministic and robust optimization problem formulations in terms of objective functions and constraints, and summarize the optimization results.

6.1 Objective function

The performance parameter considered in this study was LCOE, and the goal of the RDO exercise reported below was to minimize both the expectation and the standard deviation of LCOE considering the uncertainty affecting the mean wind speed, uniformly distributed within a given range of variability. This is a multi-objective design optimization problem, and it can be solved using either ad-hoc bi-objective optimization approaches [133], including evolution-based algorithms [20], or single-objective approaches [133]. Optimization of the mean often conflicts with minimization of the standard deviation, and, in this circumstance, a Pareto set of optimal solutions is encountered. As seen in Chapter 3, one of the simplest single-objective approaches to robust optimization is the weighted sum method, whereby a single objective function is obtained by considering a weighted average of mean and standard deviation of the performance parameter of interest. When a Pareto front exists, each of its points could be determined by varying the weights and solving a new optimization problem. Although rather simple to implement and often quite robust, this approach to the calculation of the entire Pareto front suffers from some limitations, including its inadequacy to determine non-convex regions of the front [134]. Making use of this approach, the objective function to be minimized in the considered HAWT design problem is:

$$f_{\text{rob}}(\boldsymbol{b},\bar{u}) = \alpha_w \left[\frac{\mu_{\text{LCOE}}(\boldsymbol{b},\bar{u})}{\mu^*_{\text{LCOE}}}\right] + (1-\alpha_w)\left[\frac{\sigma_{\text{LCOE}}(\boldsymbol{b},\bar{u})}{\sigma^*_{\text{LCOE}}}\right] \tag{6.1}$$

where $\boldsymbol{b}$ is the array of 54 design variables defined in Chapter 5, μ_{LCOE} and σ_{LCOE} are respectively the mean and the standard deviation of LCOE of the current HAWT design, and μ^*_{LCOE} and σ^*_{LCOE} denote the values of these two parameters for the reference turbine. These two values are thus used to normalize the probabilistic estimate of LCOE of all considered HAWT rotor designs. The constants α_w and $(1-\alpha_w)$ define respectively the weight assigned to μ_{LCOE} and σ_{LCOE}. The values of μ_{LCOE} and σ_{LCOE} for each considered HAWT configuration were evaluated by means of the Latin hypercube sampling, as explained in Chapter 4. Practically, the range of variability of the mean wind speed was divided into 100 intervals with equal probability[3]. Subsequently, LCOE was evaluated for the central

[3]The accuracy of the Latin hypercube sampling depends on the number of the selected equal probability intervals. The more intervals are considered, the more accurately this method can estimate the statistical

mean wind speed of each interval, and then μ_{LCOE} and σ_{LCOE} were calculated by means of Eqs. 4.6 and 4.7.

6.2 Constraints

The structural verification of wind turbines requires a large number of aeroelastic simulations in order to evaluate the loads that their components experience under design-driving scenarios. The purpose of these analyses is to make sure that the loads acting on the wind turbine over its lifetime do not lead to structural failure. The IEC 61400-3 [28] standard specifies an essential set of design requirements to ensure the structural integrity of offshore wind turbines. This standard prescribes a number of design load cases (DLCs) which define design scenarios to be considered during the structural design of wind turbine components. Considering these DLCs, the aim is to assess the turbine response with respect to the following analyses:

- ultimate load analysis;
- fatigue load analysis.

Ultimate load analysis refers to the assessment of material ultimate strength, blade tip deflection and structural stability (i.e., buckling), while fatigue load analysis concerns fatigue strength. The full set of DLCs includes, among others, normal, fault, and parked operating conditions, and considers both normal and extreme wind conditions. The IEC 61400-3 standard specifies also marine conditions (waves, sea currents, water level, etc.) which should be included in the design of offshore wind turbines. In this work, however, marine conditions were not considered. A few representative DLCs were taken into account in the present study, namely those denoted by 1.1, 1.2 and 6.1b. These load cases have shown to be the most likely design drivers for the majority of turbine blades [16, 33, 34]. In the framework of the presented optimization problem, each HAWT configuration generated during the course of the optimization process was assessed structurally by performing ultimate and fatigue load analyses, considering the DLCs 1.1, 1.2 and 6.1b. According to the conditions prescribed by these DLCs, described in detail in Sect. 6.2.1, ultimate and fatigue loads were evaluated through a series of aeroelastic simulations performed by means of FAST. As explained in Sect. 6.2.2, ultimate and fatigue loads were then augmented by means of safety factors in order to account for uncertainties and variabilities of various natures (such as in the evaluation of loads and materials) in the design procedure. Eventually, ultimate load analysis was carried out by means of Co-Blade, while fatigue loads were analyzed through MLife. Sect. 6.2.3 and

moments. A preliminary study has show that, for this particular application, 100 intervals allowed the method to converge.

Sect. 6.2.4 will outline the procedure followed for ultimate load analysis and fatigue load analysis, respectively.

6.2.1 Design load cases

The design scenarios prescribed by the DLCs depend primarily on the considered IEC standard class, which is defined in terms of wind speed and turbulence parameters of the intended installation site. In this study, a turbine class of I_B, defining a site reference wind speed of 50.0 m/s, and medium turbulence characteristics, was selected. According to the IEC standard, a turbine belonging to this class is designed to withstand climates for which the extreme 10 min average wind speed with a recurrence period of 50 years at turbine hub height, denoted by V_{ref}, is lower than or equal to 50.0 m/s, with a hub height turbulence intensity, at a 10 min average wind speed of 15 m/s, denoted by I_{ref}, equal to 0.14. Table 6.1 provides details of the DLCs 1.1, 1.2 and 6.1b for a I_B turbine class, showing the relative operation and wind conditions and the associated type of analysis. These DLCs are described

DLC	operating condition	wind conditions	type of analysis
1.1	normal	NTM 3 m/s < V_{hub} < 25 m/s	ultimate
1.2	normal	NTM 3 m/s < V_{hub} < 25 m/s	fatigue
6.1b	parked	steady EWM V_{hub} = 70 m/s	ultimate

Table 6.1 IEC DLCs considered in the structural verification of each wind turbine generated during the optimization process. The table shows the operation and wind conditions and the type of analysis related to each DLC. V_{hub} represents the wind speed at the hub height.

in detail below.

Design load cases 1.1 and 1.2

Considering normal operating conditions, the DLCs 1.1 and 1.2 involve the analysis of ultimate and fatigue loads, respectively, using the normal turbulence model (NTM) to define wind conditions. According to the NTM, a series of aeroelastic simulations were carried out considering different turbulent wind speed conditions, the mean value of which ranged from cut-in to cut-out wind speed. More specifically, from cut-in to cut-out, wind speed at the hub height was defined by 11 bins characterized by a size of 2.0 m/s, and mean equal to 4.0, 6.0, 8.0, 10.0, 12.0, 14.0, 16.0, 18.0, 20.0, 22.0 and 24.0 m/s, respectively. As recommended

by the standard, loads were estimated by 6 10-minute stochastic simulations for each of the 11 mean wind speeds considered. TurbSim was used to create the 10-minute turbulent wind files, using 6 different random seeds for each of the 11 mean wind speeds considered. According to the standard, all of these wind files were generated considering a power law shear profile with an exponent of 0.14. Turbulence intensity, I ,was given by [28]:

$$I = \frac{\sigma_1}{V_{\text{hub}}} \tag{6.2}$$

where σ_1 is the turbulence standard deviation, and V_{hub} represents the mean wind speed at the hub height. σ_1 can be evaluated as follows [28]:

$$\sigma_1 = I_{\text{ref}}(0.75V_{\text{hub}} + b) \tag{6.3}$$

where I_{ref} = 0.14 (for a class I_B turbine) and b = 5.6 m/s. These values are derived from [28]. With this configuration, 66 10-minute simulations were carried out for the DLCs 1.1 and 1.2. Ultimate and fatigue loads were evaluated concurrently, using the same turbulent wind files.

Design load case 6.1b

The DLC 6.1b considers the analysis of ultimate loads in parked conditions using the steady extreme wind speed model (EWM) for wind conditions. Parked conditions can be achieved in several ways, such as by pitching the blades towards feather, or by applying a high-speed shaft (HSS) brake control. In this work, the parked conditions were achieved by making the following assumption:

- The turbine's HSS brake is engaged for a parked configuration so that the rotor speed is fixed to zero.
- The turbine was parked with a blade pitch angle equal to 0 deg (i.e., the blade is flat to the wind).
- Computation of the induced velocities is turned off in AeroDyn because the rotor is stationary. This means that the calculation of the axial and tangential induction factors is bypassed during BEM computations, considering all induction factors equal to zero.

According to the EWM, a steady extreme wind speed, V_{e50}, with a recurrence period of 50 years of 70 m/s was considered. V_{e50} was calculated by using the following expression [28]:

$$V_{e50} = 1.4V_{\text{ref}} \tag{6.4}$$

where V_{ref} = 50 m/s (for a class I_B turbine). The analysis associated with the DLC 6.1b involved a single 100-second aeroelastic simulation[4], using a steady AeroDyn hub height wind file created by means of IECWind. More specifically, this file prescribed a horizontal wind, perpendicular to the rotor plane, with a speed of 70 m/s at the hub height. With reference to the wind speed at the hub height, wind speed at any other heights was determined by means of a power law shear profile with an exponent of 0.14. With this configuration, a 100-second simulation was carried out for the DLC 6.1b.

6.2.2 Safety factors

As already stated in the preceding sections, ultimate and fatigue analyses for the structural verification of HAWTs are carried out by means of aeroelastic simulations. These simulations can be affected by uncertainties related for instance to errors in the loading model or variations of the actual material strengths from the theoretical ones. In the ultimate and fatigue analyses, such uncertainties are taken into account by means of safety factors. Practically, these factors increase the ultimate and fatigue loads calculated by means of the aforementioned aeroelastic simulations. The IEC 61400-3 standard prescribes a set of specific safety factors, accounting for different types of uncertainty and variability. This set is made up of the following partial safety factors:

- partial safety factors for loads, δ_f;
- partial safety factors for materials, δ_m;
- partial safety factor for consequence of failure and component classes, δ_n.

δ_f takes into account possible unfavorable deviations/uncertainties of the load from the characteristic value, and uncertainties in the loading model. δ_m instead takes into account possible unfavorable deviations/uncertainties of the strength of material from the characteristic value, possible inaccurate assessment of the resistance of sections or load-carrying capacity of parts of the structure, and uncertainties in the geometrical parameters. The value of δ_n depends on the structural components making up wind turbines, and, in particular, on whether their failure may lead to the failure of a major part of the turbine. More specifically, according to the IEC 61400-3 standard, wind turbines are distinguished into classes that define whether a failure of one of their structural components can result in major turbine failures. In this work, a component class of 2 was used, meaning that the wind turbine failure may be caused by the failure of one of its components. The aforementioned partial safety factors, depicted

[4] Although steady wind conditions are considered by this DLC, a time-variant aeroelastic simulation was needed to assess the time-variant dynamic response of the blades.

in Table 6.2, are combined in total safety factors, δ_T, used in the load analyses. This table

	DLC	δ_f	δ_m	δ_n	δ_T
ultimate strength	1.1	1.25	1.3	1	1.625
	1.2	-	-	-	-
	6.1b	1.35	1.3	1	1.755
deflection	1.1	1.25	1.1	1	1.375
	1.2	-	-	-	-
	6.1b	1.35	1.1	1	1.485
buckling	1.1	1.25	1.2	1	1.5
	1.2	-	-	-	-
	6.1b	1.35	1.2	1	1.62
fatigue strength	1.1	-	-	-	-
	1.2	1	1.2	1.15	1.38
	6.1b	-	-	-	-

Table 6.2 Total safety factor, δ_T, used in the ultimate and fatigue load analyses. δ_f, δ_m and δ_n are respectively the partial safety factors for loads, materials, and consequence of failure and component classes.

shows that the value of the partial safety factors depend on both the considered DLC and the specific structural analysis carried out (e.g., ultimate strength, deflection, buckling and fatigue strength)

6.2.3 Ultimate load analysis

For each ultimate load analysis, carried out for both the DLCs 1.1 and 6.1b, blade laminate (tensile, σ_T, and compressive, σ_C) normal stress, panel (i.e., laminate) buckling and out-of-plane tip deflection, δ, were evaluated by means of Co-Blade. As explained in Chapter 2, panel buckling is treated by means of the dimensionless buckling criteria, R [69]. Maximum tensile and compressive stresses and buckling criteria were specifically calculated on the upper and lower surfaces, and webs of the blade at 4 radial sections fixed at 0%, 14.3%, 34% and 63.3% of its length. Maximum stresses, buckling criteria and tip deflections were evaluated on a blade in the 3 o'clock azimuth position, when looking downwind[5]. Due to the blade weight forces, such conditions represent the worst case for the edgewise loads.

Thus, regarding the ultimate load analysis, the objective function reported above was minimized subject to constraints on maximum allowable tensile and compressive stresses, buckling criteria and out-of-plane tip deflection. As depicted in Table 6.2, normal stresses,

[5]The rotor of the considered turbine rotates anticlockwise when looking downwind.

calculated by means of FAST, were augmented considering a total safety factor of 1.625 for the DLC 1.1, and a total safety factor of 1.755 for the DLC 6.1b. Laminate tensile and compressive yield strength were both considered equal to 325 MPa for simplicity[6]. Therefore, the maximum allowable tensile and compressive stresses were equal to 325 MPa and -325 MPa, respectively. Buckling loads were instead augmented by a total safety factor of 1.5 for the DLC 1.1, and by a total safety factor of 1.62 for the DLC 6.1b. The maximum allowable buckling criteria R was set equal to 1. Indeed, for this value of R, buckling loads become critical (i.e., lead to structural failure by buckling). Maximum allowable out-of-plane tip deflection was determined by dividing the total blade clearance in unloaded conditions, equal to 10.23 m, by a total safety factor of 1.375 for the DLC 1.1, and by a total safety factor of 1.485 for the DLC 6.1b. This resulted in a maximum allowable out-of-plane tip deflection of 7.44 m and 6.89 m for the DLC 1.1 and DLC 6.1b, respectively.

The total blade clearance in unloaded conditions is the distance between the tower and the blade tips in undeflected conditions. As shown in Fig. 6.1, the minimum clearance of a given blade is achieved when the blade in the 6 o'clock azimuth position. In this work, the tower diameter, T, was assumed constant along the tower span, and equal to 6 m. The rotor shaft overhang, O, of the turbine under investigation was equal to 5.019 m. The rotor shaft tilt angle, θ, and the blade precone angle[7], β, were equal to 5 and 2.5 deg, respectively. The distance between the blade tip and the rotor axis, R, was equal to 63 m. Therefore, the total blade clearance in unloaded conditions, C, of a blade in the 6 o'clock azimuth position can be calculated as follows:

$$\begin{aligned} C &= O\cos(\theta) + R\sin(\theta+\beta) - \frac{T}{2} = \\ &= 5.019 \cdot \cos(5 \cdot \pi/180) + 63 \cdot \sin(30 \cdot \pi/180) - \frac{6}{2} = 10.23 \text{ m} \end{aligned} \tag{6.5}$$

The constraints associated with the ultimate load analysis can be expressed by means the following nonlinear inequalities:

$$\sigma_T \leq 350 \text{ MPa} \tag{6.6}$$

[6]This approach has been followed also by Ashuri et al. [16]. These authors explain that the layup and the volumetric mixture of the elements that the composite sample is made of depends strongly on the blade yield stress. Exceeding this yield stress in some elements of a composite material does not necessarily mean the entire structure will fail, since the experienced load of that element will be distributed among other elements. Considering these facts, the defined value in this work is just a representative value suitable for the design applications.

[7]One way of increasing the distance between the blade tip and the tower is to orientate the blades with a so-called cone angle. In a HAWT, the rotor blades mounted on a hub rotate about a substantially horizontal axis, and the cone angle is formed by mounting the blades such that a longitudinal axis of the blade is not perpendicular to the rotational axis of the rotor [135].

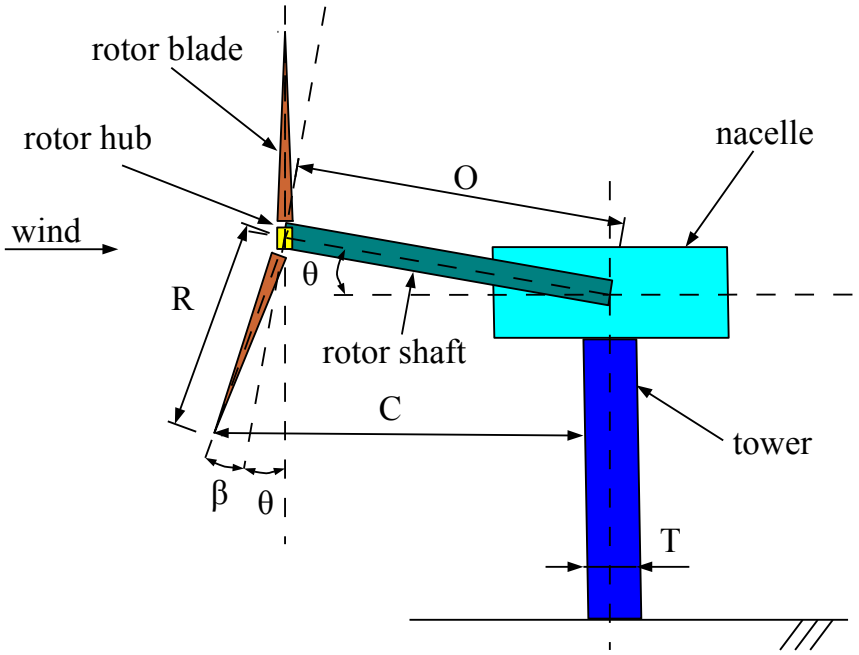

Fig. 6.1 Total blade clearance in unloaded conditions, C, of a blade in the 6 o'clock azimuth position. In this picture, T is the tower diameter (assumed constant along the tower length), O is the rotor shaft overhang, θ is the rotor shaft tilt angle, β is the blade precone angle and R is the distance between the blade tip and the rotor axis.

$$\sigma_C \leq -350 \text{ MPa} \tag{6.7}$$

$$R \leq 1 \tag{6.8}$$

$$\delta \leq 7.44 \text{ m} \quad \text{(DLC 1.1)} \tag{6.9}$$

$$\delta \leq 6.89 \text{ m} \quad \text{(DLC 6.1b)} \tag{6.10}$$

6.2.4 Fatigue load analysis

The fatigue load analysis is carried out considering the fluctuations of the in-plane and out-of-plane moments (i.e., moments caused by in-plane and out-of-plane forces, respectively) acting on the blade root, for a design lifetime of 20 years. In-plane and out-of-plane moment histories were obtained through a series of FAST simulations, according to the DLC 1.2 (as

explained in Sect. 6.2.1). In-plane and out-of-plane forces act respectively along the x- and y-direction of the FAST's coned coordinate framework. This coordinate system, depicted in Fig. 6.2, rotates with the rotor, but does not pitch with the blades. The origin of the FAST's

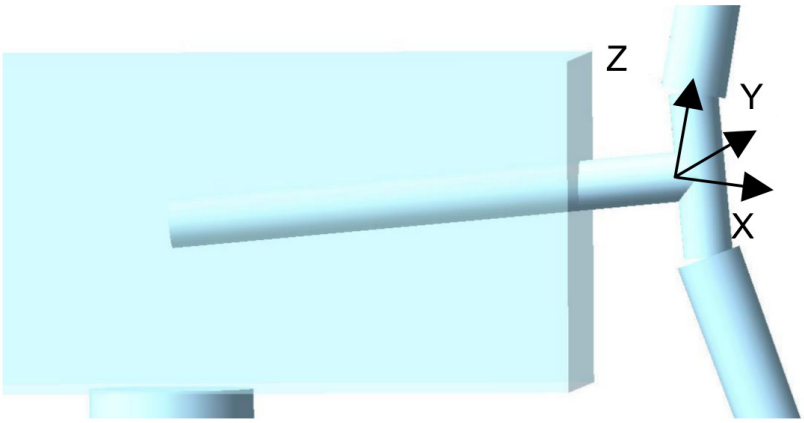

Fig. 6.2 FAST's coned coordinate system. Image reproduced from [136].

coned coordinate system is at the intersection of the rotor axis and the plane of rotation, for non coned rotors, or the apex of the cone of rotation, for coned rotors. y-axis points towards the trailing edge of blade along the chord line if the pitch and twist were zero. x-axis is orthogonal to the y-axis and the blade pitch axis. z-axis points along the pitch axis towards the tip of blade. In-plane and out-of-plane moment histories were processed by means of MLife (as explained in Chapter 2), which computed fatigue cycles for each time-series using rainflow counting, and applied the Miner's rule to eventually estimate the lifetime damage D. For design purposes, fatigue failure is assumed to occur when the lifetime damage is equal to 1. The relationship between load range and cycles to failure (S-N curve) was modeled by means of a Whöler exponent of 10.

In order to calculate the lifetime damage associated with the in-plane and out-of-plane moments acting on the blade root, the ultimate design in-plane and out-of-plane moments on the blade root needed to be specified. Practically, these ultimate moments lead the blade root to structural failure. Ultimate design blade root in-plane and out-of-plane moments, in particular, depend respectively on the in-plane and out-of-plane stiffnesses at the blade root. Since the shape of the blade at the root is circular, and the internal structural layup is constant along the cross-section periphery, the in-plane and out-of-plane stiffnesses at this section are assumed equal. Therefore also the ultimate design blade root in-plane and out-of-plane moments are constant. The blade root stiffness of the rotors generated during the course of the optimization varies. In particular, it depends directly on the chord length at the blade root, $c(c_1)$, and the value of the thickness parameter, s, defining the internal structural layup

thickness. Therefore, in a preprocessing step, Table 6.3 was generated, providing the value of the ultimate design blade root moments as a function of the chord length at the blade root, and the thickness parameter. Within this table interpolations were performed by means bilinear interpolation.

s [-] \ $c(c_1)$ [m]	0.1	1.9	3.7	5.5
0.1	28.367	16,453	64,298	139,940
0.9	283.67	119,140	510,600	1,172,500
1.7	3,782.3	179,660	869,920	2,042,400
2.5	1,4562	213,700	1,134,700	2,798,900

Table 6.3 Ultimate design blade root moment, expressed in kN·m, as a function of the chord length at the blade root, $c(c_1)$, and the thickness parameter, s.

Regarding the fatigue load analysis, the objective function reported above was minimized subject to constraints on the lifetime damage associated with the in-plane and out-of-plane moments, denoted respectively by $D_{(RootMxc1)}$ and $D_{(RootMyc1)}$. For each fatigue load analysis, carried out for the DLCs 1.2, in-plane and out-of-plane moments were augmented by a total safety factor of 1.38. The lifetime damage maximum allowed value was 1. Indeed, for this value of D, fatigue loads become critical (i.e., lead to structural failure by fatigue).

The constraints associated with the fatigue load analysis can be expressed by means the following nonlinear inequalities:

$$D_{(RootMxc1)} \leq 1 \tag{6.11}$$

$$D_{(RootMyc1)} \leq 1 \tag{6.12}$$

6.2.5 Constraint on maximum rotor speed

Wind turbines are generally designed taking into account noise. The blade tip speed is the most significant parameter affecting the turbine aerodynamic noise. In particular, aerodynamic noise can be controlled by lowering the blade tip speed. The latest generation of offshore wind turbines can operate at tip speeds up to 80 m/s [137]. Accordingly, in this work, as a surrogate for noise constraint, the maximum rotor speed was set equal to 12.1 rpm, leading to a tip speed of 80.0 m/s. Practically, this constraint was implemented by conveniently setting the controller of all turbines generated during the optimization in order to achieve a constant maximum rotor speed equal to 12.1 rpm.

6.2.6 Blade natural frequency analysis

In order to avoid blade resonance, a constraint on the minimum value of the blade first natural frequency, ω_1, was also enforced. Among all blade natural frequencies, the first natural frequency is the lowest, and therefore it was the only one considered here. Considering a safety factor of 1.1, the minimum allowable blade first natural frequency was set equal to the maximum blade passing frequency (calculated at the maximum rotor speed of 12.1 rpm), f_B. f_B was evaluated as follows:

$$f_B = 1.1 \cdot N_b f_R \tag{6.13}$$

where N_b is the number of blades (equal to 3), and f_R is the frequency corresponding to the maximum angular speed of the rotor (12.1 rpm) equal to

$$f_R = \frac{12.1}{60} = 0.202 \text{ Hz} \tag{6.14}$$

Therefore, for each of the turbines generated during the optimization, the minimum allowable blade first natural frequency, at a rotor speed of 12.1 rpm, was equal to 0.666 Hz.

The constraint associated with the blade first natural frequency can be expressed by means the following nonlinear inequality:

$$\omega_1 \geq 0.666 \text{ Hz} \tag{6.15}$$

6.2.7 Geometric feasibility checks

Each airfoil generated during the course of the optimization process was subject to a number of feasibility checks, aiming to avoid unphysical or unconventional shapes. These checks identified and discarded airfoils with self-intersecting shapes, and airfoils respectively with more than 1 and 2 changes in the curvature sign of the suction and pressure sides. Airfoil relative thicknesses and their chordwise locations are also subject to feasibility checks. Relative thickness of root, midspan and tip airfoils are enforced to vary within the ranges [38%, 42%], [23%, 27%] and [16%, 20%], respectively, while, for all airfoils, the location of maximum thickness was constrained to range between 20% and 40% of chord.

6.3 Problem formulation

Denoting by $g_j(\boldsymbol{b}, \bar{u})$ the set of nonlinear inequality constraints described by Eqs. 6.6, 6.7, 6.8, 6.9, 6.10, 6.11, 6.12 and 6.15, the robust optimization problem is:

$$\begin{aligned} \text{Find: } & \boldsymbol{b} = \{b_1, ..., b_{54}\} \\ \text{to minimize: } & f_{\text{rob}}(\boldsymbol{b}, \bar{u}) \\ \text{where: } & \bar{u} \sim U(\bar{u}_L, \bar{u}_U) \\ \text{subject to: } & g_j(\boldsymbol{b}, \bar{u}) \leq 0 \\ \text{and: } & \boldsymbol{b_L} \leq \boldsymbol{b} \leq \boldsymbol{b_U} \end{aligned} \tag{6.16}$$

where $f_{\text{rob}}(\boldsymbol{b}, \bar{u})$ is the objective function of the robust problem defined by Eq. 6.1. The symbols $\bar{u} \sim U(\bar{u}_L, \bar{u}_U)$ indicate that the mean wind speed $\bar{u}$ is uniformly distributed in the range from $\bar{u}_L$, equal to 7.0 m/s, to $\bar{u}_U$, equal to 13.0 m/s. $\boldsymbol{b_L}$ and $\boldsymbol{b_U}$ are respectively the lower and upper bounds of the design variables' variability ranges, as shown in Chapter 5. The deterministic optimization problem is instead formulated as follows:

$$\begin{aligned} \text{Find: } & \boldsymbol{b} = \{b_1, ..., b_{54}\} \\ \text{to minimize: } & f_{\text{det}}(\boldsymbol{b}, \bar{u}) \\ \text{where: } & \bar{u} = \bar{u}_{\text{det}} \\ \text{subject to: } & g_j(\boldsymbol{b}, \bar{u}) \leq 0 \\ \text{and: } & \boldsymbol{b_L} \leq \boldsymbol{b} \leq \boldsymbol{b_U} \end{aligned} \tag{6.17}$$

where $\bar{u}_{\text{det}}$ is equal to 10.0 m/s, and $f_{\text{det}}(\boldsymbol{b}, \bar{u})$ is objective function of the deterministic problem expressed as follows:

$$f_{\text{det}}(\boldsymbol{b}, \bar{u}) = \text{LCOE}(\boldsymbol{b}, \bar{u}) \tag{6.18}$$

All the constraints, $g_j(\boldsymbol{b}, \bar{u})$, appearing in Eq. 6.16 and Eq. 6.17 are treated deterministically (i.e., not considering the variability of the wind speed distribution mean). These constraints are treated in such a way primarily because they have been calculated by augmenting the loads by safety factors that consider various types of uncertainty. Moreover, these constraints do not depend on the wind speed distribution mean. Therefore, these constraints were evaluated for a single wind speed distribution mean equal to 10.0 m/s

6.4 Results and discussion

The purpose of this section is to illustrate and assess the results obtained for the robust and deterministic optimization problems formulated in Sect. 6.3. The aim of the robust optimization was to minimize both the expectation and the standard deviation of the LCOE of the reference 5-MW HAWT defined in Chapter 5, considering the uncertainty affecting the mean wind speed of the installation site. In the attempt to determine the Pareto front of optimal solutions using the weighted sum method illustrated in Sect. 6.1, several robust optimizations were performed by varying the weights given to μ_{LCOE} and σ_{LCOE} in Eq. 6.1. This assessment indicated that the Pareto front associated with the design problem under investigation is rather small. In this circumstance, variations of the weights do not result in designs yielding significantly different values of μ_{LCOE} and σ_{LCOE}. Therefore, in this section, a representative robust solution obtained giving equal weights to μ_{LCOE} and σ_{LCOE}, i.e., $\alpha_w = 0.5$, is considered. For comparison purposes, a deterministic optimization was performed along with the robust one. The goal of the deterministic optimization was to minimize the LCOE, considering a fixed mean wind speed of 10 m/s. The rest of this section deals with the comparison between the reference turbine and the robust and deterministic ones.

As reported in Table 6.4, the robust and deterministic optimizations led to the design of improved rotors with respect to the reference one, achieving a reduction in both μ_{LCOE} and σ_{LCOE}. With respect to the reference turbine, the robust optimization achieved a 7.69% and 12.5% reduction in μ_{LCOE} and σ_{LCOE}, respectively. The lower μ_{LCOE} was due primarily to the lower blade weight (- 44.01%), and the enhanced aerodynamic characteristics of the robust rotor, leading to a greater mean of AEP (+ 1.52%). The standard deviation of AEP of the robust configuration with respect to that of the reference turbine decreases by 0.70%. With respect to the reference configuration, the deterministic optimization achieves a 7.16% and 12.0% reduction in μ_{LCOE} and σ_{LCOE}, respectively. The lower μ_{LCOE} is due to the lower blade weight (- 38.81%), and the greater mean of AEP (+ 1.91%). The standard deviation of AEP of the deterministic configuration with respect to that of the reference turbine decreases by 0.93%. With reference to the deterministic optimum, the robust one is characterized by better overall performance, with lower μ_{LCOE} (- 0.57%) and σ_{LCOE} (- 0.59%). The enhancement of the robust rotor performance with respect to that of the deterministic one are related to the lower blade weight (- 8.50%), which compensates for a slightly lower mean of AEP (- 0.38%). The standard deviation of AEP of the robust configuration is 0.23% greater with respect to that of the deterministic turbine.

As depicted in Table 6.4, the deterministic and robust designs reported in this thesis have obtained by keeping the rotor diameter, rated power, cut-in and cut-out speeds constant

	ref.	det.	rob.
rated power [MW]	5	5	5
rotor diameter [m]	126	126	126
cut-in wind speed [m/s]	3	3	3
cut-out wind speed [m/s]	25	25	25
μ_{LCOE} [$ / kWh]	0.1132	0.1051	0.1045
σ_{LCOE} [$ / kWh]	0.0192	0.0169	0.0168
μ_{AEP} [kWh]	$23.03 \cdot 10^6$	$23.47 \cdot 10^6$	$23.38 \cdot 10^6$
σ_{AEP} [kWh]	$4.31 \cdot 10^6$	$4.27 \cdot 10^6$	$4.28 \cdot 10^6$
w_b [kg]	$44.216 \cdot 10^3$	$27.055 \cdot 10^3$	$24.755 \cdot 10^3$

Table 6.4 Comparison of the gross design specifications and overall performance of the reference, deterministic and robust designs. μ_{LCOE} and σ_{LCOE} are mean and standard deviation of LCOE, respectively; μ_{AEP} and σ_{AEP} are mean and standard deviation of AEP, respectively; w_b is the blade weight.

and equal to those of the reference turbine. As explained above, with reference to the deterministic optimum, the robust one is characterized by better overall performance, with 0.57% lower LCOE mean. Considering the same probabilistic scenario reported in the thesis, in the work of Ning et al. [17] the robust design has achieved a 1.2% lower average LCOE than that of a deterministically designed rotor. With respect to the results highlighted in this thesis, the higher reduction of the LCOE mean (of the robust rotor with respect to the deterministic one) achieved by Ning at al. is due to the fact that these authors considered, in addition to the design variables considered in the thesis, the diameter and rated power as design variables, allowing for a higher design space. Indeed, in the optimization process, the inclusion of the rotor diameter and turbine rated power as design variables allows greater freedom in the design search, allowing the generation of significantly diverse wind turbine configurations. Rotor diameter and turbine rated power, however, affect directly the design of several structural components of the turbine, such as the tower. Therefore, an optimization system that considers variations in rotor diameter and turbine rated power should be able to structurally assess turbine structural components, such as the tower, for each configuration generated during the course of the optimization process. At present, the optimization system presented in this thesis does not include suitable tools for the structural analysis of turbine structural components, focusing purely on the aeroservoelastic design of the rotor. Therefore, in this context, the rotor diameter and turbine rated power are not included as design variables, that is they are kept constant, which has allowed us to keep the same turbine structural components for each turbine.

The purpose of the rest of this chapter is to present and compare the characteristics of the reference, deterministic and robust design in detail. Table 6.5 compares the structural properties at selected wind speeds and radial positions for the reference, deterministic and robust blades. The ultimate load analysis of these turbines highlights that the maximum stresses, buckling criteria and tip deflections are achieved for the DLC 6.1b. As seen in Sect. 6.2.1, this DLC considers the turbine in parked conditions, subject to an extreme wind speed of 70 m/s. In such conditions, stresses, buckling criteria and tip deflections are evaluated on a blade in the 3 o'clock azimuth position, representing the worst case for the edgewise loads due to the blade weight forces. Under such conditions, the reference and the robust blades have an active constraint on the maximum allowable buckling criteria acting on the top surface of the blade at 63.3% span, while the deterministic and robust turbines have an active constraint on the maximum allowable tensile stress, on the bottom surface of the blade at 14.3% span. Table 6.5 reports also the maximum compressive stress σ_C acting on the top surface at the blade root section of the three blade designs, at a wind speed of 70.0 m/s for a blade in the 3 o'clock azimuth position. One sees that σ_C has increased considerably for the deterministic and robust designs, and it is respectively 19.43% and 3.71% lower than the allowed maximum values. At a wind speed of 70.0 m/s, the maximum tip deflections of the deterministic and robust blades are about 35.85% and 19.16% lower than the allowed maximum. Calculated from the cut-in and cut-out wind speeds, the means of the lifetime damage caused by the in-plane and out-of-plane moments at the blade root are well below the maximum allowed values for both the deterministic and robust turbines. The deterministic and robust blade first natural frequencies are 37.84% 34.38% higher than the minimum allowed value.

Figures 6.3 and 6.4 present respectively the comparison of the airfoils and force coefficients of the reference, deterministic and robust blade designs. The root, midspan and tip airfoils of the deterministic and robust designs feature a higher lift-to-drag ratio than that of the corresponding reference turbine airfoils. It is observed that, while the maximum airfoil thickness and the chordwise position where such maximum is achieved vary fairly little between corresponding airfoils of the three blade designs, the airfoils of the deterministic and robust blades are more cambered than those of the reference blade. The camber line, defined as the locus of the points midway between the suction and pressure sides, plays a crucial role in the improvements of the robust airfoils' aerodynamic performance. Indeed, the larger amount of camber of the deterministic and robust blade airfoils enables them to achieve a higher lift coefficient. This is particularly evident for the root airfoil, the maximum C_L of which is about 40% higher than that of the reference blade root airfoil. It is also observed that, with respect to the robust midspan and tip airfoils, for an AoA ranging from -5 to about

	u [m/s]	r [-]	surf.	ref.	det.	rob.	const.
σ_T [MPa]	70.0	0.143	bot	138	350	350	≤ 350
σ_C [MPa]	70.0	0	top	-50	-282	-337	$\geq$ -350
R	70.0	0.633	top	1.000	0.919	1.000	≤ 1
δ [m]	70.0	1	-	2.77	4.42	5.57	≤ 6.89
$D_{(RootMxc1)}$	(3.0, 25.0)	0	-	$1.4 \cdot 10^{-9}$	$1.5 \cdot 10^{-2}$	$4.9 \cdot 10^{-2}$	≤ 1
$D_{(RootMyc1)}$	(3.0, 25.0)	0	-	$2.5 \cdot 10^{-11}$	$1.2 \cdot 10^{-2}$	$4.7 \cdot 10^{-2}$	≤ 1
ω_1 [Hz]	-	-	-	1.173	0.918	0.895	≥ 0.666

Table 6.5 Comparison of the structural characteristics of the reference, deterministic and robust blade designs at selected wind speeds and radial positions. σ_T and σ_C denote tensile and the compressive stresses, respectively; R is the buckling criteria; δ is the tip deflection; $D_{(RootMxc1)}$ and $D_{(RootMyc1)}$ are the lifetime damages caused by the in-plane and out-of-plane moments at the blade root, respectively; ω_1 is the blade first natural frequency at a rotor speed of 12.1 rpm.

20 deg, the deterministic midspan and tip airfoils achieve higher lift-to-drag ratios. This is due to greater cambers. The optimization of the airfoil shapes is also driven by structural considerations. In particular, the midspan and tip airfoils have a lower mean radius of curvature over the aft portion of the suction side with respect to the reference airfoils. This results in an increase of the buckling strength of the blade laminates at a location characterized by a high buckling stress concentration (i.e., over the aft part of the top surface, at around half-span of the blade). Moreover, the root airfoil of the deterministic and robust turbines have a thicker trailing edge, improving in this way both the flapwise and edgewise bending stiffnesses.

Radial chord and twist profiles of the two designs are reported respectively in the left and right top subplots of Fig. 6.5. Due to smaller chord lengths of the deterministic and robust blade designs (top left subplot of Fig. 6.5), these rotors have a lower solidity at most radii, and this occurrence contributes significantly to decrease the blade weight. The blade weight reduction is also a result of the 6.95% and 13.69% decrease of the internal structure thickness parameter s of the deterministic and robust turbines, respectively (see Table 6.6). The deterministic and robust blade designs also have less twist than the reference design along the inboard part of the blade and more twist along the outboard part. The consequences of this trend are discussed below.

The left and right subplots of Fig. 6.6 report respectively the rotor speed and the tip-speed ratio of the three turbines against the wind speed. Figure 6.7 shows instead the power curve of the reference, deterministic and robust turbines. As expected, the power extracted by the deterministic and robust HAWT designs is higher than that of the reference turbine in regions 1½, 2 and 2½. The power extraction of the deterministic design in this wind speed range is

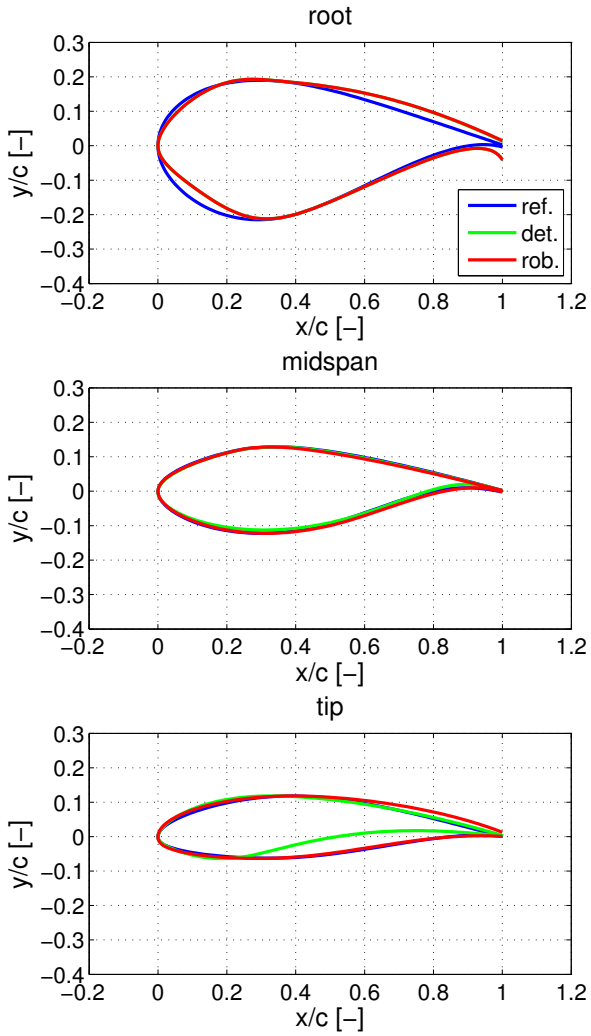

Fig. 6.3 Comparison of the base airfoil shapes of the reference, deterministic and robust designs.

higher than that of the robust one. It is also noted that the rotor speed of the robust turbine in region 2 is higher than that of the reference turbine, while the rotor speed of the deterministic turbine in region 2 is slightly lower than that of the reference turbine.

The torque control parameter, the tip-speed ratio in region 2, and the thickness parameter of the three turbines are provided in Table 6.6. These results highlight that the robust design features an increment of 3% of the tip-speed ratio in region 2, and a reduction of 13.69% of the thickness of the internal structure over the reference turbine. The deterministic design instead is characterized by a slight decrement of 0.26% of the tip-speed ratio in region 2, and

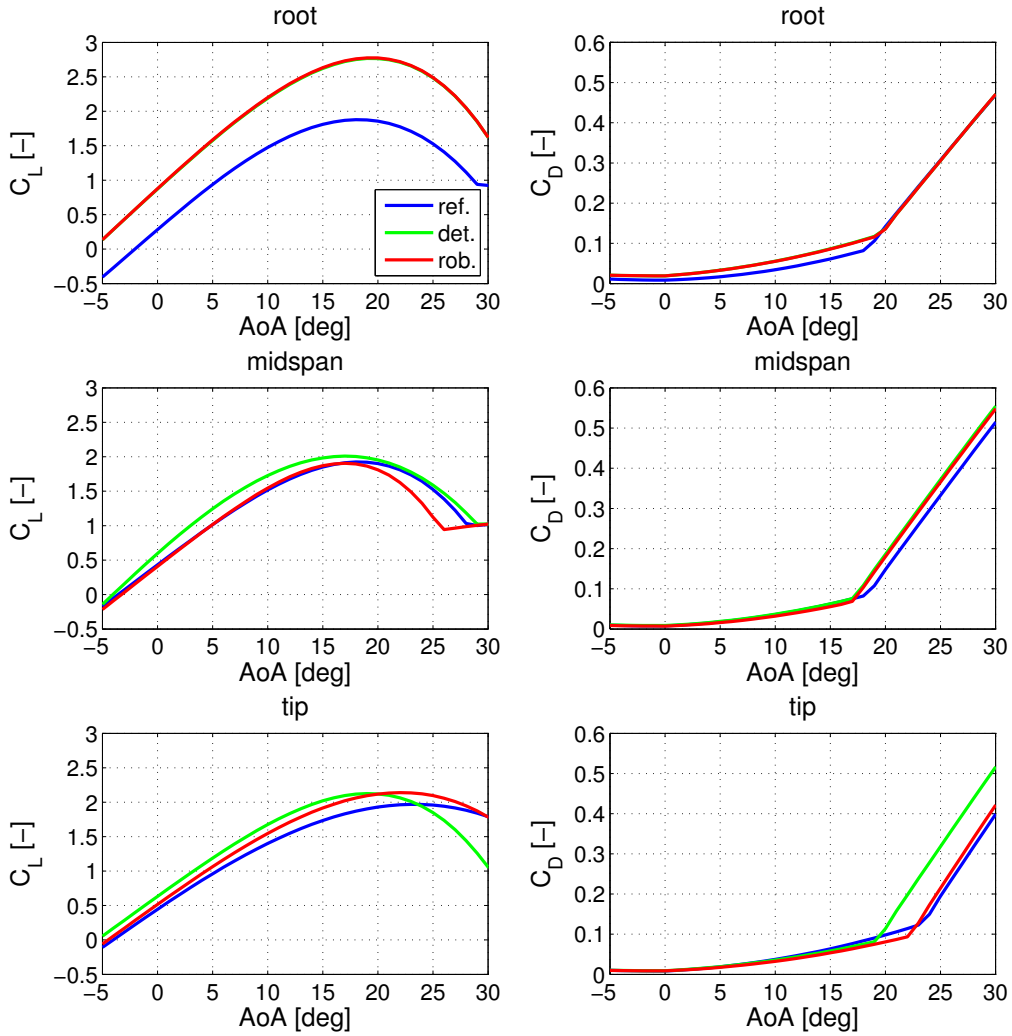

Fig. 6.4 Comparison of lift and drag coefficients of the reference, deterministic and robust designs' base airfoils, for an indicative Reynolds number of $12 \cdot 10^6$.

a reduction of 6.95% of the thickness of the internal structure with respect to the reference turbine.

The higher mean of AEP of the deterministic and robust turbines over the reference one is determined by a higher power production of the former turbines in regions 1½, 2 and 2½, as highlighted above. This improvement is due to the reported alterations of the outer blade shapes, and, in the case of the robust turbine, a higher rotor speed. All these alterations have conflicting effects on the net power production, and a discussion on their interactions in regions 1½, 2 and 2½ for both the deterministic and robust turbines is provided below.

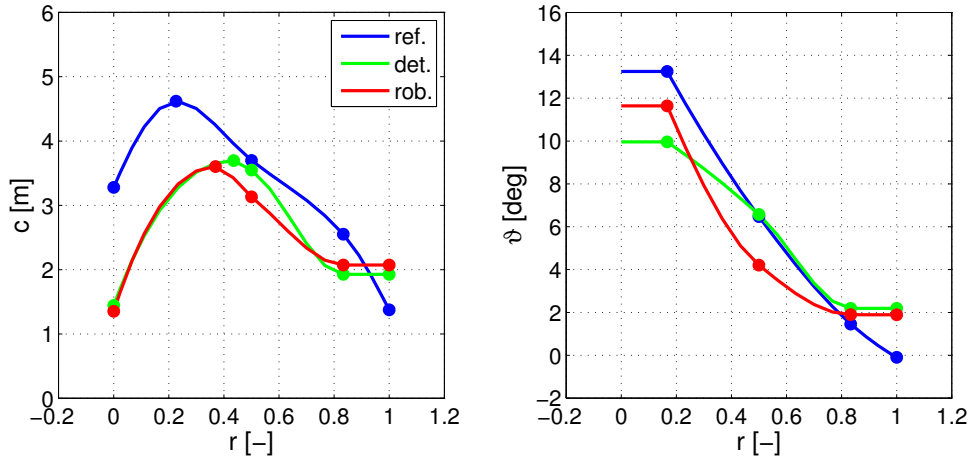

Fig. 6.5 Comparison of chord and twist distributions (left and right subplots, respectively) of the reference, deterministic and robust designs.

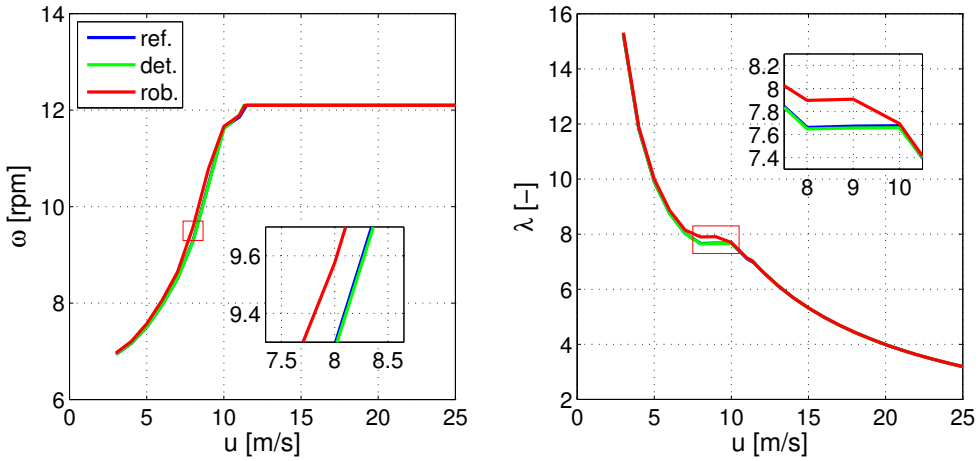

Fig. 6.6 Comparison of rotor speed and tip-speed ratio against wind speed (left and right subplots, respectively) of the reference, deterministic and robust designs.

At the inboard sections, the twist reduction of the deterministic design visible in the top right subplot of Fig. 6.5 yields an increment of the aerodynamic load, as one can see in the right subplot of Fig. 6.8. This is a consequence of the expected higher AoA, and also the higher lift coefficient curves at the inboard blade sections. At a wind speed of 9.0 m/s, the

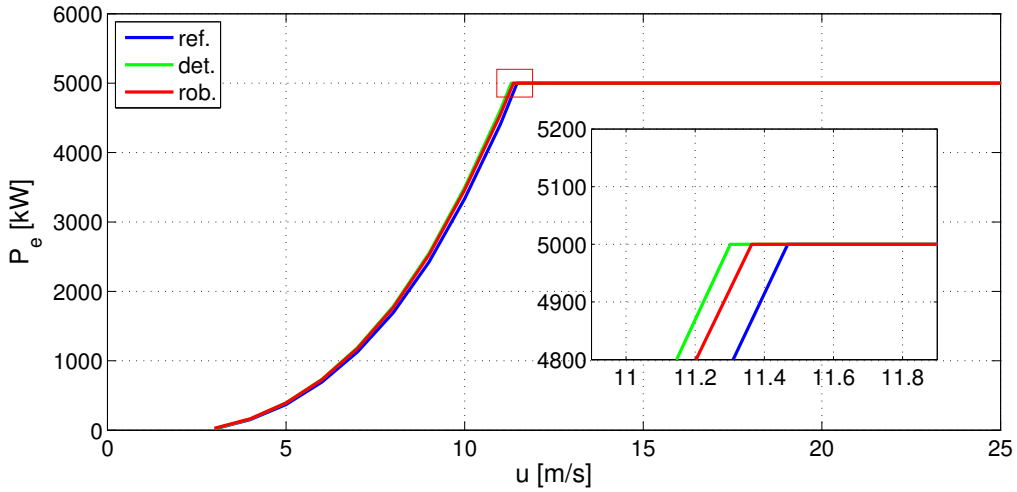

Fig. 6.7 Electrical power as a function of wind speed of the reference, deterministic and robust designs.

	ref.	det.	rob.
K [N · m/s^2]	2.13 ($\lambda = 7.67$)	2.26 ($\lambda = 7.65$)	2.03 ($\lambda = 7.90$)
s	0.964	0.897	0.832

Table 6.6 Torque control parameter with resulting tip-speed ratio in region 2 in parentheses, and thickness parameter of the reference, deterministic and robust designs.

AoA at the root airfoil of the deterministic turbine increases by about 2.5 deg, slightly less than 3 deg, which is the twist reduction at this radius. Moreover, the chords of the inboard sections of the deterministic design are smaller than those of the reference turbine. As a consequence, the increment of the aerodynamic forces due to higher AoA and the higher lift coefficient curve is partly compensated by the reduction of these forces caused by a smaller blade planform. As a consequence, the tangential force, and thus the aerodynamic torque, of the inboard sections of the deterministic blade design is significantly higher than that of the reference blade design. At 40% blade length the tangential force of the former blade achieves increments of up to 10% over the latter blade design. The higher power extracted by the inboard sections of the deterministic design is thus a result of the higher torque.

Like at the inboard sections, the deterministic blade is more heavily loaded than the reference one at the outboard sections. This is a consequence of a higher lift coefficient distribution and larger chords. The increase of the aerodynamic loads due to higher lift coefficient distribution and larger chords is partially compensated by the lower AoA, which is a consequence of the twist increase at near-tip sections shown in the right subplot of Fig. 6.5.

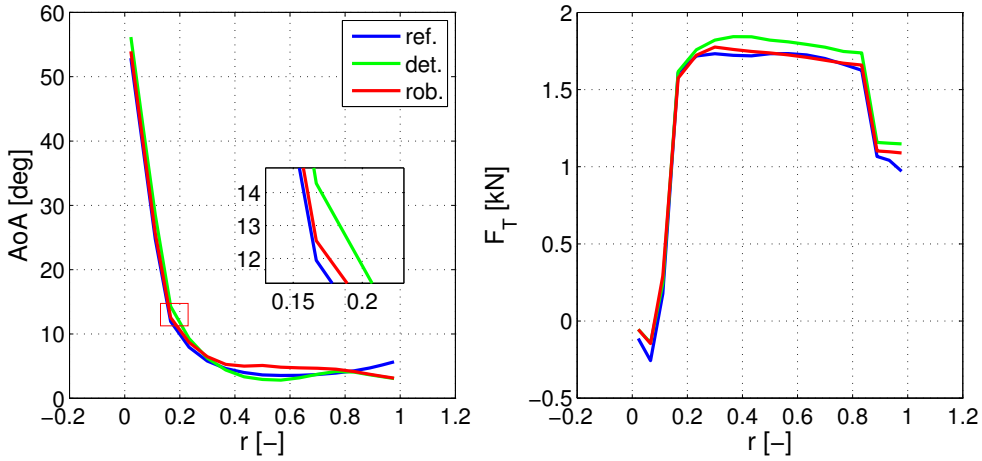

Fig. 6.8 Comparison of the angle of attack and tangential force distributions along the blade span (left and right subplots, respectively) of the reference, deterministic and robust designs, for a wind speed of 9.0 m/s.

At a wind speed of 9.0 m/s, the AoA at the near-tip airfoils of the robust turbine decreases by about 2.6 deg, slightly more than the 2.2 deg twist increase at the blade tip. As a result, at the outboard sections, the deterministic turbine extracts more power than the reference one due to greater tangential forces, and thus a higher aerodynamic torque.

At the inboard sections, the twist reduction of the robust design shown in the right subplot of Fig. 6.5 yields an increment of the aerodynamic load, as one can see in the right subplot of Fig. 6.8. This is a consequence of the expected higher AoA, and also the higher lift coefficient curves of the inboard blade sections. However, the AoA increment due to the lower twist is reduced by the increment of about 3% of the rotational speed. Due to this, at a wind speed of 9.0 m/s, the AoA at the root airfoil of the robust turbine increases by about 1 deg (see the left subplot of Fig. 6.8), and not by more than 2 degrees, which is the twist reduction at this radius. Moreover, the chords of the inboard sections of the robust design are smaller than those of the reference turbine. As a consequence, the increment of the aerodynamic forces due to slightly higher AoA and the higher lift coefficient curve is partly compensated by the reduction of these forces caused by a smaller blade planform. As a consequence, the tangential force, and thus the aerodynamic torque, of the inboard sections of the robust blade design is noticeably higher than that of the reference blade design. At 30% blade length the tangential force of the former blade achieves increments of up to 2.5%

over the latter blade design. The higher power extracted by the inboard sections of the robust design is thus a result of both the higher torque and the higher rotational speed.

At the outboard sections, the twist increment of the robust design yields a reduction of the aerodynamic load. This is a consequence of the expected lower AoA. The AoA at high blade radii is further reduced by the higher rotational speed of the robust rotor. Therefore, at a wind speed of 9.0 m/s, the AoA at the near-tip airfoils of the robust turbine decreases by about 2.5 deg, slightly more than the 1.9 deg twist increase at the blade tip visible in the right subplot of Fig. 6.5. As for the power production of the outboard sections, it is observed that the chords of the outboard sections of the robust design are larger than those of the reference turbine. In addition, the lift coefficient distribution along the outboard part of the robust blade is higher than that of the reference design. As a consequence, the reduction of the aerodynamic forces due to lower AoA is compensated by the increment of these forces caused by a larger blade planform and higher lift coefficient. Thus, the tangential force and the aerodynamic torque of the outboard sections of the two blade designs are fairly similar, and the outboard sections of the robust blade design produce more power due primarily to the higher rotational speed.

Figures 6.9, 6.10 and 6.11 compare the blade displacements and the applied forces of the reference, deterministic and robust blade designs, respectively, at the 3 o'clock azimuthal position for a wind speed of 12.0 m/s and a rotor speed of 12.1 rpm. This figure highlights *a*) the lighter weight of the inboard part of the deterministic and robust designs, and *b*) the larger deflections of the deterministic and robust designs resulting from the larger normal components of the aerodynamic force, and lower stiffness with respect to the reference blade.

Figures 6.12, 6.13 and 6.14 report the laminate normal stresses acting on the reference, deterministic and robust blades, respectively, at the 3 o'clock azimuthal position for a wind speed of 12.0 m/s and a rotor speed of 12.1 rpm. It is noted that the maximum tensile stress occurs on the blade suction side close to its root for all configurations, and that the maximum tensile stress of the deterministic and robust designs is higher than that of the reference blade, as previously indicated. This points to better utilization of the material strength, since the maximum stress of the deterministic and robust blade designs is still lower than the maximum value enforced by the structural constraints.

Figures 6.15, 6.16 and 6.17 report the buckling criteria on the reference, deterministic and robust blades, respectively, at the 3 o'clock azimuthal position for a wind speed of 12.0 m/s and a rotor speed of 12.1 rpm. These figures highlight that, for all the three blades, the maximum buckling stress concentration acts over the aft part of the top surface, at around half-span of the blade.

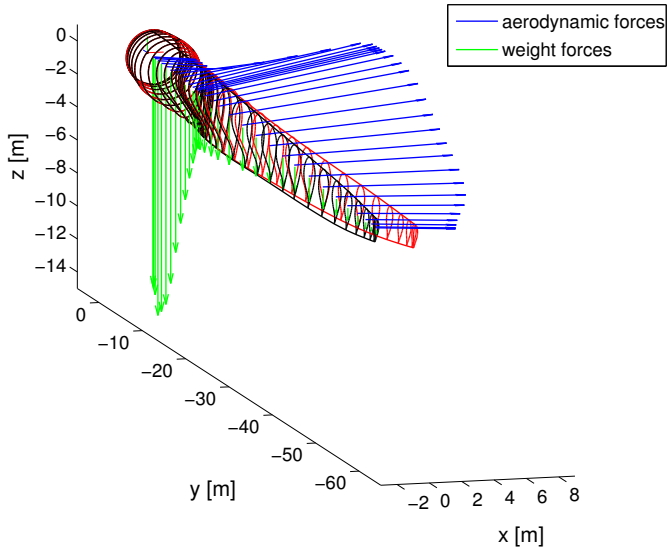

Fig. 6.9 Displacement and applied forces of the reference blade in the 3 o'clock azimuth position, for a wind speed of 12.0 m/s and a rotor speed of 12.1 rpm.

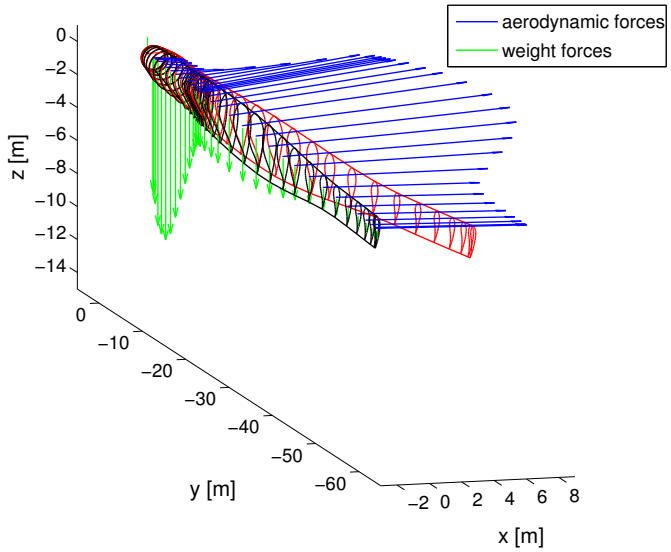

Fig. 6.10 Displacement and applied forces of the deterministic blade in the 3 o'clock azimuth position, for a wind speed of 12.0 m/s and a rotor speed of 12.1 rpm.

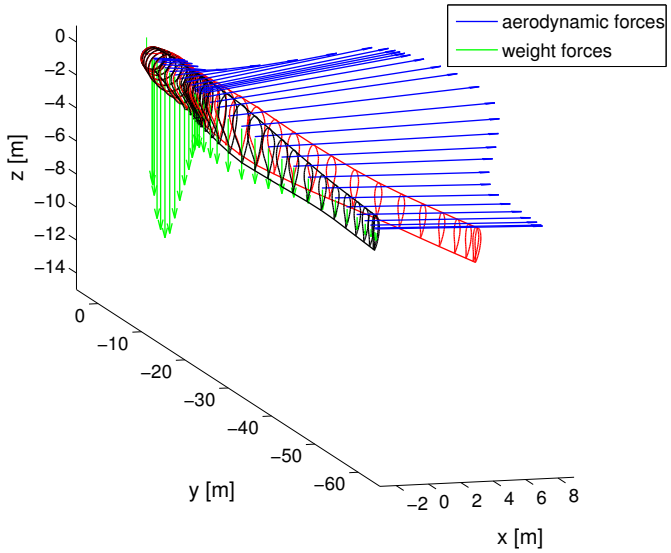

Fig. 6.11 Displacement and applied forces of the robust blade in the 3 o'clock azimuth position, for a wind speed of 12.0 m/s and a rotor speed of 12.1 rpm.

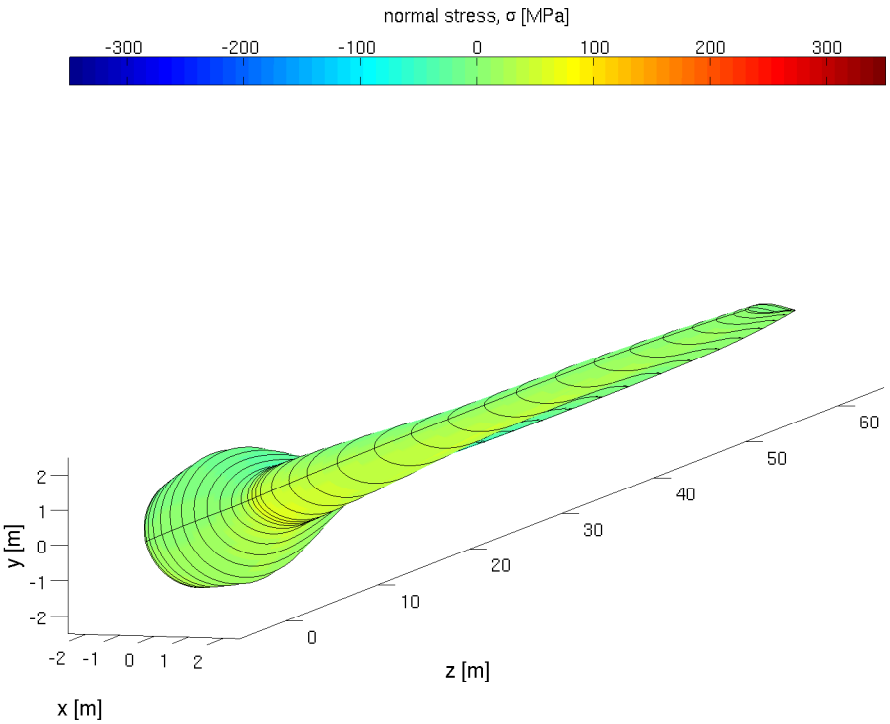

Fig. 6.12 Laminate normal stress of the reference blade in the 3 o'clock azimuth position, for a wind speed of 12.0 m/s and a rotor speed of 12.1 rpm.

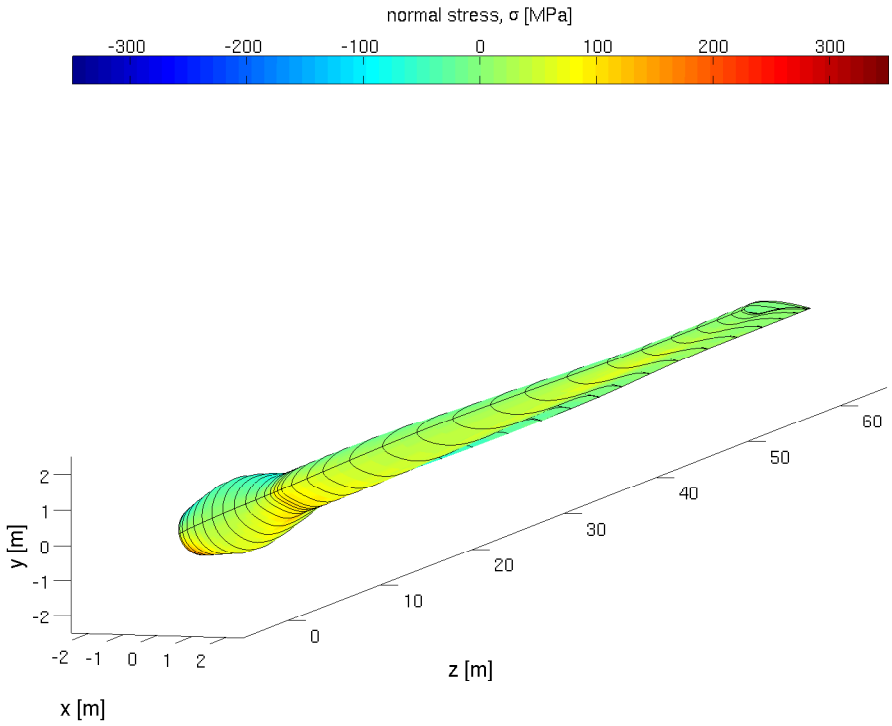

Fig. 6.13 Laminate normal stress of the deterministic blade in the 3 o'clock azimuth position, for a wind speed of 12.0 m/s and a rotor speed of 12.1 rpm.

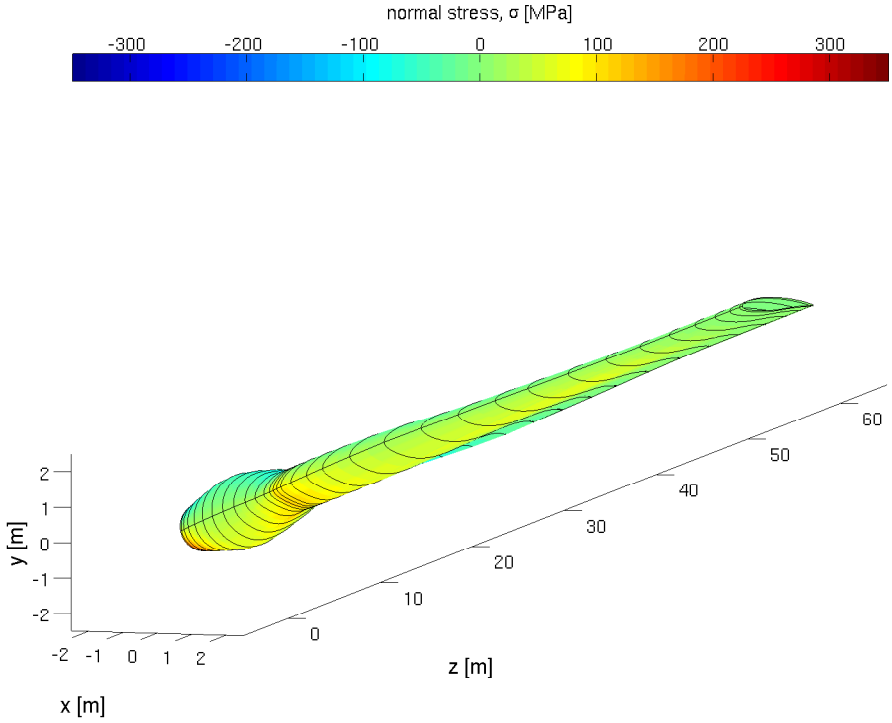

Fig. 6.14 Laminate normal stress of the robust blade in the 3 o'clock azimuth position, for a wind speed of 12.0 m/s and a rotor speed of 12.1 rpm.

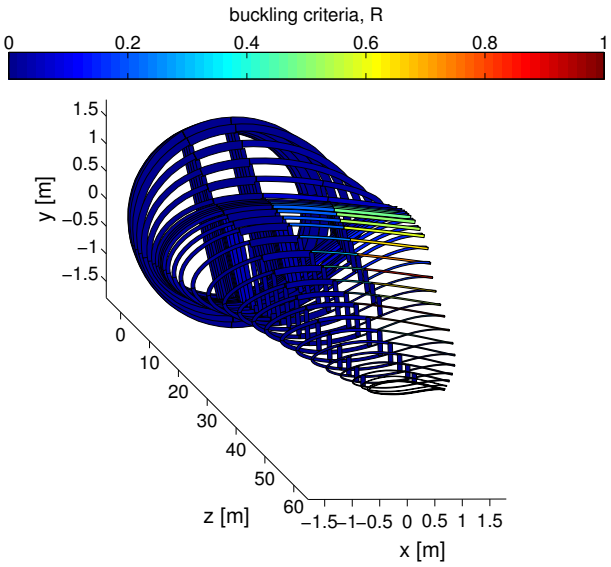

Fig. 6.15 Buckling criteria of the reference blade in the 3 o'clock azimuth position, for a wind speed of 12.0 m/s and a rotor speed of 12.1 rpm.

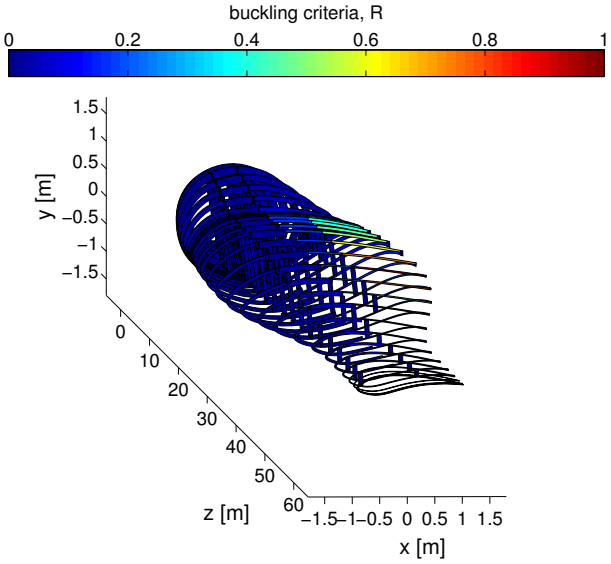

Fig. 6.16 Buckling criteria of the deterministic blade in the 3 o'clock azimuth position, for a wind speed of 12.0 m/s and a rotor speed of 12.1 rpm.

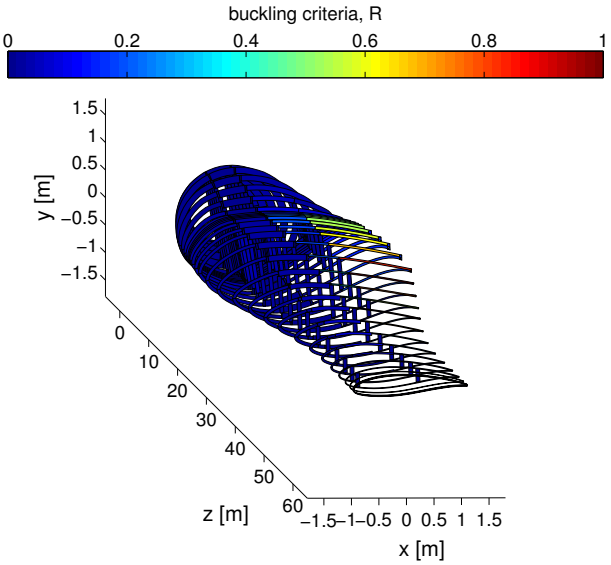

Fig. 6.17 Buckling criteria of the robust blade in the 3 o'clock azimuth position, for a wind speed of 12.0 m/s and a rotor speed of 12.1 rpm.

Chapter 7

Conclusions and suggestions for further work

7.1 Summary and concluding remarks

A novel integrated computational framework for the multidisciplinary and robust design optimization of HAWTs has been developed, assessed and demonstrated by performing the aeroservoelastic design optimization of a multi-megawatt HAWT under environmental uncertainty.

7.1.1 Conclusions on the development of the design system

The multidisciplinary and robust design optimization system has been presented, highlighting the interconnection and main characteristics of its constituent modules. An overview of the topics which are fundamental to understanding the aeroservoelastic behavior of HAWTs, uncertainty propagation and mathematical optimization has been also provided. The key features of the developed framework include:

- the integration of a method for uncertainty propagation to account for uncertainty in the design optimization process, and
- the concurrent optimization of the blade airfoils, chord and twist radial distributions, rotor speed and internal structural layup, and
- the enforcement of a comprehensive set of aerostructural constraints to ensure the blade structural integrity during the course of the optimization.

The main element of novelty associated with the presented HAWT MDO system is that it simultaneously includes uncertainty propagation, the optimization of the blade airfoil shapes within the aeroservoelastic optimization of the rotor, and the enforcement of a comprehensive set of aerostructural constraints. Airfoil optimization has been made possible by developing a suitable parametrization based on a composite Bézier curve, enabling high flexibility, yet keeping a low number of degrees of freedom. Another important feature of the presented system is that it is made up of integrated modules. In principle, this allows one to replace one or more current modules (for instance with higher-fidelity ones) without the need to modify significantly the rest of the system.

7.1.2 Conclusions on the application of the design system

The developed computational framework has been successfully used to optimize the design of a HAWT rotor subject to the environmental uncertainty associated with the mean value of the wind speed frequency distribution. The probabilistic design exercise has involved minimizing the expected value and standard deviation of LCOE by optimizing the turbine's blade external geometry, rotor speed and internal structural layup. The main motivation for analyzing this scenario has been to demonstrate the effectiveness of the developed probabilistic design system taking into account a realistic problem.

The achieved robust optimum turbine design has been found to achieve a reduction of about 7.7% of the expectation of LCOE, and a reduction of about 12.5% of the standard deviation of this objective function with respect to the initial baseline reference turbine. This improvement has been made possible primarily by both increasing the lift-to-drag ratio of the rotor airfoils and decreasing the rotor blade weight, still satisfying the aerostructural constraints.

The better airfoil aerodynamic performance of the robust airfoils with respect to the reference ones are due to greater airfoil cambers. It has also been shown that structural considerations have driven the optimization of the airfoils. In particular, the robust airfoils have a lower mean radius of curvature over the aft portion of the suction side with respect to the reference airfoils. This results in an increase of the buckling strength of the blade laminates at a location characterized by a high buckling stress concentration.

The probabilistically designed turbine has also achieved more favorable probabilistic performance than those of a turbine designed deterministically, with a reduction of about 0.6% of the expectation of LCOE, and a reduction of about 0.6% of the standard deviation of LCOE. These results highlight that taking into account the environmental uncertainty in the optimization process, has enabled us to achieve a robust design with lower expectation and

sensitivity of LCOE to the mean value of the wind speed distribution with respect to those of a deterministically designed turbine.

The obtained optimal solutions may require further verifications due to possible inaccuracy of the low-fidelity aerodynamic module XFOIL for stall and post-stall airfoil performance analysis, and also the high level of empiricism of the 3D correction model used by the BEM analysis. The main objective of the probabilistic turbine design optimization exercise presented herein, however, has been to highlight the potential of robust fully integrated MDO of improving HAWT design technologies, rather than proposing a ready-for-installation design, and this objective has been accomplished.

7.2 Future work

On the methodology front, future improvements of the developed design framework include the incorporation of higher-fidelity analysis modules, such as transitional NS CFD for stall and post-stall airfoil aerodynamics, and possibly a full 3D finite element stress analysis code for rotor structural analysis. Another planned extension of the current design system encompasses the integration of a module for the tower structural analysis and design. This will allow one to extend the design search by including turbine rated power and rotor diameter as design variables.

On the application side, planned and partly already ongoing work includes using the developed methodology to carry out the design optimization of multi-megawatt wind turbine rotors considering other sources of uncertainty, such as those associated with rotor manufacturing, assembly and blade internal structural layup errors.

References

[1] Global Wind Energy Council. Global Wind Report 2013 - Annual market update. Technical report, GWEC, Brussels, Belgium, 2013.

[2] P. Brøndsted. Introduction. In P. Brøndsted and R. P. L. Nijssen, editors, *Advances in wind turbine blade design and materials*, volume 47 of *Energy*. Woodhead Publishing Limited, 2013. ISBN 978-0-85709-426-1.

[3] T. Ashuri. *Beyond Classical Upscaling: Integrated Aeroservoelastic Design and Optimization of Large Offshore Wind Turbines*. PhD thesis, TU Delft, 2012.

[4] G. Sieros, P. Chaviaropoulos, J. D. Sørensen, B. H. Bulder, and P. Jamieson. Upscaling wind turbines: theoretical and practical aspects and their impact on the cost of energy. *Wind Energy*, 15(1):3–17, 2012.

[5] P. Jamieson. *Innovation in Wind Turbine Design*. Wiley, 2011.

[6] J. R. R. A. Martins and A. B. Lambe. Multidisciplinary design optimization: A survey of architectures. *AIAA Journal*, 51(9):2049–2075, 2013.

[7] P. Fuglsang and H. A. Madsen. Optimization method for wind turbine rotors. *Journal of Wind Engineering and Industrial Aerodynamics*, 80(1–2):191–206, 1999.

[8] E. Benini and A. Toffolo. Optimal design of horizontal-axis wind turbines using blade-element theory and evolutionary computation. *Journal of Solar Energy Engineering*, 124:357–363, 2002.

[9] Juan Méndez and D. Greiner. Wind blade chord and twist angle optimization by using genetic algorithms. In *Fifth International Conference on Engineering Computational Technology*, Las Palmas de Gran Canaria, Spain, 2006.

[10] G. Kenway and J. R. R. A. Martins. Aerostructural shape optimization of wind turbine blades considering site-specific winds. In *12th AIAA/ISSMO Multidisciplinary Analysis and Optimization Conference, MAO*, Victoria, British Columbia, Canada, 2008.

[11] W. Xudong, W. Z. Shen, W. J. Zhu, J. N. Sørensen, and C. Jin. Shape optimization of wind turbine blades. *Wind Energy*, 12(8):781–803, 2009.

[12] G. Petrone, C. de Nicola, D. Quagliarella, J. Witteveen, and G. Iaccarino. Wind turbine optimization under uncertainty with high performance computing. In *29th AIAA Applied Aerodynamics Conference 2011*, Honolulu, Hawaii, USA, 2011.

[13] J. Jeong, K. Park, S. Jun, K. Song, and D. Lee. Design optimization of a wind turbine blade to reduce the fluctuating unsteady aerodynamic load in turbulent wind. *Journal of Mechanical Science and Technology*, 3(26):827–838, 2012.

[14] C. L. Bottasso, F. Campagnolo, and A. Croce. Multi-disciplinary constrained optimization of wind turbines. *Multibody System Dynamics*, 27(1):21–53, 2012.

[15] R. W. Vesel and J. J. McNamara. Performance enhancement and load reduction of a 5 MW wind turbine blade. *Renewable Energy*, 66:391–401, 2014.

[16] T. Ashuri, M. B. Zaaijer, J. R. R. A. Martins, G. J. W. van Bussel, and G. A. M. van Kuik. Multidisciplinary design optimization of offshore wind turbines for minimum levelized cost of energy. *Renewable Energy*, 68:893–905, 2014.

[17] S. A. Ning, R. Damiani, and P. J. Moriarty. Objectives and constraints for wind turbine optimization. *Journal of Solar Energy Engineering, Transactions of the ASME*, 136(4), 2014.

[18] C. L. Bottasso, A. Croce, L. Sartori, and F. Grasso. Free-form design of rotor blades. *Journal of Physics: Conference Series*, 524(1), 2014.

[19] M. Caboni, E. Minisci, and M. S. Campobasso. Robust aerodynamic design optimization of horizontal axis wind turbine rotors. In D. Greiner, B. Galván, J. Periaux, N. Gauger, K. Giannakoglou, and G. Winter, editors, *Advances in Evolutionary and Deterministic Methods for Design, Optimization and Control in Engineering and Sciences*, volume 36 of *Computational Methods in Applied Sciences*. Springer, 2014. ISBN 978-3-319-11540-5.

[20] M. S. Campobasso, E. Minisci, and M. Caboni. Aerodynamic design optimization of wind turbine rotors under geometric uncertainty. *Wind Energy*, 2014. DOI: 10.1002/we.1820.

[21] P. Fuglsang and K. Thomsen. Site-specific design optimization of 1.5–2.0 MW wind turbines. *Journal of Solar Energy Engineering, Transactions of the ASME*, 123(4):296–303, 2001.

[22] P. Fuglsang, C. Bak, J. G. Schepers, B. Bulder, T. T. Cockerill, P. Claiden, A. Olesen, and R. van Rossen. Site-specific design optimization of wind turbines. *Wind Energy*, 5(4):261–279, 2002.

[23] T. Diveux, P. Sebastian, D. Bernard, J. R. Puiggali, and J. Y. Grandidier. Horizontal axis wind turbine systems: optimization using genetic algorithms. *Wind Energy*, 4(4):151–171, 2001.

[24] K. Lee, W. Joo, K. Kim, D. Lee, K. Lee, and J. Park. Numerical Optimization using Improvement of the Design Space Feasibility for Korean Offshore Horizontal Axis Wind Turbine Blade. In *EWEC 2007*, Milan, Italy, 2007.

[25] K. Maki, R. Sbragio, and N. Vlahopoulos. System design of a wind turbine using a multi-level optimization approach. *Renewable Energy*, 43:101–110, 2012.

[26] M. Jureczko, M. Pawlak, and A. Mężyk. Optimisation of wind turbine blades. *Journal of Materials Processing Technology*, 167:463–471, 2005.

[27] E. Lund and J. Stegmann. On Structural Optimization of Composite Shell Structures Using a Discrete Constitutive Parametrization. *Renewable Energy*, 8:109–124, 2005.

[28] International Standard. International Electrotechnical Commission, 2009-02. IEC 61400-3 Edition 1.0.

[29] G. J. Park, T. H. Lee, K. H. Lee, and K. H. Hwang. Robust design: An overview. *AIAA Journal*, 44(1), 2006.

[30] INVESTOPEDIA. Variance. See also URL http://www.investopedia.com/terms/v/variance.asp.

[31] G. Iaccarino. Quantification of Uncertainty in Flow Simulations Using Probabilistic Methods. Technical report, Stanford University, Stanford, California, USA, 2008. VKI Lecture Series.

[32] M. Padulo, M.S. Campobasso, and M.D. Guenov. A Novel Uncertainty Propagation Method for Robust Aerodynamic Design. *AIAA Journal*, 49(3):530–543, 2011.

[33] D. T. Griffith and T. D. Ashwill. The Sandia 100-meter All-glass Baseline Wind Turbine Blade: SNL100-00. Technical report, Sandia National Laboratories, Albuquerque, New Mexico, USA, 2011. SAND2011-3779.

[34] B. R. Resor. Definition of a 5MW/61.5m Wind Turbine Blade Reference Model. Technical report, Sandia National Laboratories, Albuquerque, New Mexico, USA, 2013. SAND2013-2569.

[35] M. H. Straathof. *Shape Parameterization in Aircraft Design: A Novel Method, Based on B-Splines*. PhD thesis, TU Delft, 2012.

[36] J. Jonkman, S. Butterfield, W. Musial, and G. Scott. Definition of a 5-MW Reference Wind Turbine for Offshore System Development. Technical report, National Renewable Energy Laboratory, Golden, Colorado, USA, 2009. NREL/TP-500-38060.

[37] S. Øye. FLEX4 – Simulation of Wind Turbine Dynamics. In *28th IEA Meeting of Experts "State of the Art of Aeroelastic Codes for Wind Turbine Calculations"*, Lyngby, Denmark, 1996.

[38] E. A. Bossanyi. GH-Bladed User Manual. Technical report, Garrad Hassan and Partners Limited, Bristol, UK, 2004. Issue 14.

[39] C. Lindenburg and J. G. Schepers. Phatas-IV Aero-elastic Modelling, Release. Technical report, ECN, Petten, Netherlands, 2000. ECN-CX–00-027.

[40] J. M. Jonkman and M. L. Buhl. FAST User's Guide. Technical report, National Renewable Energy Laboratory, Golden, Colorado, USA, 2005. NREL/EL-500-29798.

[41] T. J. Larsen, H. A. Madsen, A. M. Hansen, and K. Thomsen. Investigations of stability effects of an offshore wind turbine using the new aeroelastic code HAWC2. In *Copenhagen Offshore Wind 2005*, Copenhagen, Denmark, 2005.

[42] J. Manwell, J. McGowan, and A. Rogers. *Wind Energy Explained. Theory, Design and Application*. John Wiley and Sons Ltd., 2002.

[43] J. D. Anderson. *Computational Fluid Dynamics*. McGraw-Hill Higher Education, 1995. Sixth Edition.

[44] D. J. Laino. AeroDyn: Aerodynamics analysis routines for horizontal-axis wind-turbine dynamics analyses. See also URL https://nwtc.nrel.gov/AeroDyn.

[45] S. A. Ning. CCBlade. See also URL https://nwtc.nrel.gov/CCBlade.

[46] M. S. Campobasso and M. H. Baba-Ahmadi. Analysis of Unsteady Flows Past Horizontal Axis Wind Turbine Airfoils Based on Harmonic Balance Compressible Navier-Stokes Equations With Low-Speed Preconditioning. *Journal of Turbomachinery*, 6(134), 2012.

[47] Numeca. Fine™/Turbo. See also URL http://www.numeca.com/en/products/finetmturbo.

[48] A. Suzuki and A. Hansen. Generalized dynamic wake model for YawDyn. In *AIAA-99–0041, 37th Aerospace Sciences Meeting and Exhibit*, Reno, Nevada, USA, 1999.

[49] H. Glauert. *The analysis of experimental results in the windmill brake and vortex ring states of an airscrew*. H.M. Stationery Office, 1926.

[50] M. L. Buhl. A New Empirical Relationship between Thrust Coefficient and Induction Factor for the Turbulent Windmill State. Technical report, National Renewable Energy Laboratory, Golden, Colorado, USA, 2005. NREL/TP-500-36834.

[51] H. Glauert. *A General Theory of the Autogyro*. H.M. Stationery Office, 1928.

[52] C. Bak, A. Madsen, and J. Johansen. *Influence from blade-tower interaction on fatigue loads and dynamics (poster)*, pages 394–397. WIP Renewable Energies, 2001.

[53] B. D. Hibbs. HAWT Performance With Dynamic Stall. Technical report, Solar Energy Research Institute, Golden, Colorado, USA, 1986. STR-2732.

[54] T. Burton, N. Jenkins, D. Sharpe, and E. Bossanyi. *Wind Energy Handbook*. John Wiley and Sons Ltd., 2002.

[55] R. E. Gormont. A Mathematical Model of Unsteady Aerodynamics and Radial Flow for Application to Helicopter Rotors. Technical report, US Army Air Mobility Research and Development Laboratory, Philadelphia, Pennsylvania, USA, 1973. AD-767240.

[56] A. Björck, M. Mert, and H. A. Madsen. Optimal parameters for the FFA-Beddoes dynamic stall model. In *1999 European Wind Energy Conference*, Nice, France, 1999.

[57] H. Snel and J. G. Schepers. Engineering models for dynamic inflow phenomena. In *1991 European Wind Energy Conference*, Amsterdam, Netherlands, 1991.

[58] H. Snel and J. G. Schepers. Investigation and modelling of dynamic inflow effects. In *1993 European Wind Energy Conference*, Lübeck, Germany, 1993.

[59] D. M. Pitt and D. A. Peters. Theoretical predictions of dynamic inflow derivatives. *Vertica*, 1(5):21–34, 1981.

[60] ANSYS Inc. ANSYS. See also URL http://www.ansys.com/.

[61] Dassault Systèmes. Abaqus Unified FEA. http://www.3ds.com/products-services/simulia/products/abaqus/.

[62] Dassault Systèmes. SolidWorks. http://www.solidworks.co.uk/.

[63] Sandia National Laboratories. NuMAD. http://energy.sandia.gov/energy/renewable-energy/wind-power/rotor-innovation/numerical-manufacturing-and-design-tool-numad/.

[64] R. C. Juvinall and K. M. Marshek. *Fundamental of Machine Component Design*. John Wiley and Sons Ltd., 2012.

[65] G. Bir. Pre-Processor for Computing Composite Blade Properties. See also URL https://nwtc.nrel.gov/PreComp.

[66] M. E. Tuttle. *Structural Analysis of Polymeric Composite Materials*. CRC Press, 2012. Second Edition.

[67] R. M. Jones. *Mechanics of Composite Materials*. McGraw-Hill, 1975.

[68] O. A. Bauchau and J. I. Craig. *Structural Analysis: With Applications to Aerospace Structures*. Springer, 2009.

[69] D. C. Sale. Co-Blade: Software for Analysis and Design of Composite Blades. See also URL https://code.google.com/p/co-blade/.

[70] R. M. Rivello. *Theory and Analysis of Flight Structures*. McGraw-Hill, 1969.

[71] D. H. Allen and W. E. Haisler. *Introduction to Aerospace Structural Analysis*. John Wiley and Sons Ltd., 1985.

[72] D. J. Peery and J. J. Azar. *Aircraft Structures*. McGraw-Hill, 1982. Second Edition.

[73] W. Young and R. Budynas. *Roark's Formulas for Stress and Strain*. McGraw-Hill, 2001. Seventh Edition.

[74] T. Ashuri, M. Zaaijer, G. van Bussel, and G. van Kuik. An analytical model to extract wind turbine blade structural properties for optimization and up-scaling studies. In *The Science of Making Torque from Wind*, Crete, Greece, 2010.

[75] G. Bir. BModes: Software for Computing Rotating Blade Coupled Modes. See also URL https://nwtc.nrel.gov/BModes.

[76] G. Hayman. MLife: A MATLAB-based Estimator of Fatigue Life. See also URL https://nwtc.nrel.gov/MLife.

[77] Astm international. Standard Practices for Cycle Counting in Fatigue Analysis, 2011. ASTM E1049 - 85(2011)e1.

[78] M. A. Miner. Cumulative Damage in Fatigue. *Journal of Applied Mechanics*, 12(1):A159–A164, 1945.

[79] M. Buhl. IECWind: A program to create IEC hub-height wind files for InflowWind/AeroDyn-based simulators. See also URL https://nwtc.nrel.gov/IECWind.

[80] N. Kelley and B. Jonkman. TurbSim: A stochastic, full-field, turbulence simulator primarily for use with InflowWind/AeroDyn-based simulation tools. See also URL https://nwtc.nrel.gov/TurbSim.

[81] J. L. Tangler and D. M. Somers. NREL Airfoil Families for HAWTs. Technical report, National Renewable Energy Laboratory, Golden, Colorado, USA, 1995. NREL/TP-442-7109.

[82] W.A. Timmer and R.P.J.O.M. van Rooij. Summary of the Delft University Wind Turbine Dedicated Airfoils. *Journal of Solar Energy Engineering, Transactions of the ASME*, 125:488–496, 2003.

[83] N.N. Sørensen. CFD Modelling of Laminar-Turbulent Transition for Airfoils and Rotors Using the $\gamma - \tilde{Re}_\theta$ Model. *Wind Energy*, 12:715–733, 2009.

[84] C. Bak. Aerodynamic design of wind turbine rotors. In P. Brøndsted and R. P. L. Nijssen, editors, *Advances in wind turbine blade design and materials*, volume 47 of *Energy*. Woodhead Publishing Limited, 2013. ISBN 978-0-85709-426-1.

[85] A.C. Aranake, V.K. Lakshminarayan, and K. Duraysami. Computational analysis of shrouded wind turbine configurations using a 3-dimensional RANS solver. *Renewable Energy*, 75:818–832, 2015.

[86] J. Tangler and J. D. Kocurek. Wind Turbine Post-Stall Airfoil Performance Characteristics Guidelines for Blade-Element Momentum Methods. Technical report, National Renewable Energy Laboratory, Golden, Colorado, USA, 2004. NREL/CP-500-36900.

[87] S. J. Schreck, N. N. Sørensen, and M. C. Robinson. Aerodynamic Structures and Processes in Rotationally Augmented Flow Fields. *Wind Energy*, 4(10):159–178, 2001.

[88] S. Schreck. Wind Turbine Aerodynamics Part B: Turbine Blade Flow Fields. In D. A. Spera, editor, *Wind Turbine Tecnology*. ASME PRESS, 2009. Second Edition.

[89] H. Snel, R. Houwink, G. J. W. van Bussel, and A. Bruining. Sectional prediction of 3D effects for stalled flow on rotating blades and comparison with measurements. In *European Community Wind Energy Conference*, Lübeck-Travemünde,Germany, 1993.

[90] Z. Du and M. S. Selig. A 3-D stall-delay model for horizontal axis wind turbine performance prediction. In *AIAA-98-0021, 36th AIAA Aerospace Sciences. Meeting and Exhibit, 1998 ASME Wind Energy Symposium*, Reno, Nevada, USA, 1998.

[91] P. K. Chaviaropoulos and M. O. L. Hansen. Investigating three-dimensional and rotational effects on wind turbine blades by means of a quasi-3D Navier Stokes solver. *Journal of Fluids Engineering*, (122):330–336, 2000.

[92] C. Lindenburg. Modelling of rotational augmentation based on engineering considerations and measurements. In *European Wind Energy Conference*, London, UK, 2004.

[93] C. Bak, J. Johansen, and P. B. Andersen. Three-dimensional corrections of airfoil characteristics based on pressure distributions. In *European Wind Energy Conference Exhibition (EWEC)*, Athens, Greece, 2006.

[94] A. J. Eggers, K. Chaney, and R. Digumarthi. An Assessment of Approximate Modeling of Aerodynamic Loads on the UAE Rotor. In *AIAA-2003-0868, 41st Aerospace Sciences Meeting and Exhibit*, Reno, Nevada, USA, 2003.

[95] W. A. Timmer and C. Bak. Aerodynamic characteristics of wind turbine blade airfoils. In P. Brøndsted and R. P. L. Nijssen, editors, *Advances in wind turbine blade design and materials*, volume 47 of *Energy*. Woodhead Publishing Limited, 2013. ISBN 978-0-85709-426-1.

[96] L. A. Viterna and R. D. Corrigan. Fixed Pitch Rotor Performance of Large Horizontal Axis Wind Turbines. Technical report, NASA Lewis Research Center, Cleveland, Ohio, USA, 1981. N83 19233.

[97] E. M. Jacobs and I. H. Abbot. The NACA Variable-Density Wind Tunnel. Technical report, NASA Langley Research Center, Hampton, Virginia, USA, 1932. NACA TR 416.

[98] D. Spera. Models of Lift and Drag Coefficients of Stalled and Unstalled Airfoils in Wind Turbines and Wind Tunnels. Technical report, National Aeronautics and Space Administration, Cleveland, Ohio, USA, 2008. NASA/CR—2008-215434.

[99] M. M. Hand, D. A. Simms, L.J. Fingersh, D. W. Jager, J. R. Cotrell, S. Schreck, and S. M. Larwood. Unsteady Aerodynamics Experiment Phase VI: Wind Tunnel Test Configurations and Available Data Campaigns. Technical report, National Renewable Energy Laboratory, Golden, Colorado, USA, 2001. NREL/TP-500-29955.

[100] C. Lindenburg. Investigation into Rotor Blade Aerodynamics. Technical report, ECN, Petten, Netherlands, 2003. ECN-C–03-025.

[101] C. Hansen. AirfoilPrep: An Excel workbook for generating airfoil tables for Aerodyn and WT_Perf. See also URL https://nwtc.nrel.gov/AirFoilPrep.

[102] L. Fingersh, M. Hand, and A. Laxson. Wind Turbine Design Cost and Scaling Model. Technical report, National Renewable Energy Laboratory, Golden, Colorado, USA, 2006. NREL/TP-500-40566.

[103] R. Smith. *Uncertainty Quantification: Theory, Implementation, and Applications*. Society for Industrial and Applied Mathematics, 2014.

[104] J. C. Helton and F. J. Davis. Latin Hypercube Sampling and the Propagation of Uncertainty in Analyses of Complex Systems. *Reliability Engineering and System Safety*, 81(1):23–69, 2003.

[105] J. M. Hammersley and D. C. Handscomb. *Monte Carlo Methods*. Chapman and Hall, New York, 1964.

[106] M. Tari and A. Dahmani. Refined Descriptive Sampling: A better Approach to Monte Carlo Simulation. *Simulation Modelling Practice and Theory*, 14(2):143–160, 2006.

[107] Lumina Blog. Latin Hypercube vs. Monte Carlo Sampling. See also URL http://blog.lumina.com/2014/latin-hypercube-vs-monte-carlo-sampling/.

[108] R. G. Ghanema and P. D. Spanos. *Stochastic Finite Elements: A Spectral Approach*. Dover, London, 1991.

[109] L. Mathelin, M. Y. Hussaini, and T. A. Zang. Stochastic Approaches to Uncertainty Quantification in CFD Simulations. *Numerical Algorithms*, 38(1–3), 2005.

[110] P.E. Gill, W. Murray, and M.H. Wright. *Practical Optimization*. Academic Press, 1981.

[111] Z. Ugray, L. Lasdon, J. Plummer, F. Glover, J. Kelly, and R. Martí. Scatter Search and Local NLP Solvers: A Multistart Framework for Global Optimization. *INFORMS Journal on Computing*, 19(3):328–340, 2007.

[112] D. E. Goldberg. *Genetic Algorithms in Search, Optimization & Machine Learning*. Addison-Wesley, 1989.

[113] C. Audet and J. E. Dennis. Analysis of Generalized Pattern Searches. *SIAM Journal on Optimization*, 13(3):889–903, 2003.

[114] Hugo. Gradient descent. See also URL http://www.onmyphd.com/?p=gradient.descent.

[115] Mathworks. MATLAB documentation. See also URL http://www.mathworks.co.uk/help/matlab/.

[116] A. R. Conn, N. I. M. Gould, and Ph. L. Toint. A Globally Convergent Augmented Lagrangian Algorithm for Optimization with General Constraints and Simple Bounds. *SIAM Journal on Numerical Analysis*, 28(2):545–572, 1991.

[117] K. Deb and S. Srivastava. A Genetic Algorithm Based Augmented Lagrangian Method for Accurate, Fast and Reliable Constrained Optimization. Technical report, Kanpur Genetic Algorithms Laborator, Kanpur, UP, India, 2011. KanGAL Report Number 2011012.

[118] T. G. Kolda, R. M. Lewis, and V. Torczon. A generating set direct search augmented lagrangian algorithm for optimization with a combination of general and linear constraints. Technical report, Sandia National Laboratories, Albuquerque, New Mexico, USA, 2006. SAND2006-5315.

[119] D. M. Somers. Design and Experimental Results for the S809 Airfoil. Technical report, National Renewable Energy Laboratory, Golden, Colorado, USA, 1997. NREL/SR-440-6918.

[120] M. Costa and E. Minisci. MOPED: a multi-objective parzen-based estimation of distribution algorithm. In *EMO 2003*, pages 282–294, Faro, Portugal, 2003. Springer.

[121] M. Vasile, E. Minisci, and M. Locatelli. An inflationary differential evolution algorithm for space trajectory optimization. *Evolutionary Computation, IEEE Transactions on*, 15(2):267–281, 2011.

[122] J.A. Lozano, P. Larranaga, I. Inza, and E. Bengoetxea. *Towards a New Evolutionary Computation: Advances on Estimation of Distribution Algorithms (Studies in Fuzziness and Soft Computing)*. Springer, February 2006.

[123] K. Fukunaga. *Introduction to statistical pattern recognition*. Academic Press, 1972.

[124] G. Avanzini, D. Biamonti, and E.A. Minisci. Minimum-fuel/minimum-time maneuvers of formation flying satellites. In *Adv. Astronaut. Sci.*, pages 2403–2422, 2003.

[125] K. Deb, A. Pratap, S. Agarwal, and T. Meyarivan. A Fast and Elitist Multiobjective Genetic Algorithm: NSGA-II. *Evolutionary Computation, IEEE Transactions on*, 6(2):182–197, 2002.

[126] D. Datta, K. Deb, C.M. Fonseca, F.G. Lobo, P.A. Condado, and J. Seixas. Multi-objective evolutionary algorithm for land-use management problem. *International Journal of Computational Intelligence Research*, 3(4):371–384, 2007.

[127] K. Deb. Scope of stationary multi-objective evolutionary optimization: A case study on a hydro-thermal power dispatch problem. *Journal of Global Optimization*, 41(4):479–515, 2008.

[128] R.H. Leary. Global optimization on funneling landscapes. *Journal of Global Optimization*, 18(4):367–383, 2000.

[129] N. Dodgson. Bezier curves. See also URL http://www.cl.cam.ac.uk/teaching/2000/AGraphHCI/SMEG/node3.html.

[130] MalinC. Bézier curves and continuity explained. See also URL http://scratch.mit.edu/projects/11824563/.

[131] J. F. Mandell, D. D. Samborsky, P. Agastra, A. T. Sears, and T. J. Wilson. Analysis of SNL/MSU/DOE Fatigue Database Trends for Wind Turbine Blade Materials. Technical report, Sandia National Laboratories, Albuquerque, New Mexico, USA, 2010. SAND2010-7052.

[132] National Renewable Energy Laboratory. Classes of wind power density at 10 m and 50 m. See also URL http://rredc.nrel.gov/wind/pubs/atlas/tables/1-1T.html.

[133] C. Zang, M.I. Friswell, and J.E. Mottershead. A review of robust optimal design and its application in dynamics. *Computers and Structures*, 83:315–326, 2005.

[134] I. Das and J.E. Dennis. A closer look at drawbacks of minimizing weighted sums of objectives for pareto set generation in multicriteria optimization problems. *Structural Optimization*, 14(1):63–69, 1997.

[135] A. Haahr, Z. Chen, and M. Rajagopal. A wind turbine rotor blade with a cone angle and a method of manufacturing a wind turbine rotor blade with a cone angle. See also URL http://www.google.com/patents/WO2013091635A1?cl=en.

[136] J. Jonkman. FAST: An aeroelastic computer-aided engineering (CAE) tool for horizontal axis wind turbines. See also URL https://nwtc.nrel.gov/FAST.

[137] G. Leloudas, W. J. Zhu, J. N. Sørensen, W. Z. Shen, and S. Hjort. Prediction and Reduction of Noise from a 2.3 MW Wind Turbine. *Journal of Physics: Conference Series*, 75(1):1–9, 2007.